

AD_____

Award Number: W81XWH-09-1-0420

TITLE: High Resolution PET Imaging Probe for the Detection, Molecular Characterization, and Treatment Monitoring of Prostate cancer

PRINCIPAL INVESTIGATOR: Stan Majewski, Ph.D.

CONTRACTING ORGANIZATION: West Virginia Research Corporation
Morgantown, WV 26505-2742

REPORT DATE: July 2011

TYPE OF REPORT: Annual

PREPARED FOR: U.S. Army Medical Research and Materiel Command
Fort Detrick, Maryland 21702-5012

DISTRIBUTION STATEMENT: Approved for Public Release;
Distribution Unlimited

The views, opinions and/or findings contained in this report are those of the author(s) and should not be construed as an official Department of the Army position, policy or decision unless so designated by other documentation.

REPORT DOCUMENTATION PAGE				Form Approved OMB No. 0704-0188	
Public reporting burden for this collection of information is estimated to average 1 hour per response, including the time for reviewing instructions, searching existing data sources, gathering and maintaining the data needed, and completing and reviewing this collection of information. Send comments regarding this burden estimate or any other aspect of this collection of information, including suggestions for reducing this burden to Department of Defense, Washington Headquarters Services, Directorate for Information Operations and Reports (0704-0188), 1215 Jefferson Davis Highway, Suite 1204, Arlington, VA 22202-4302. Respondents should be aware that notwithstanding any other provision of law, no person shall be subject to any penalty for failing to comply with a collection of information if it does not display a currently valid OMB control number. PLEASE DO NOT RETURN YOUR FORM TO THE ABOVE ADDRESS.					
1. REPORT DATE July 2011		2. REPORT TYPE Annual		3. DATES COVERED 1 July 2010 – 30 June 2011	
4. TITLE AND SUBTITLE High Resolution PET Imaging Probe for the Detection, Molecular Characterization, and Treatment Monitoring of Prostate cancer				5a. CONTRACT NUMBER	
				5b. GRANT NUMBER W81XWH-09-1-0420	
				5c. PROGRAM ELEMENT NUMBER	
6. AUTHOR(S) Stan Majewski, Ph.D. Neal H. Clinthorne, M.S. E-Mail: smajewski@hsc.wvu.edu				5d. PROJECT NUMBER	
				5e. TASK NUMBER	
				5f. WORK UNIT NUMBER	
7. PERFORMING ORGANIZATION NAME(S) AND ADDRESS(ES) West Virginia Research Corporation Morgantown, WV 26505-2742				8. PERFORMING ORGANIZATION REPORT NUMBER	
9. SPONSORING / MONITORING AGENCY NAME(S) AND ADDRESS(ES) U.S. Army Medical Research and Materiel Command Fort Detrick, Maryland 21702-5012				10. SPONSOR/MONITOR'S ACRONYM(S)	
				11. SPONSOR/MONITOR'S REPORT NUMBER(S)	
12. DISTRIBUTION / AVAILABILITY STATEMENT Approved for Public Release; Distribution Unlimited					
13. SUPPLEMENTARY NOTES					
14. ABSTRACT The goal of this work is to improve methods of molecular imaging for diagnosis as well as treatment planning and monitoring in prostate cancer. This investigation hypothesizes that a dedicated endorectal probe for positron emission tomography (PET) will provide significant improvements in image quality over conventional, external-ring PET scanners used alone. The project is developing prototype high resolution PET detectors that have the possibility of endorectal use and is evaluating potential advantages using phantom studies prior to use in human subjects. Progress to date has been significant with the development of several prototype detectors that achieve desired resolution performance and that will be interfaced to a partial-ring PET system for testing in the upcoming year. Particularly exciting from the viewpoint of developing devices that can be tested clinically was interest in the technology by a major manufacturer of conventional PET instruments.					
15. SUBJECT TERMS Molecular Imaging, Positron Emission Tomography (PET), Prostate Cancer					
16. SECURITY CLASSIFICATION OF:			17. LIMITATION OF ABSTRACT UU	18. NUMBER OF PAGES 57	19a. NAME OF RESPONSIBLE PERSON USAMRMC
a. REPORT U	b. ABSTRACT U	c. THIS PAGE U			19b. TELEPHONE NUMBER (include area code)

Table of Contents

Report Update October 2011	4
Introduction.....	4
Body.....	4
Agreed Upon Statement of Work	4
Overview.....	6
Summary of progress in Year 1	6
Summary of progress in Year 2	6
Plans for Year 3	6
Aim 1: Probe requirements, modeling, etc.	6
Refine requirements	6
Develop Monte Carlo simulations	6
Incorporate device measurements from prototypes	6
Develop image reconstruction	6
Predict probe performance, refine models and reconstructions, etc.	7
Aim 2: Probe component selection and prototype construction	12
Report 1: Dedicated High Resolution Prostate PET Imager.....	12
Report 2: Achieving Sub-mm PET Resolution Using DOI Modules Based on Double-Sided SiPM Readout	15
Report 3: Development of a “Resistive” Readout for SiPM Arrays.....	18
Report 4: Development of a Mini Gamma Camera for Prostate Imaging	20
Aim 3: Probe demonstrator construction	23
Probe interfacing to PET ring at Michigan	23
Probe adaptation for human use.....	24
Aim 4: Phantom studies and performance evaluation	24
Key Research Accomplishments	25
Reportable Outcomes	25
Publications, abstracts, and presentations	25
Other reportable outcomes	26
Conclusions.....	26
Appendices.....	26

Addendum to the WVU report

INTRODUCTION (WVU REPORT VERSION)

We are including here in its entirety the summary report prepared by both partners and submitted from our collaboration by the leading PI, Dr Neal Clinthorne. In addition, we are commenting on the synergy of the project from the WVU perspective.

THE PROJECT'S SYNERGY (WVU REPORT VERSION)

The synergy of the project, especially in its initial phase, is in the complementary roles and strengths of the two partners. (The WVU group is the minority partner in this project with most of the resources for the effort going to UM.) The UM group had the initial idea of a dedicated prostate PET with a probe. UM also did the simulations of the system. The WVU group, benefiting from their unique technical skills, built the very high performance (sub-mm 3D resolution) PET probes (with DOD funds but also with other matching funds). The UM built the PET scanner to operate with the WVU prototype probe(s), and perfected the simulations and reconstruction algorithms. The WVU developed additional probes as alternatives to the first probes. These complementary key efforts were done in parallel at UM and WVU until the last phase when the assembly and operation of the whole system takes place at UM.

Due to the outstanding progress in the PET probe instrumentation development achieved at WVU, the side spin-off efforts were initiated early in the process, with new partners interested to be involved in the prostate PET instrumentation. As an expression of the successful partnership, WVU and UM decided to initiate together other projects. Some of the additional interested partners are Siemens and JHU.

In addition, sparked by the initial development, the WVU group developed other options for the prostate PET imaging, beyond the initial scope of the common project. Several stand-alone PET systems were constructed utilizing the PET probes. The plans are underway to combine the PET modality with ultrasound to improve prostate biopsy guidance. Industrial partners were also identified and there are plans for common efforts to develop marketable mobile high performance dedicated prostate PET imagers. One of the concepts for the dedicated prostate PET was awarded with a US patent.

REPORT UPDATE OCTOBER 2011

This report was delayed due to illness of one of the Principal Investigators. In the intervening time, significant additional progress has occurred, which will be described in detail in the report for the 2012 and briefly noted here. Significantly, two prostate probe prototypes have been provided to the PI's lab at the University of Michigan for testing with the PET ring emulator. One probe is a single-sided readout detector that does not have 3D position resolution and consists of a 24 x 24 array of 1mm x 1mm x 10mm LYSO scintillation crystals read out by a 5 x 5 array of Hamamatsu silicon photomultipliers. The other is a probe having double-sided readout that provides ~1mm FWHM depth-of-interaction (DOI) resolution. A recent analysis shows that while DOI resolution may not be necessary in all cases, it is nevertheless a highly desirable feature.

At Michigan, initial stages of interfacing have been completed. Coincidence images have been obtained from the probe having double-sided readout, and remaining interfacing to the ring system will occur in the next two weeks. Initial versions of the data acquisition and 3D image reconstruction software have been completed and—for the most part—tested. The mechanical setup necessary to handle larger phantoms is straightforward but remains to be constructed. Initial testing can occur with the existing small field-of-view configuration. Overall, as noted in the following report, our schedule slipped a bit as far as detector delivery to Michigan and interfacing; however, we made significant progress in August through October and are now close to the original timeline.

INTRODUCTION

The scope of the research is the investigation of the concept of the dedicated prostate PET imager composed of an endorectal PET probe and a partial PET imager ring, operating in a coincidence. The probe placed close to the prostate is a high resolution element of this system, utilizing the magnification PET imaging concept. The University of Michigan team's responsibility is the design and simulation of the concept, construction of the external partial PET ring, and image reconstruction of the resultant laboratory prototype(s) assembled at the University of Michigan. The WVU partner's primary responsibility is in comparative design, construction and validation of the prostate probe based on Silicon Photomultiplier technology. Progress for Year 2 of this project is outlined below.

There are no anticipated changes to the Statement of Work for the upcoming year. Probes developed at WVU will be interfaced to the partial PET ring at Michigan and evaluated.

BODY

Agreed Upon Statement of Work

The Statement of Work agreed upon among the participating parties and the granting agency is shown below. Tasks required for this year that are on schedule or essentially complete are shaded in green while those behind schedule are shaded red..

<i>Aim / Task</i>	<i>Month (from the start)</i>	<i>Contributing/ <u>Responsible Party</u></i>
Aim 1: Probe requirements and modeling (Michigan)		
Refine probe requirements	1-3	MP/ <u>NC</u>
Develop Monte Carlo simulations	1-6	SH/ <u>NC</u>
Incorporate device measurements from prototypes in Aim 2	6-12	SH/SM/ <u>NC</u>
Develop image reconstruction	1-12	SH/ <u>NC</u>

Predict probe performance & evaluate	3-12	SH/MP/SM/ <u>NC</u>
Refinements of models, image reconstruction, and performance evaluation methods	12-36	SH/MP/SM/ <u>NC</u>
Aim 2: PET probe component selection/validation and prototyping (WVU)		
Technical design selection (options)	2-4	JP/NC/ <u>SM</u>
Selection of SiPM modules	3-4	JP/ <u>SM</u>
Designing and building prototypes	5-8	AS/BK/ <u>SM</u>
Prototype testing	6-9	AS/JP/ <u>SM</u>
Technical design selection (final)	9	JP/NC/ <u>SM</u>
Aim 3: Probe demonstrator construction/Interface to PET (WVU / Michigan)		
Produce electronics boards	10-11	JP/ <u>SM</u>
Assemble SiPMs with electronics	12	JP/ <u>SM</u>
Mechanical assembly with enclosure	10-11	<u>BK</u>
DAQ assembly/DAQ software	6-9	JM, <u>JP</u>
Laboratory performance tests / Intrinsic performance evaluation/Attestation	10-12	AS/JP/ <u>SM</u>
Interface with PET ring at Michigan	12-18	AS/SM/SH/ <u>NC</u>
Performance testing / characterization of probe/ring	18-24	AS/SM/SH/ <u>NC</u>
Aim 4: Phantom Imaging studies and performance evaluation (Michigan / WVU)		
Construct phantoms	12-24	SH/MP/SM/ <u>NC</u>
Conduct phantom imaging studies	18-30	SH/MP/SM/ <u>NC</u>
Compare with performance predictions from Aim 1	18-36	SH/ <u>NC</u>
Summarize Research Results (Michigan / WVU)		
Clinical applicability of prostate probe	30-36	MP/SM/ <u>NC</u>
Device designs for next stage	30-36	MP/NC/ <u>SM</u>
Determine next funding steps (if any)	36	<u>MP/SM/NC</u>

<i>Resource</i>	<i>Abbreviation</i>	<i>Role / Location</i>
Neal Clinthorne	NC	PI, Michigan
Morand Piert, MD	MP	Co-inv, Michigan
Sam Seoung Huh	SH	Graduate Student Research Assistant, Michigan
Stan Majewski	SM	PI, WVU
James Proffitt	JP	WVU
Alexander Stolin	AS	WVU
John McKisson	JM	JLab (subcontract)
Brian Kross	BK	JLab (subcontract)

In the next sections, results for each task in the above Statement of Work are summarized. To aid the flow of the presentation, a detailed technical report follows the description of work performed for each task.

Overview

Summary of progress in Year 1

In the first year of the project, the highest risk elements of the prostate probe were addressed including potential performance improvements over conventional PET and methods for constructing the high performance endorectal detectors necessary to implement in such an instrument. Investigations showed that significant performance improvements were feasible in terms of better spatial resolution for a given level of image noise, and a number of feasible endorectal detector designs based on LYSO arrays and high performance just available on the market silicon photomultipliers were developed and tested.

Summary of progress in Year 2

Year 2 progress has continued along the same categories as progress in Year 1. In particular, various image reconstruction methods were evaluated, requirements for allowable size were refined, the performance and applicability of silicon photomultiplier technologies from various vendors were evaluated, and technologies necessary to adapt the probe to human use were investigated. We did not make it as far as desired in integration of the probe detectors developed at WVU with the partial-ring PET system at Michigan primarily due to graduation of the Ph.D. student assigned to the project. Nevertheless, we have developed the integration plan and electronics for interfacing the two systems and now must execute the plan. This will be assisted by our former graduate student whom we intend to appoint as a short-term postdoctoral fellow while he searches for a more permanent position. However, we benefited from this extra time to develop still better probes plus we tested them in other relevant configurations using planar panel PET modules. The results of this extensive extra work are included below in reports. This work enabled us to have an early start on submitting new proposals to continue the work on implementation of our concept. We chose partners such as Washington University in St. Louis and Siemens PET group in Knoxville, TN to work with us on these new-generation projects.

Plans for Year 3

Other than pushing integration into Year 3, we anticipate no changes from the original Statement of Work for the upcoming year.

Progress for Year 2 is described in more detail below.

Aim 1: Probe requirements, modeling, etc.

Refine requirements

Based on ongoing detailed discussions with urologists, allowable external size of the probe was refined and at 32mm in the largest cross-section it will allow for more detector material than originally anticipated. This is important because a greater detector volume directly translates to improved probe performance.

Develop Monte Carlo simulations

Monte Carlo simulations were developed in Year 1 and continue to be used to simulate data collection from the probe. While they have assumed a less prominent role in the work of Year 2, they will again play an important part in matching predictions from theory and simulations with measured performance.

Incorporate device measurements from prototypes

Complete. Reported last year. These performance measurements continue to be used to guide reconstruction development as noted below.

Develop image reconstruction

Image reconstruction was a significant focus this year. While statistically motivated reconstruction for PET is a well established technology, reconstructions that combine datasets having differing measurement uncertainties or that combine limited-angle high-resolution data with that from a conventional PET ring

remain an open research topic. Last year, we reported on a sliding-window list-mode reconstruction that can be used to form images in real time. This may well be useful for probe positioning; however, it is highly desirable to use the measurements in a manner that extracts as much information as possible about

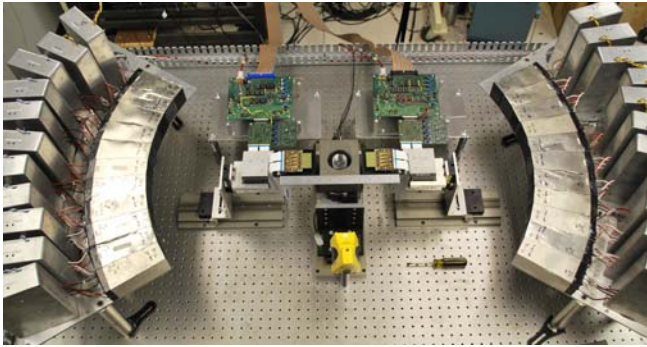


Figure 1. Partial ring PET system at Michigan showing 22 of 24 BGO detector blocks at 500mm radius.

the underlying radiotracer distribution in the prostate. Reconstruction results using measurements from the partial-ring PET system at Michigan as well as from Monte Carlo simulations are described in the next section.

Predict probe performance, refine models and reconstructions, etc.

We continue to refine reconstruction models and performance predictions. An important milestone this year was physical demonstration of the PET magnifier concept where a high resolution images in a small field-of-view are possible if a detector having high resolution (the probe) is located close to the field-of-view while lower resolution detectors (e.g., the conventional PET ring) are located further away. This is the basic principle leading to potential advantages of the endorectal prostate probe under development in this grant. Another milestone has been preliminary demonstration of performance enhancement possible by combining multi-resolution PET data in a single reconstruction. While much work remains, the basic concepts have been demonstrated and will be quickly applied to the prostate probe demonstrator that will be integrated in Year 3.

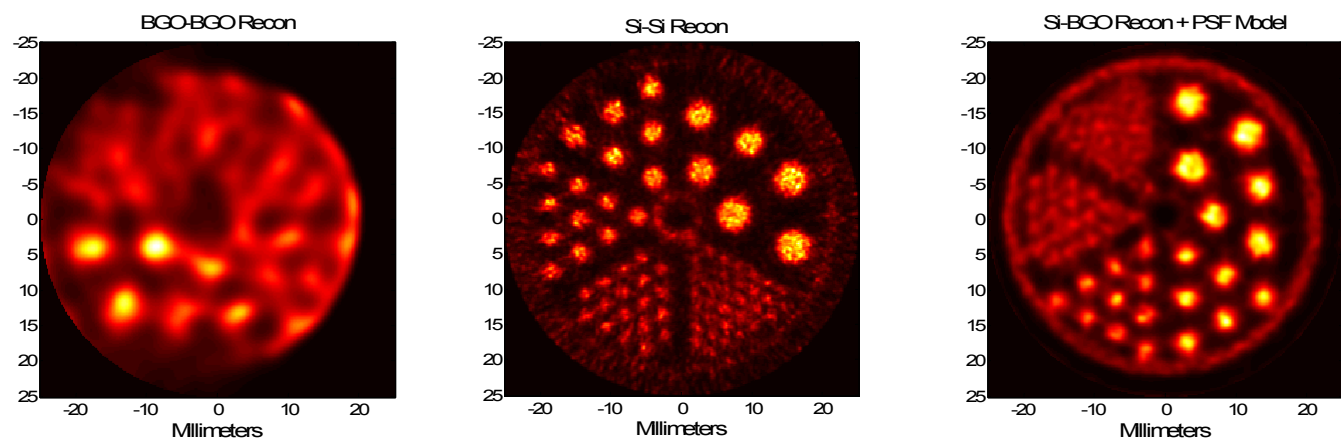


Figure 2: Resolution phantom images reconstructed from data acquired using the test system in Fig. 1. Left: Low resolution coincidence events only. Center: High resolution coincidence events only. Right: Reconstruction from mixed high and low resolution coincidence events. Note the improvement in resolution over the low resolution reconstruction demonstrating the “magnifying glass” concept used in the prostate probe. Rod diameters are 4.8 mm, 4.0mm, 3.2mm, 2.4mm, 1.6mm, and 1.2mm.

A key component of the work performed in Year 2 used the dual-ring PET demonstrator described last year and shown in Fig. 1. Briefly, the system comprises 24 BGO block detectors having 8 x 4 arrays of BGO crystals located at 500mm radius and two high resolution detector arrays (1.4mm x 1.4mm elements) located at 70mm radius around a small FOV. In the upcoming year, the small detectors and small FOV will be replaced with prostate probe prototypes from WVU as described under work in Aim 3 but this instrument has proven valuable for demonstrating the magnifier concept and for examining various reconstruction methods.

With this system, three types of events are possible: coincidences between the low resolution detectors in the outer ring, coincidences between the two high resolution detectors, and mixed coincidences where one annihilation photon interacts in the low and the other in the high resolution detector. The last, or mixed coincidence, forms the basis of the prostate probe (assuming that we cannot conveniently locate *two* high resolution detectors close to the prostate on either side). Figure 2 shows resolution phantom images reconstructed from F-18 PET data recorded using the device demonstrating the spatial resolution capabilities of each coincidence category. The leftmost image in Fig. 2 is the phantom reconstructed using only data from the low resolution outer PET ring. Because of the relatively poor performance of these detectors—as well as the common spatial undersampling associated with un-wobbled PET acquisition—reconstructed resolution is somewhat worse than 4mm FWHM. The center image in Fig. 2 is reconstructed using only coincidences from the high resolution detectors. In this case, reconstructed resolution is ~ 0.7 mm FWHM but as noted, this is not practical for prostate imaging. On the other hand, the rightmost image in Fig. 2 where reconstruction is from the mixed coincidence events shows much higher resolution than reconstructions from the external ring events alone demonstrating the magnifier concept. While this is closer to the arrangement that will ultimately be used in the prostate data acquisitions one must remember that the prostate probe will only acquire limited-angle data at high resolution. Effects of limited angle high-resolution acquisitions combined with full-ring lower resolution data are currently being studied and initial results are described later in this section.

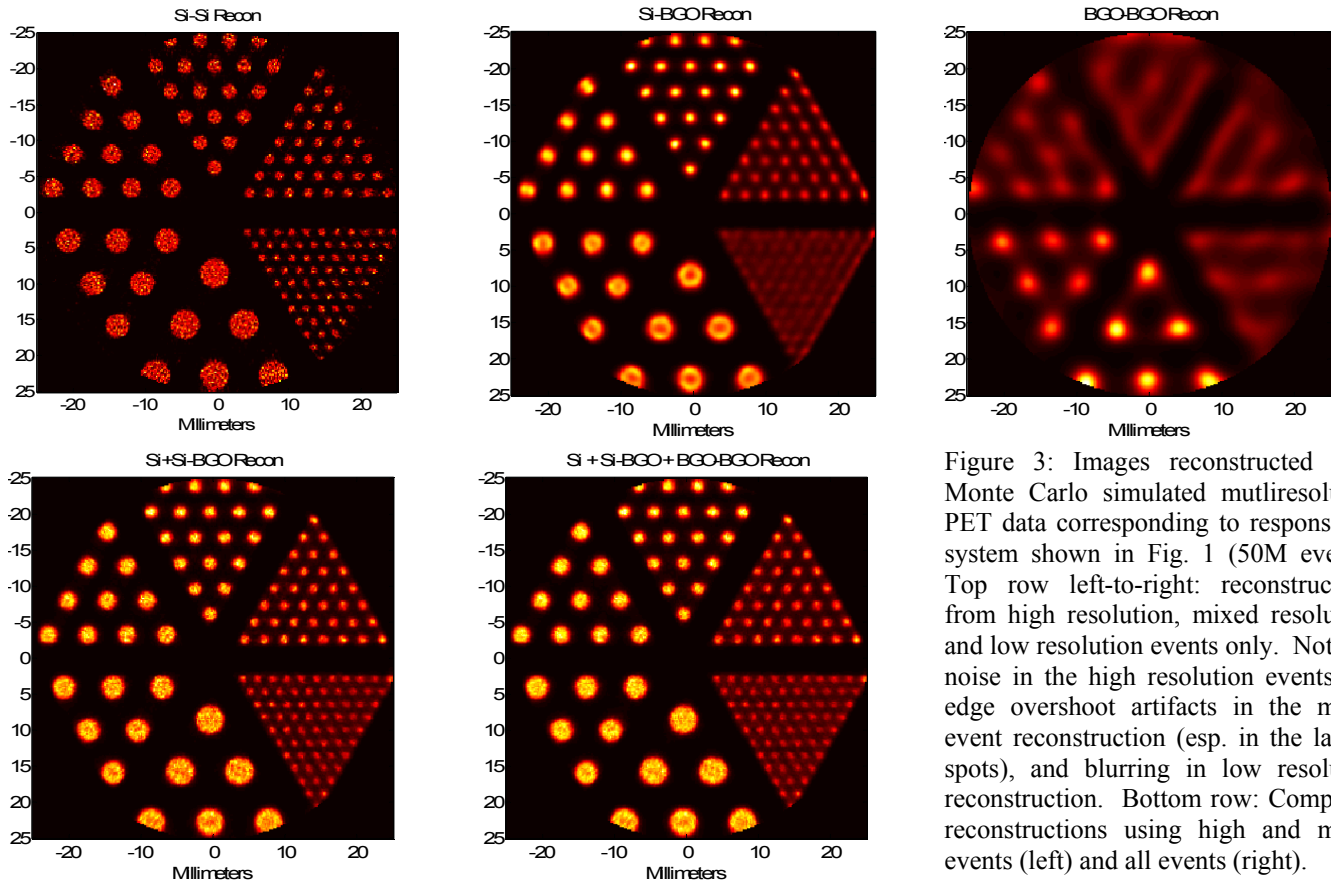


Figure 3: Images reconstructed from Monte Carlo simulated multiresolution PET data corresponding to response for system shown in Fig. 1 (50M events). Top row left-to-right: reconstructions from high resolution, mixed resolution, and low resolution events only. Note the noise in the high resolution events, the edge overshoot artifacts in the mixed event reconstruction (esp. in the largest spots), and blurring in low resolution reconstruction. Bottom row: Composite reconstructions using high and mixed events (left) and all events (right).

Taking full advantage of data acquired from the high resolution probe and low resolution external ring requires a reconstruction method that can optimally combine the measurements to reconstruct a single underlying image volume. If we take the meaning of “optimal” to be the lowest reconstructed variance (or image noise) at a desired reconstructed point spread function (PSF), then the best reconstruction method is a slightly penalized, post-smoothed maximum likelihood reconstruction. This technique requires having accurate models of the PET system response including the spatial resolution and sensitivity for each event

category. Demonstrating this with the system shown in Fig. 1 has proceeded in several steps (and work continues).

Shown in Fig. 3 are reconstructions from high count (50M events) simulated data generated using the system model for the partial-ring PET system. The highest resolution events (0.7mm FWHM) have the lowest abundance, the lowest (3mm FWHM) the highest abundance, and the mixed coincidences are between in both resolution (1.2mm FWHM) and abundance. The top row of Fig. 3 shows reconstructions from the individual event categories alone (same as in Fig. 2). Present in these images are common PET reconstruction artifacts. For example, the high resolution image shows significant image noise due to the relatively low sensitivity of the instrument for these highest resolution events. The largest spots in the center image (reconstructed from the mixed events) show typical edge overshoots resulting from attempting significant resolution recovery. The image reconstructed from the lowest resolution events alone demonstrates significant undersampling or aliasing artifacts. The bottom row of Fig. 3 shows results of combining the multiresolution data to form a single, best image. At bottom left is the image reconstructed from the high and mixed resolution events. Noise and overshoot artifacts are significantly reduced while spatial resolution is improved. The image at bottom right was reconstructed using all events. In this case, the lowest resolution data did not add significantly to performance but *did* require many additional iterations to attain a similar degree of convergence. This phenomenon is currently under investigation.

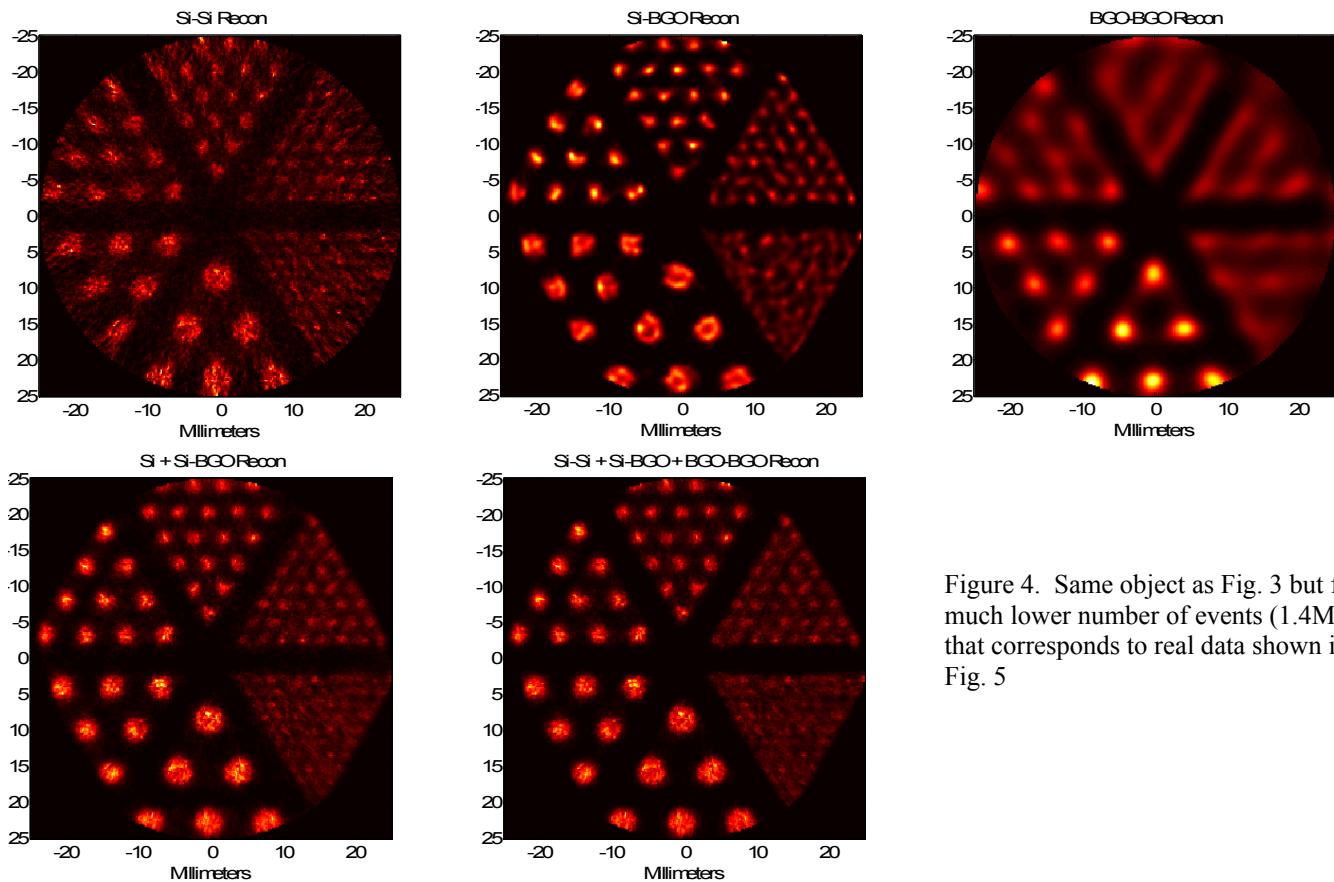


Figure 4. Same object as Fig. 3 but for a much lower number of events (1.4M) that corresponds to real data shown in Fig. 5

Because of sensitivity limitations of the configuration shown in Fig. 1, we also generated simulated data for the same object in Fig. 3 but with many fewer coincidence events (1.7M total) to correspond with actual measurements from the PET system. Conclusions are the same as for reconstructions from higher count data although images shown in Fig. 4 are noisier.

Finally, the measurements—also containing a total of 1.7M coincidence events—obtained using the system in Fig. 1 were reconstructed and are shown in Fig. 5. While the images are noisy, they demonstrate the

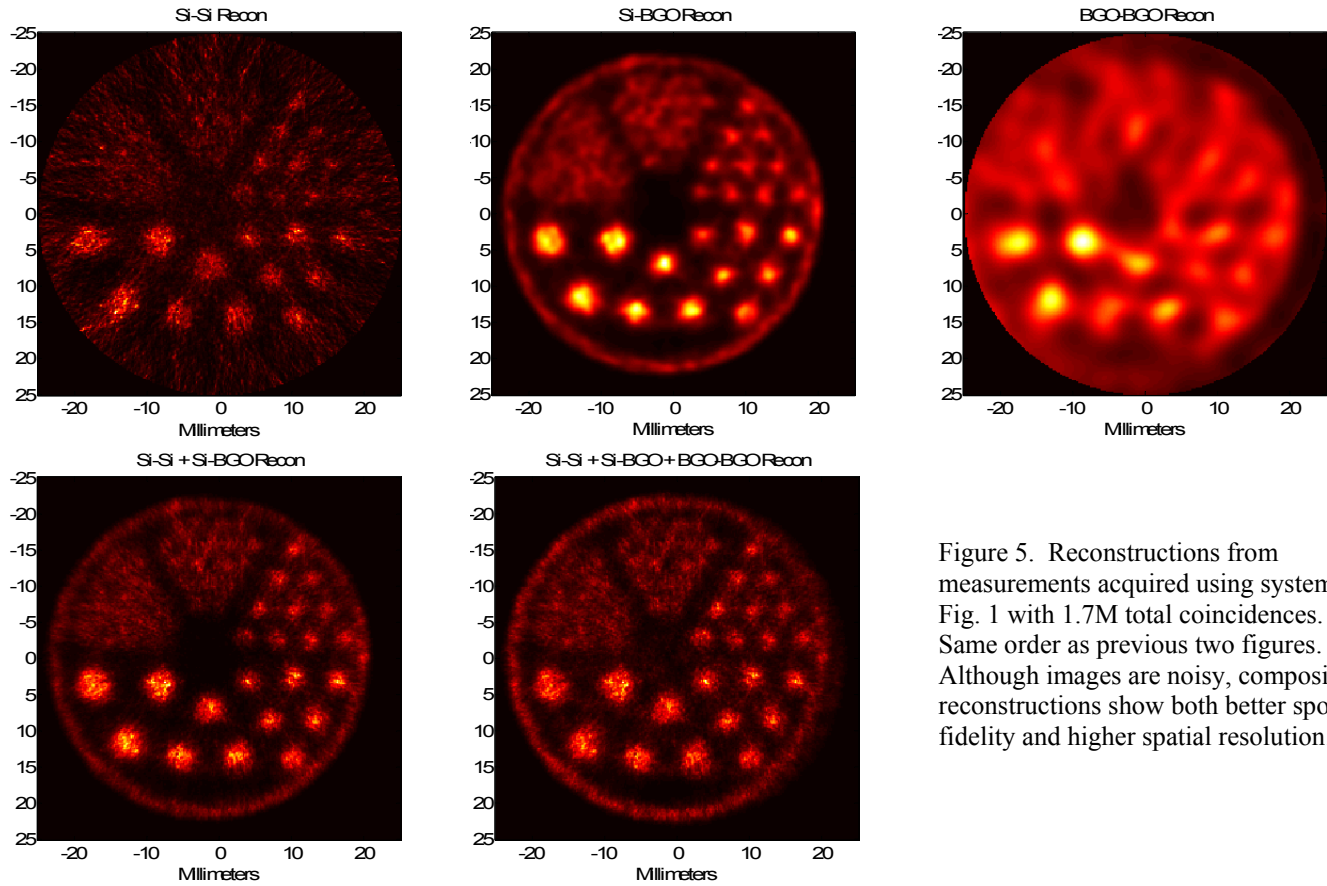


Figure 5. Reconstructions from measurements acquired using system in Fig. 1 with 1.7M total coincidences. Same order as previous two figures. Although images are noisy, composite reconstructions show both better spot fidelity and higher spatial resolution.

same effects shown in the reconstructions from simulated data. One reason that this study is important is that it shows that the system modeling used (which contained many approximations) in the reconstruction was good enough to see an effect. Over the next month, much higher count measurements will be used to refine reconstruction development and potential performance advantages.

While the above studies are important in that they demonstrate the PET magnifier concept and advantages of image reconstruction from multiresolution data, as noted the prostate probe will augment data from the conventional PET ring with limited-angle high resolution data. We have been studying this effect in various probe geometries and have developed Monte Carlo simulations and—recently—a 3D PET reconstruction algorithm. As yet, the work is preliminary requires additional studies but the 3D reconstruction is a necessary component of this project and is straightforward to adapt to the geometry that will be used for prostate probe measurements in the upcoming year.

Figure 6 shows the configuration of an external ring PET detector, external 10cm x 10cm x 1cm thick probe detector, and resolution phantom modeled using the GEANT 4 Monte Carlo code. Preliminary reconstructions obtained from simulated data and the 3D PET reconstruction are shown in Fig. 7.

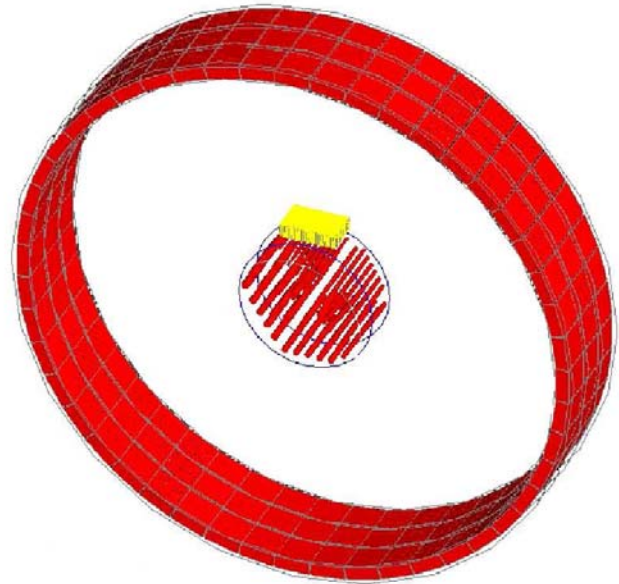


Figure 6. Diagram of setup used for Monte Carlo simulations of externally located 10cm x 10cm x 1cm probe within an 80cm diameter LSO-based PET ring. Probe is located adjacent to highest resolution segment of phantom.



Figure 7. Preliminary 3D PET reconstructions of phantom shown in Fig. 6. Left: ring-ring coincidences only. Center: probe-ring coincidences only. Right: composite reconstruction. Although the composite reconstruction in this case fails to show significant improvements, there are two significant issues. First, the resolution of the PET ring was nearly as high as could be supported by the pixel size in the reconstruction; and second, significantly more iterations are required for convergence in combined dataset.

The leftmost image is a slice of the phantom reconstructed from the external PET ring data alone (ring-ring coincidences). The center image is reconstructed from probe-ring coincidences. Note the reconstruction artifacts due to limited-angle measurement data. The composite reconstruction algorithm combined the two datasets to produce the image on the right in Fig. 7. Two things must be noted in this preliminary work. First, the spatial resolution of the external ring data was unrealistically good and near the limiting resolution that was supportable by the voxel size used in the reconstructions. Given this, we might not expect to see much of an effect of adding the high resolution probe data, which is indeed the case. Second, as noted above, composite reconstructions using all data appear to take significantly more computation to reach similar levels of convergence. Since the same number of iterations was used for each of the reconstructions in Fig. 7 (as well as Fig. 8), it is likely that the image reconstructed from the probe-ring and ring-ring coincidences is not close to convergence and many more iterations are necessary. These effects will be explored in more detail in the coming few months.

Figure 8 show images reconstructed from data simulated using a model more closely resembling the instrument shown in Fig. 1 having only one probe detector. Similar to the prostate probe there are ring-ring and ring-probe coincidences. In this case, higher resolution measurements are provided by the ring-probe coincidences and while the composite reconstruction shows some improvement in resolution, again, it likely requires many more iterations to attain an appropriate degree of convergence for the combined measurements.

While the preliminary studies described here provide significant information on issues involved with combining multiresolution data, the importance relative to the prostate probe work is that (1) from theory, the optimum reconstruction method has this basic structure, and (2) an implementation of the 3D PET reconstruction necessary for this project has been developed.

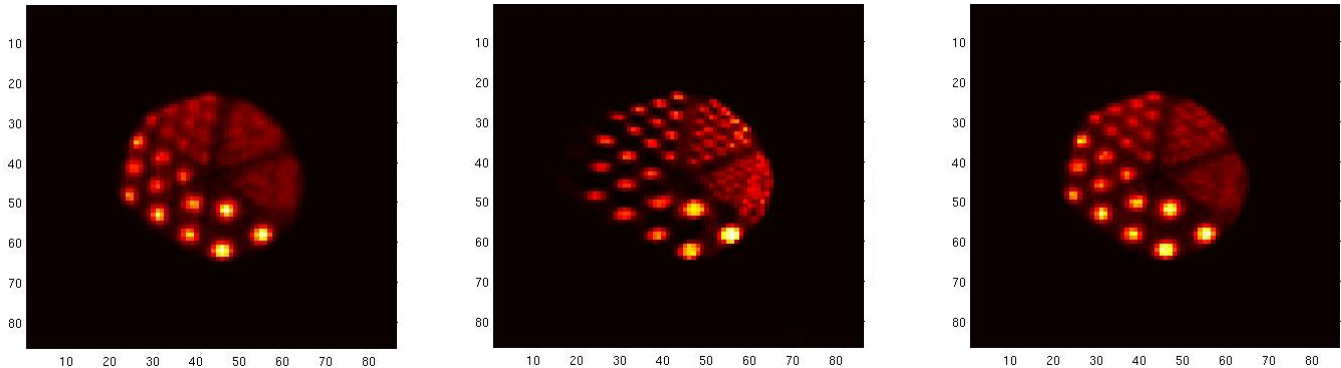


Figure 8. Simulated full-ring and limited-angle probe data for 45mm diameter phantom used in Figs 2–6. See text for details.

Aim 2: Probe component selection and prototype construction

Work conducted under this aim, as planned initially, was essentially completed in Year 1 and described in last year's progress report. However, we continued with this development due to the opportunity of having more SiPM prototypes and also using developed planar panel PET imagers paired with the probes to form prototype imagers, in addition to the UM system. We developed several more probe prototypes and readout options, as shown below. The short included reports were submitted to be presented as talks and posters at the 2011 IEEE Medical Imaging Conference planned in October 2011 in Valencia, Spain.

Report 1: Dedicated High Resolution Prostate PET Imager

Abstract. We are developing a dedicated high resolution ($\sim 1\text{mm}$) and high efficiency prostate PET imager that can operate with standard Transrectal Ultrasound probes and that can provide accurate localization of the tumor, especially when used with the new prostate cancer specific PET imaging agents. The PET system will have two major components: the sub-mm resolution endorectal PET probe and the dedicated PET scanner. The co-registered TRUS component will provide the usual structural 2D or 3D information, while the PET imager will provide the metabolic information related to the biological state of the prostate. We are reporting on preliminary data acquired with the prototype imager. The main highlight is achieving $\sim 1\text{mm}$ FWHM DOI resolution with the PET probe using new monolithic MPPC arrays from Hamamatsu.

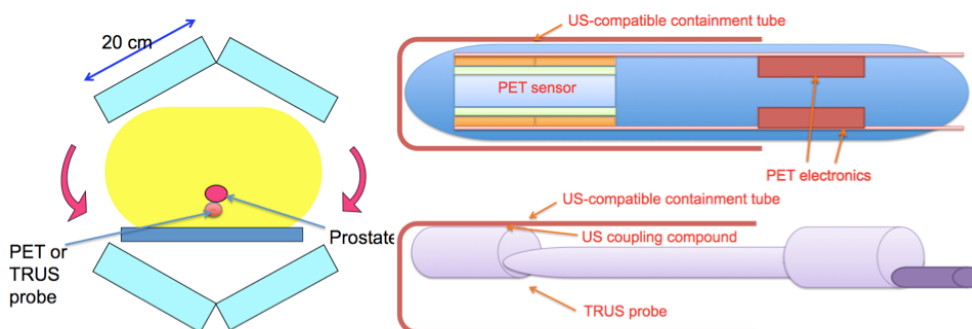


Figure 1. Left: Schematic of the high resolution ($\sim 1\text{mm}$) PET imager composed of four planar modules, 216 mm x 162 mm each in size, mounted on a rotating gantry, and a prostate PET probe providing local sub-mm spatial resolution. The PET probe can be inserted interchangeably with the Transrectal Ultrasound (TRUS) probe by putting them inside a containment

tube (made out of ultrasound-compatible material) that is immobilized and mounted to the patient table during the scans. This approach minimizes the relative movement of the prostate during and between the scans. In addition, both probes (and the PET scanner modules) are equipped with position sensors. This arrangement assures high accuracy in maintaining the same position of the prostate during scans, and the control of the absolute and relative positions of all components of the entire imaging system, therefore substantially easing the task of co-registration of the PET and TRUS images. For TRUS to operate with high efficiency, an ultrasound coupling compound will be used during TRUS scans, and the TRUS probe will be placed in contact with the containment tube.

The sub-mm resolution prostate PET probe

Our new prototype of the PET probe is based on the latest variant of SiPMs manufactured by Hamamatsu. The Multi-Pixel Photon Counter (MPPC) S10943-3344MF-050 monolithic array measures about ½" by ½" and consists of an array of 4 x 4 (16) ~3mm x 3mm mm active imaging elements (pads).

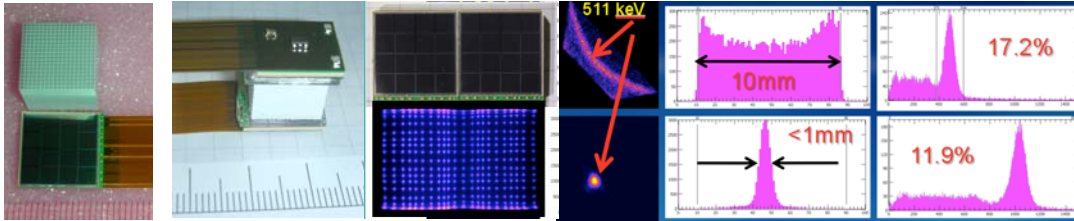


Figure 2. Left: 0.7mm step x 10mm thick 18x18 pixel LYSO DOI array from Proteus with double sided output and S10943-3344MF-050 MPPC array from Hamamatsu. The LYSO array was optimized for the DOI operation. Two butted

arrangements of four (2 x 2) such arrays will be used in the proposed PET probe. Third from left: Test of the side-to-side butting. Raw image at left bottom shows only a small response perturbation in the junction region. Energy dropped by 15% and energy resolution changed from 11.8% to 12.1% @511 keV. The 2D plots at left display the signal relationship between top and bottom MPPC array outputs for the broad beam (top) and narrow collimated beam (produced with electronic collimation of a 1mm Na22 seed source) (bottom). These pilot (02/13/2011) DOI results show < 1mm FWHM DOI resolution for one of the 0.7mm pixels close to the edge of the LYSO array. The central histograms show the ratio of the sum signal from the top MPPC module by the sum of the signals from both modules, for a broad 511 KeV gamma beam (top), and the narrow beam (bottom), respectively. At right the energy spectra for the same selected LYSO pixel and the narrow beam case are shown, for the top array (17.2% FWHM @511 keV, top spectrum) and for the sum (11.9% FWHM @511 keV, bottom spectrum).

We have tested temperature response of the whole detector module (array plus one MPPC array). We have shown that we can operate from room temperature to over 110°F with no visible impact on performance, except the requirement to correct (increase) bias voltage at higher temperatures.

The 1.0-1.5mm resolution dedicated prostate PET imager

The current plan is to build each panel module of the PET scanner with twelve Hamamatsu H8500 PMTs arranged in a 4 by 3 matrix. Each PMT will be coupled to a 36 by 36 array of 1.5 x 1.5 x 15 mm LYSO scintillator pixels from Proteus, covering a 54 mm x 54 mm area. The key novel element (available only starting February, 2011) is the compact, 5.3 mm thick, tapered light guide that couples these oversized arrays to the PMTs, with excellent results, as shown below.

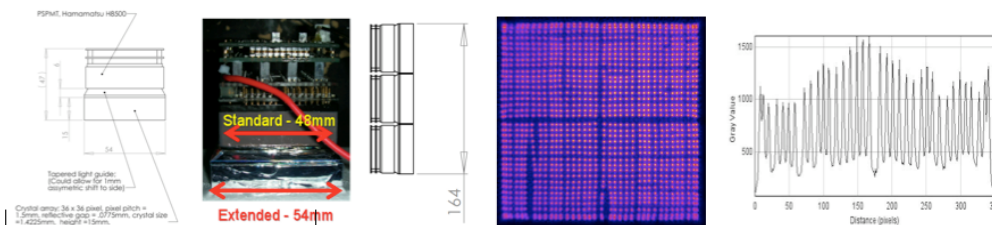


Figure 3. The novel (Feb, 2011) high resolution PET module based on a H8500 PMT, and a tapered custom-made compact (5.3 mm thick) light guide that connects the 54 mm square Proteus/Agile LYSO array of 1.51 mm x 1.51 mm x 15 mm pixels to a 48 mm x 48 mm

active surface of the PMT. This excellent result permits tight assembly of 12 such modules to form extended and uniform high resolution detector surface without dead regions.

Each PSPMT will be equipped with a gain-equalization resistor matrix and a read-out board that houses preamplifiers and 4-channel multiplexed analog signals (a,b,c). These boards correct for gain variation across the faces of PSPMTs as well as reduce the number of required read-out channels. Three modules from each column will be combined to form one channel in the coincidence matrix, with four output position channels per column. A total of 4 x 4=16 ADC channels will be required per each panel imager, and a total of 64 channels for all four panel modules. The same software package that reads out the SiPM probe will be used to acquire data from the panel detectors. The panels will be mounted on an already available rotating gantry. A mobile cabinet will house all the necessary electronic components, such as PCs, power supplies etc.

A very important part of our dedicated PET system is a motion-tracking apparatus. We plan on utilizing a MicroBird EM tracking system, from Ascension Technology Corp. Six such sensors will be used for independent spatial localization of the two probes (PET and TRUS) and each panel imager. Transmitters (two) will be attached to the dedicated non-metallic patient bed produced by Agile specifically for our imaging system and will remain stationary for the entire imaging session. We have measured the spatial accuracy of MicroBird sensors to be installed on the PET and TRUS probes, within a volume of 2" x 2" x 2" (sufficient for prostate imaging and obtained accuracy (measured as deviation from the linear relationship between the real position and the measured position) in the 0.36 - 0.45 mm FWHM range. For larger movement volume involved with the PET panels, an accuracy of over 1.2 mm FWHM was defined from these tests. Both values are adequate for their corresponding detector modules. Positioning information will be time-stamped with a computer clock and supplied to the reconstruction module of the software. Prior-developed PET reconstruction methodology (d,e) will be upgraded to include motion tracking. The reconstruction module will combine annihilation gamma interaction information with the tracking system data to obtain a set of lines-of-response.

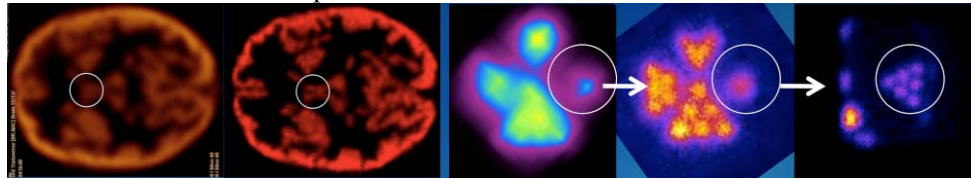
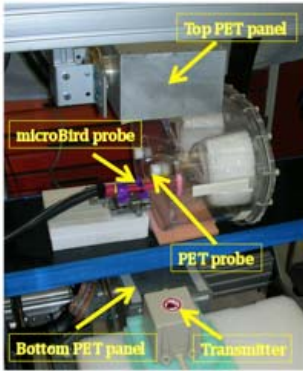


Figure 4. Left: The prototype of high resolution PET imager composed of two 20 x 15 cm panel modules based on 2 x 2 x 15 mm LYSO arrays coupled to 4 x 3 arrays of H8500 PMTs, and mounted on a computer-controlled rotating gantry. The coverage (width) of these modules (20 cm) was designed for the breast imager (f), and is insufficient to accommodate the width of a prostate patient (g). The PET probe is shown with the attached position sensor, both inserted in the phantom during position calibration studies. To demonstrate the spatial resolution capability of this prototype PET

scanner, a brain phantom was used filled with a ~60 Ci of ^{18}F -solution. Left image shows central ~5mm slice image obtained in a 10 minutes scan using Philips GEMINI TOF PET. Right image is the equivalent scan performed using dedicated PET imaging system. No absorption corrections were applied. The dedicated PET imager shows much more detail for example in the circled area. Right three images: spatial resolution step-wise improvement in imaging the high resolution Derenzo-type phantom by imaging it first with the Biograph 16 PET/CT scanner, the dedicated PET scanner, and finally with the PET probe in coincidence with the top planar module of the dedicated PET scanner. (The phantom has four groups of cylindrical holes: 2.5mm hole/5mm step, 2mm hole/4mm step, 1.5mm hole/3mm step, and 1mm hole/2mm step). The details of the 1mm hole group, not separated in the first two PET images (~8mm, and 2.5 mm spatial resolutions, respectively), are well separated in the detail image with the PET probe, as shown at right (1.1 mm spatial resolution), due to the 0.7mm intrinsic spatial resolution of this non-DOI probe. Holes from all four groups are not separated in the standard PET image.

- a. V. Popov, S. Majewski, B. L. Welch, "A Novel Readout Concept for Multianode Photomultiplier Tubes with Pad Matrix Anode Layout", Nuclear Instruments and Methods in Physics Research A 567 (2006) 319–322).
- b. V. Popov, "Matrix output device readout system", US Patent 6,747,263, 2004.
- c. R.R. Raylman, S. Majewski, B. Kross, V. Popov, J. Proffitt, M.F. Smith, A.G. Weisenberger, R. Wojcik, "Development of a Dedicated Positron Emission Tomography System for the Detection and Biopsy of Breast Cancer", Nuclear Instruments and Methods in Physics Research, A569 (2006), 291-295.
- d. M. F. Smith, S. Majewski, A. G. Weisenberger, D. A. Kieper, R. R. Raylman, and T. G. Turkington, "Analysis of factors affecting positron emission mammography (PEM) image formation", IEEE Trans. Nucl. Sci., vol. 50, pp. 53-59, 2003.
- e. M. F. Smith and R. R. Raylman, "PEM-PET image reconstruction in a clinically-relevant time frame", IEEE 2006 Nuclear Science Symposium Conference Record, pp. 1792-1796.
- f. Raymond Raylman, Jame Abraham, Hannah Hazard, Cortney Coren, Shannon Filburn, Judith Schreiman, Stan Majewski, Gary Marano, "Initial Clinical Test of a Breast-PET Scanner", accepted for publication in Journal of Medical Imaging and Radiation Oncology, 2011.
- g. Turkington T.G.; Hawk, T.C.; Coleman, R.E.; Smith, M.F.; Majewski, S.; Kross, B.J.; Wojcik, R.; Weisenberger, A.G.; DeGrado, "PET prostate imaging with small planar detectors", Nuclear Science Symposium Conference Record, 2004 IEEE Volume 5, Issue , 16-22 Oct. 2004 Page(s): 2806 – 2809.

Report 2: Achieving Sub-mm PET Resolution Using DOI Modules Based on Double-Sided SiPM Readout Introduction

Recent advancements in semiconductor light sensors technology enable design and construction of small-size radiation detectors without sacrificing detection efficiency and resolution. Such detectors allow for the novel applications of nuclear medicine techniques that were not possible due to bulky size of photomultiplier tubes. For example, in small PET imaging probes can be inserted inside patients and operate in conjunction with either commercial scanners or custom-built large area gamma detectors. Close proximity of a small detector to a source of radiation allows not only decreasing the amount of injected radioactivity, but will also deliver superior spatial resolution. But close placement of the detector inevitably leads to large number of gamma rays incident on the detector at highly oblique angles causing well-known parallax error. This necessitates a detector that is able to measure position in 3 dimensions, detector capable of depth-of-interaction (DOI) assessment.

Setup and Experiments

Our latest experimental apparatus consisted of a 18x18 LYSO scintillation array of 0.7mm x 0.7mm x 10mm pixels (Proteus Inc, Chagrin Falls, OH) with 50 micron Lumirror septa. Side surfaces of each crystal in the assembly underwent special roughing treatment in order to increase light absorption for optimized DOI-measurement. Crystal array was optically coupled (Visilox V-788 coupling compound) to two low profile (<2mm thick) 4x4 element SiPMs with 3x3mm pixels (S10943-3344MF-050 MPPC array from Hamamatsu, Hamamatsu City, Japan). 2mm-thick glass light spreader windows was placed between both SiPM/scintillator interfaces. Short flexible printed circuit cables were used to interface the PET module to custom 16 channel pre-amplifier boards (from Adaptive I/O Technologies, Blaksburg, VA,). Major components are displayed in Fig.1.

In addition to the Hamamatsu monolithic S10943-3344MF-050 SiPM arrays and the Proteus DOI-optimized LYSO scintillation array, our experimental apparatus consisted of two amplifier boards, two interface modules, and a 64ch DAQ box. Thirty-two output analog signals (16 per SiPM array) were digitized in a FPGA-based USB2 system, which has a modular extensible architecture with up to 64 channels of simultaneous sampling ADCs per unit, and a sustained trigger rate of over 150kHz for all channels. Read-out software was implemented using Java with a user interface based on Kmax scientific software package (Sparrow Corp., Port Orange, FL)

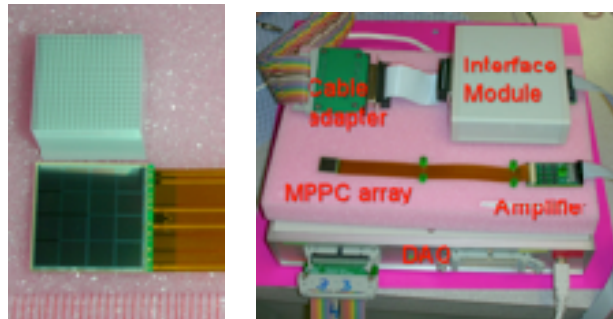


Fig. 1. Photograph of SiPM array and LYSO scintillation matrix are shown on the left. Right photo exhibits labeled components of experimental setup.

Selected results shown here were obtained with broad and with electronically collimated 511 keV annihilation photon beams from $\sim 10\mu\text{Ci}$ ^{22}Na sources. Electronically collimated annihilation photon beams were achieved by using a second detector with a 1cm-diameter Hamamatsu R1635 PMT optically coupled to a 1cm^3 LYSO scintillator, and operating in coincidence with the DOI module. Detector assembly and experiment schematic are shown in Fig.2.

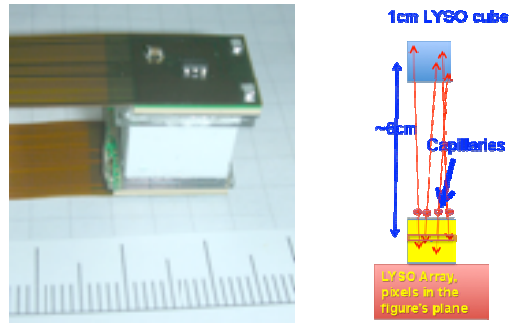


Fig. 2. Photo of assembled DOI-capable probe is shown on the left, schematic of ‘electronic collimation’ is displayed on the right.

Electronically collimated beam from a needle-tip source of ^{22}Na was placed near the side surface of the module with the needle holder attached to a translation stage. The source was scanned in 1 mm steps along the long dimension of the crystal array. 5 regions-of-interest (ROI) were chosen to include signal from the crystals located both at the center and at the edge of the array. Schematic of DOI-estimation measurement setup is in Fig.3.

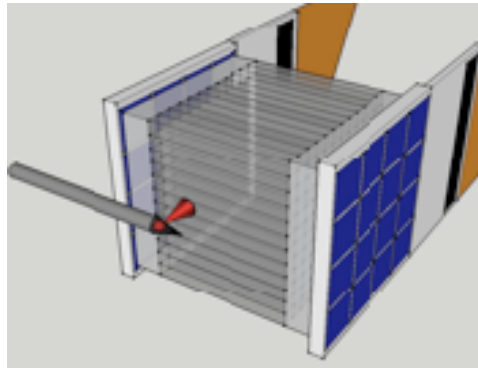


Fig. 3 Needle-tip source (< 0.5 mm) was placed ~ 1 mm away from the edge of the crystal array. The source was translated in 1 mm steps for a total of 9 linear positions.

Position information and energy signals from both SiPMs were recorded at each of 9 different linear positions. DOI position was estimated as

$$\text{DOI} = k \cdot E_1 / (E_1 + E_2) + b \quad (1)$$

where E_1 and E_2 are energies obtained from SiPM 1 and 2 respectively, k is a scaling factor obtained by a linear fit of measured DOI ratios to known linear positions and b is a linear offset, also known from the source positioning. Energy response of the detector was calculated as geometric mean of individual SiPM energies as to remove the dependence of light collection from the gamma interaction position.

Results

Image, obtained by flooding the detector with un-collimated beam with 511 keV gamma rays is shown in Fig.4. Separation of individual crystals is visibly demonstrated even at the edge of the detector surface. Also, Fig.4 exhibits image from the electronically collimated beam.

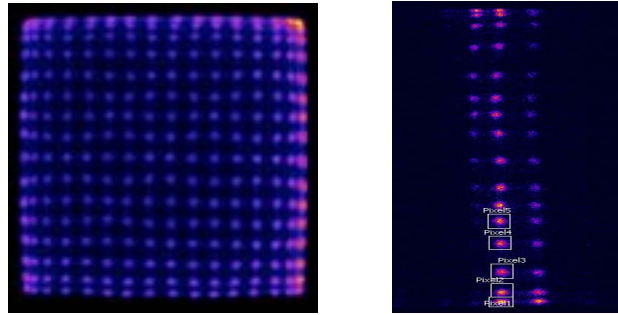


Fig. 4. Flood image is shown on the left and “pencil” beam image with ROIs is on the right.

Energy spectra for an individual pixel and overall detector are shown in Fig.5. Both collimated and broad beam illumination results are presented. Single-pixel energy resolution was measured to be 9.3 and 11% for single pixel narrow and broad beam respectively. Overall detector resolution obtained was 13 and 13.8 %. All the resolutions were measured at 511 keV.

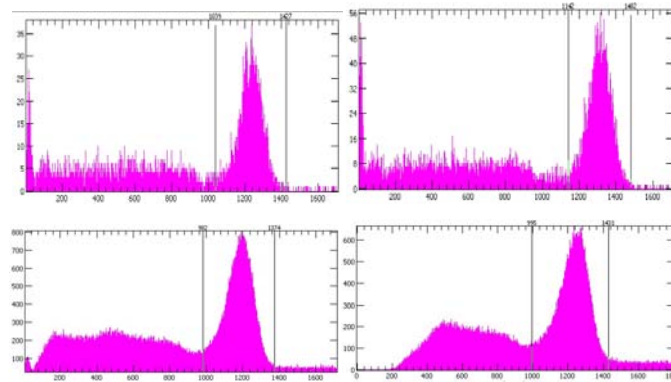


Fig. 5. Top row : energy spectra for narrow (left) and broad (right) illumination of a single LYSO crystal, chosen by placing ROI on the image. Bottom row: overall detector energy spectra under narrow (left) and broad (right) beam conditions.

Fig.6 and Table 1 summarize DOI resolution measurement results. Fig.6 shows linear fits to DOI-encoding ratio of energies obtained at different linear positions of needle-tip source. Fit parameters were used in calculation of DOI position using equation (1). Table 1 displays results of DOI spatial resolution measurements

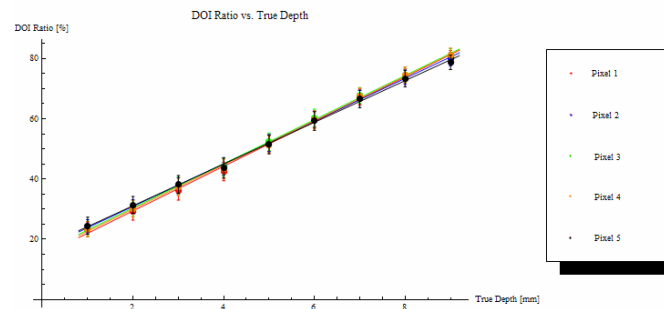


Fig.6. Linear fits to DOI-encoding ratios of energies vs source position.

Pixel	DOI resolution (mm)
1	0.71+/- 0.07
2	0.70+/- 0.07
3	0.73+/- 0.07
4	0.75+/- 0.08
5	0.83+/- 0.07
Overall	0.74+/- 0.12

Table1. DOI spatial resolution for 5 individual pixels and average over 5 selected pixels.

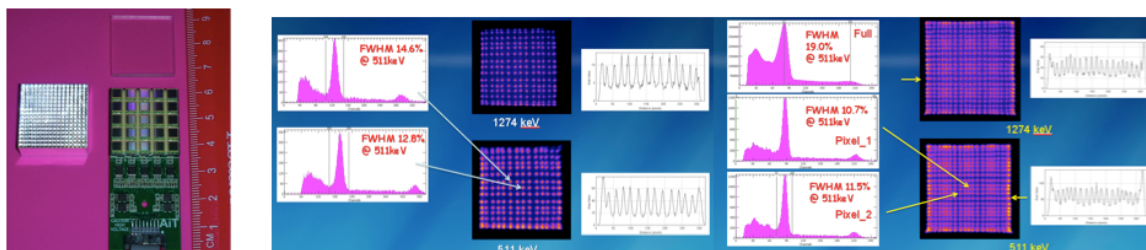
Discussion and Future Work

We have demonstrated that a compact PET module with dual-sided SiPM readout can achieve sub-mm spatial resolution in the plane perpendicular to the scintillation array and ≤ 1.0 mm FWHM DOI spatial resolution. Demonstration of such a high resolution PET module complements the simulation and experimental efforts by others, showing that one can limit the effects of the parallax error on the reconstruction image blurring. Our focus and need for such a compact high DOI resolution PET module is for the prostate PET magnifying probe working in conjunction with either a dedicated PET imager or a standard clinical PET/CT imager, aiding in prostate cancer diagnosis and biopsy guidance. Similar solutions can be as well implemented in PET probes imaging vulnerable plaque in carotid artery, in breast PET imaging probes, and in other applications.

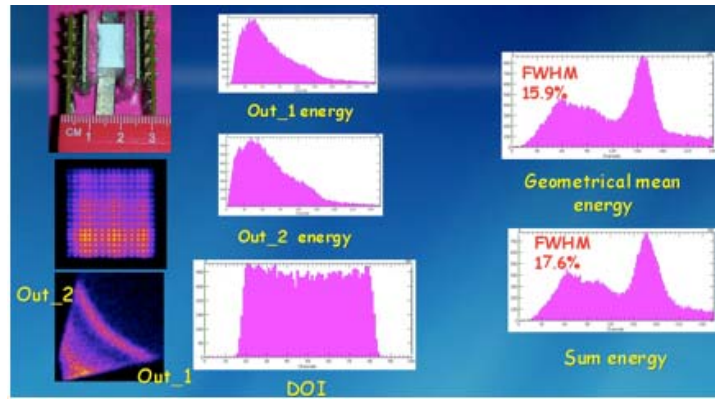
Report 3: Development of a “Resistive” Readout for SiPM Arrays

Abstract. We are developing the charge division (“resistive”) readout for several arrangements of SiPM arrays, based on devices from Hamamatsu and SensL. The difficulty with the SiPM arrays, as opposed to position sensitive photomultipliers (PSPMTs), is that the noise level is known to be high, and signal to noise ratio (S/N) is lower than in PMTs. In addition, the S/N decreases quickly with the increasing size of the module. Key parameters to optimize are: size and coverage of the arrays, operational temperature (potential necessity of introducing system cooling) and bias voltage. All these parameters have impact on the S/N, and in consequence on the spatial resolution and the energy resolution of the detector modules. Our somewhat arbitrary but practical goal is to achieve operation similar to the H8500/H9500 flat panel PSPMTs when using LYSO scintillation arrays in applications to small PET imaging modules. Ultimately we would like to use the reduced channel number readout in the depth-of interaction (DOI) modules. Our first application is to construct $\sim 5\text{cm} \times 5\text{cm}$ compact PET modules for the HelmetPET brain imager prototype under construction at WVU.

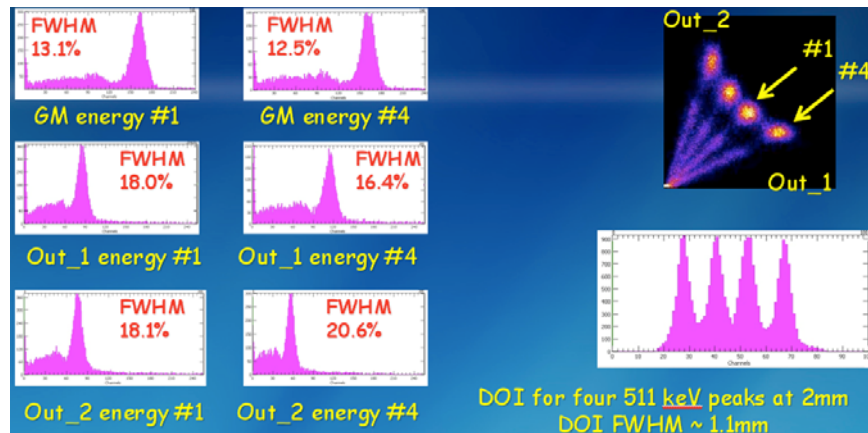
All the results shown below were obtained with the FPGA DAQ system and data acquisition software developed initially for the WVU PEM/PET breast imaging system by the Jefferson Lab group. The DAQ modules are now available from AiT Instruments. Two types of SiPM modules were used: S10943-9059(X) 25 MPPC from Hamamatsu and SPMArray4 from SensL.



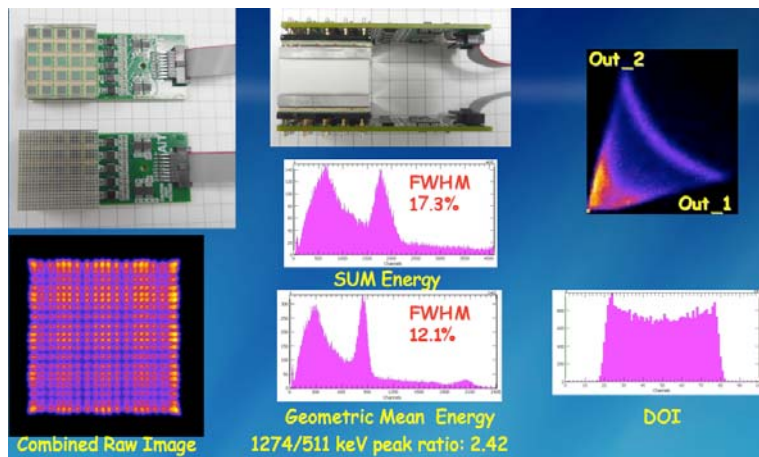
The photo at left shows resistive readout prototype from AiT Instruments for the S10943-9059(X) 25 MPPC module shown here with 1.0x1.0x10mm LYSO pixel array from Proteus, and a 2.8mm spreader window. Tests were performed at ~25 deg C using USB2 FPGA DAQ readout available from AiT. Center: Preliminary results with LYSO 1.5x1.5x10mm pixel array with 2.8mm spreader window, wet coupling (optical grease). Raw images and examples of single pixel energy spectra. Right: the same for the 1mm LYSO array. Good spatial and energy resolution was demonstrated.



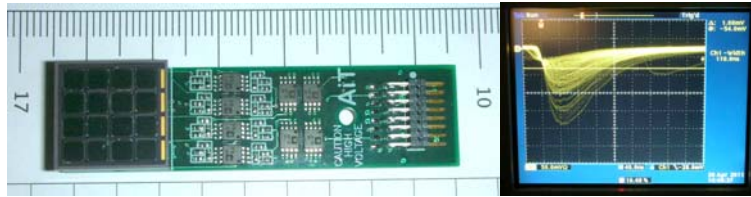
Preliminary results with two charge division modules coupled to two sides of the LYSO 1.0x1.0x10mm 16x16 pixel array optimized for DOI operation, through 2.8mm spreader windows with wet coupling (optical grease). Un-collimated Na22 beam. Energy outputs from both sides of the pixels show the expected wide amplitude spectra. The raw images from both sides (only one shown) permit for sufficient separation of the individual LYSO pixels.



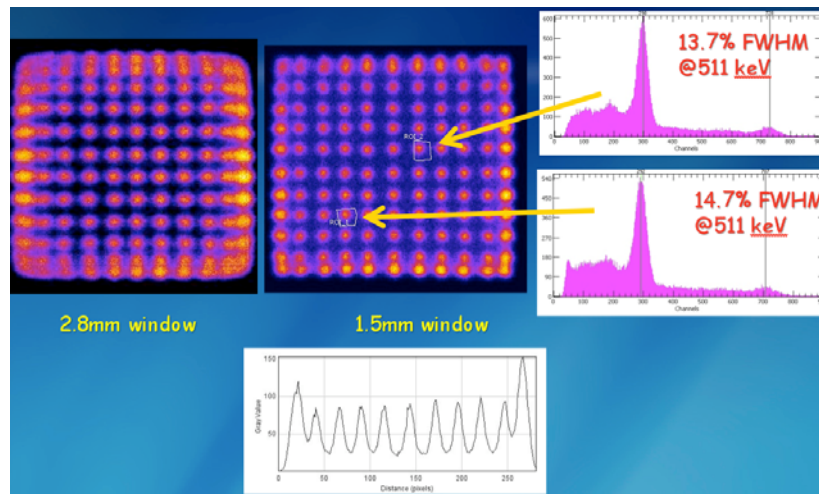
The 1.0x1.0x10mm DOI LYSO pixel array was probed with a highly electronically collimated scanning 511 keV gamma beam. The beam was moved along the 10mm length of the scintillation pixels with a 2mm step. Examples of energy spectra from one selected LYSO pixel are shown.



1" module with double-sided resistive readout. Two resistive 25 MPPC modules coupled to the LYSO array of 24x24 1x1x10mm pixels. Wide Na22 gamma beam. Geometric mean of the two output signals (shown here for one selected 1x1x10mm pixel) provides better measure of the event energy.



Charge division readout board developed for the SensL SPMArray4 module having an array of 4x4 3mm SiPM pixels. Examples of summed signals obtained with a LYSO array. 40ns/div.



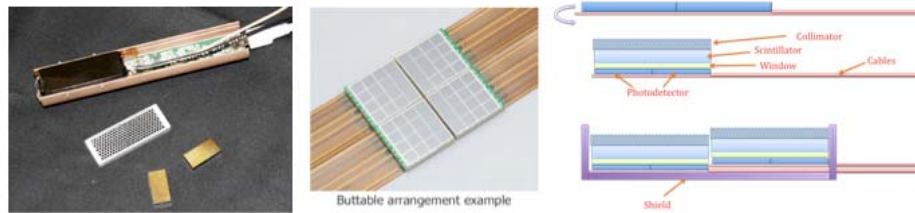
Results with the 1mm LYSO array, using two spreader windows: 2.8mm at left and 1.5mm at right. Good pixel separation and good energy resolution of ~14% FWHM @511 keV was obtained.

We believe that the above pilot results indicate that PET imaging modules with sizes up to 5cm and based on SiPMs and LYSO scintillators are feasible, with intrinsic resolution approaching 1mm, using economical charge division readout. Final work towards this goal, both with MPPC and SensL arrays, will be performed next. We are going also to define the limit of the technique when applied to the DOI capable modules.

Report 4: Development of a Mini Gamma Camera for Prostate Imaging

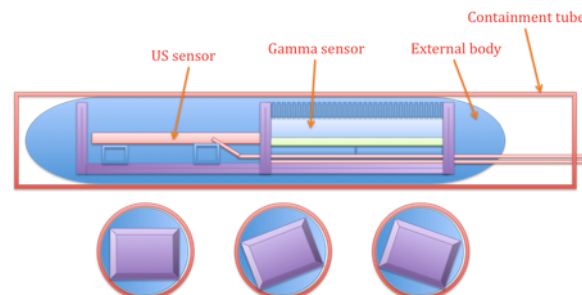
Abstract. We have tested a concept of a gamma mini-camera based on monolithic arrays of MPPCs from Hamamatsu. CsI(Tl), and Cs(Na) arrays and a thin scintillation GSO plate were tested with 122 keV gammas from ^{57}Co sources. The application requires placement of this mini-camera in an endorectal probe and requires very compact package and high intrinsic spatial resolution. The high sensitivity and high granularity collimator and gamma shield made out composite material (tungsten powder with epoxy) completes the detector package. We are developing the dual modality (hybrid) imaging prostate probe combining in one compact device the compact high resolution and high efficiency single gamma imager with an Ultrasound (US) sensor. The US component will typically provide not only the usual structural 3D information, as the standard TransRectal Ultrasound (TRUS) probe, but also the tissue differentiating information through proper US signal analysis, such as elastography. The mini gamma probe will provide

the direct metabolic information related to the biological state of the prostate and specifically about the presence of any cancerous structures exhibiting increased metabolic activity, when used with the single gamma labeled dedicated imaging agents for prostate cancer. In addition to cancer diagnosis, the dual-modality Gamma/US prostate probe can be used in biopsy and in surgical guidance.

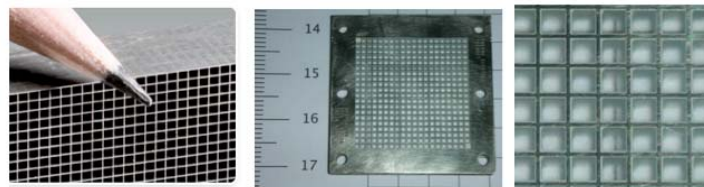


Recently, Hybridyne introduced to the market (FDA approval was obtained in Spring of 2010) a prostate mini gamma probe based on Cadmium Zinc Telluride (CZT) Technology (<http://www.hybridyneimagingtechnologies.com/>). However, the way how the probe was implemented with the associated electronics, there is no room for the addition of an US sensor in the same package. On the other hand, the SiPM/scintillator technology allows for more flexibility in choosing and modifying the detector structure.

The photo at left shows two multi-pixel CZT detector arrays and collimator used in the Hybridyne system. Shown in center is the buttable arrangement of four Hamamatsu monolithic MPPC arrays. After redirecting by 180 degrees the two left cables from the structure in the picture, as shown at top right, and adding a scintillator and a collimator, a ~1" detection module is obtained. Two of these modules can be stacked one behind the other to form a larger ~1" x 2" module, but with a small gap and step in between. An external gamma shield needs to be added to prevent gamma radiation to bypass the collimator and enter the scintillator from the sides and the back of the probe.



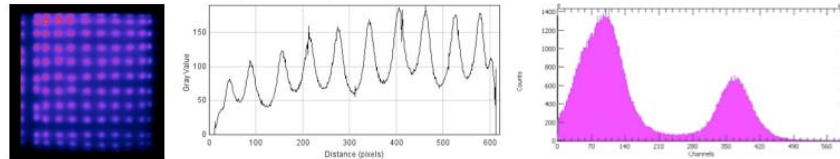
In a serial implementation of the dual modality package with US, the US sensor will be placed preferentially in front of the package, with the gamma part behind. Positioning sensors (not shown) will keep a track of the probe position and enable fusion of the images obtained from the two modalities. To stabilize prostate during imaging, the hybrid probe can be inserted inside a thin-shell UV-compatible containment tube that would stay in place during the procedure, secured by an arm mounted to the patient's table, while the Gamma/US probe will be moved along the tube or even rotated to achieve better viewing of different parts of prostate.



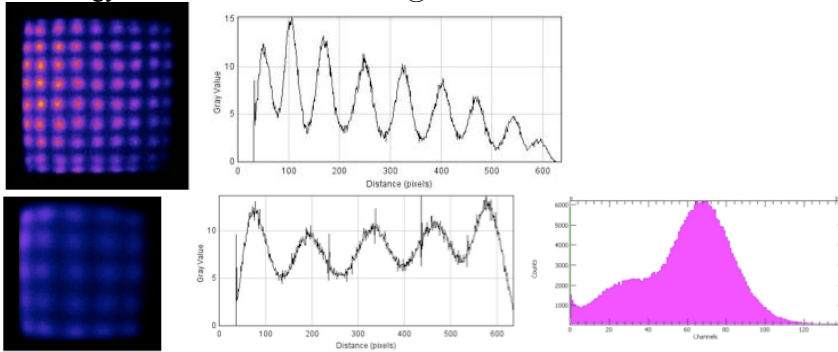
Tungsten composite collimator technology from Mikro Systems. High granularity of the produced structures well matches the high resolution of the scintillation sensor. The composite tungsten collimators available from Mikro Systems in Charlottesville, VA (<http://www.mikrosystems.com/applications/computed-tomography>) are a good match for the needs of this high resolution and compact gamma camera. Top view of the practical example of the special variant of the scintillation/collimator package, where the scintillator elements (CsI(Tl) or CsI(Na)) are imbedded in the collimator structure. Collimator septa function in this case also as separating walls of the individual scintillator pixels. To optimize the scintillation light transmission and collection, the surface of the septa is covered with reflective white material/paint. This design permits the most compact (in vertical

dimension) structure of the collimator/scintillator package. Mikro Systems is one of the companies custom-making such structures.

We have performed initial laboratory validation of the gamma probe sensor of the new design. First, the monolithic Hamamatsu SiPM module, Model MPPC-MA1-1(X), was coupled through a 2mm thick light spreader window to a 1mm step 3mm thick CsI(Tl) array from Hilger Crystals, UK. Then, we tested the 1.2mm step CsI(Tl) array imbedded in the collimator, as seen in the figure above, also coupled through a 2mm window, and using optical grease between all optical surfaces. Finally, a 1mm thick 20mm x 20mm GSO plate was also tested. The advantage of the latter design using plate GSO is that the whole structure becomes very compact, benefiting from high stopping power of GSO.

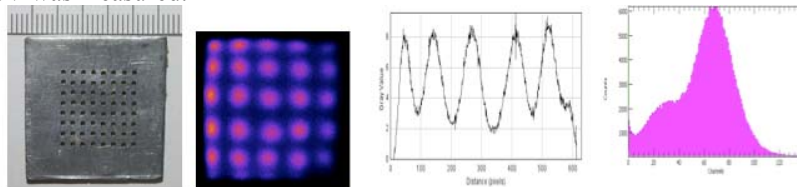


Results obtained with the 1mm step 3mm thick CsI(Tl) scintillation array tested with the Co57 source (122 keV gammas). The array is made out of several joined sections that produce the observed discontinuities in the images. The CsI(Tl) array was coupled to the monolithic MPPC array from Hamamatsu via a 2mm spreader window. Dry coupling was used. Raw image at left and vertical profile through one of the pixel columns in the center, demonstrate sub-mm intrinsic spatial resolution. The energy spectrum from one of the 1x1x3mm CsI(Tl) pixels at right shows scattered radiation peak at left and photopeak at right with energy resolution 19.5% FWHM @ 122 keV.



Results obtained with the 1.2mm step 3mm thick CsI(Na) scintillation array tested with the Co57 source. The array was coupled to the monolithic MPPC array from Hamamatsu via a 2mm spreader window. Wet (optical grease) coupling was used. Raw image at left and profile through one of the pixel rows in the center, again demonstrate sub-mm intrinsic spatial resolution.

Results obtained with the 1mm thick GSO scintillator plate tested with the Co57 source. The plate was coupled to the monolithic MPPC array from Hamamatsu via a 2mm spreader window. Wet coupling was used. Raw image at left is the image of a 1mm thick lead masks having an array of 1mm diameter holes, spaced at 2mm center-to-center. Vertical profile through one of the columns shown in the center, is demonstrating sub-mm intrinsic resolution of this solution. Overall energy resolution (no region selection) of 36% @122 keV was measured.



Results obtained with the 1mm thick GSO scintillator plate tested with the Co57 source. The plate was coupled to the monolithic MPPC array from Hamamatsu via a 1mm spreader window. Wet coupling (optical grease) and white diffusing paper on top of the scintillator plate were used. Raw image at left is the image of a 1mm thick lead mask having an array of 1mm diameter holes, spaced at 2mm center-to-center (shown at left). Vertical profile through one of the columns shown at center, is demonstrating sub-mm intrinsic resolution of this mini-imager. Central region energy resolution of 36% @122 keV was measured.

The above pilot results demonstrate that compact gamma imaging probes based on SiPMs and scintillators for prostate imaging applications with 1mm intrinsic resolution are feasible, while the overall spatial

resolution (and sensitivity) will be defined by the collimator design and geometry (the distance to lesion). Additional work on improving energy resolution will be performed next.

Aim 3: Probe demonstrator construction

Probe interfacing to PET ring at Michigan

As noted in the Overview, we are somewhat behind in this task (due both to scheduling conflicts and the March 2011 graduation of the student involved with this project). Nevertheless, remaining work should proceed quickly and we do not expect that the delay will prevent achievement of the project goals. In last year's report, we described the existing data acquisition system for the instrument shown in Fig. 1. As of June 2011, all electronics boards required for interfacing the probe detectors to this system are complete. While some alterations to the FPGA firmware and data acquisition software will be required, these are rather straightforward and should be easily accomplished with planned personnel (we are planning to hire our recent graduate as a short-term postdoctoral fellow for this project). The team at WVU has developed a method of interfacing their probes that requires only standard hardware that plugs into our VME-based data acquisition system.

Mechanical fabrication of the platform for mounting the phantom and probe on a turntable within the partial-ring BGO system (essentially replacing the "inner-ring" and turntable shown in Fig. 1) is straightforward but yet to be completed.

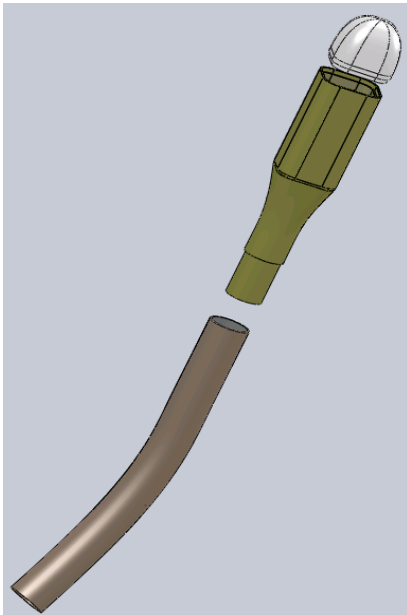


Figure 9. Mechanical drawing for probe housing developed in Biomedical Engineering design class. Prototypes have been fabricated in black Delrin.

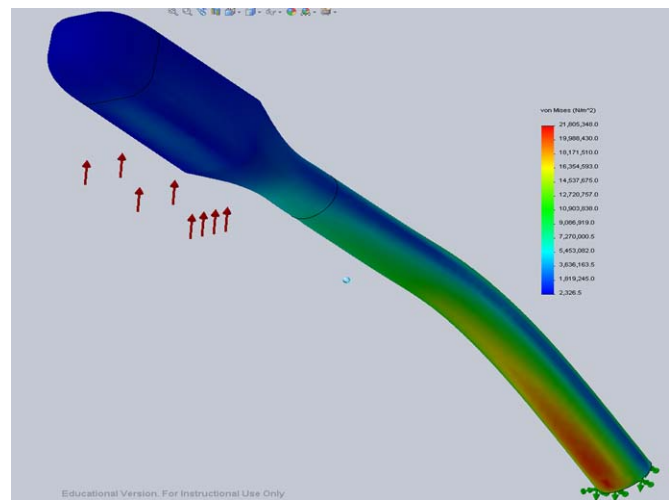


Figure 10. Finite element testing of probe housing for mechanical strength assuming probe will be clamped at base of handle.

Probe adaptation for human use

At Michigan, we were fortunate to enlist the assistance of a student team from the two-semester Biomedical Engineering Capstone Design course to refine the probe for possible future testing in human subjects. This involved meeting with urologists to refine the allowable probe dimensions, exploring materials with which to construct the housing (evaluating strength, moisture resistance, etc.), and evaluating potential hardware for tracking the probe orientation and position relative to the external PET ring. Moreover, an initial FMEA was done on the proposed device which should help with the IRB application.

Mechanical design of the probe housing for detectors under construction at WVU is shown in Fig. 9 and finite element modeling for mechanical strength is shown in Fig. 10. Final material chosen for constructing probe housings is lightproof black Delrin. Several prototype housings have been fabricated and an appropriate housing will be used to shield the detector delivered by WVU.

Unlike the planned phantom studies, a prostate probe for human use will require that its position and orientation relative to the external PET ring be tracked as a function of time. Errors in probe location will of course introduce reconstruction artifacts and loss of resolution. Numerous tracking methods exist and each has advantages and pitfalls. The student team examined the performance of a DC magnetic tracking system for this task with two different sensors. A plastic model of the probe detector and housing were constructed using a 3D rapid prototyping system. Two tracking sensors were attached to this model (either a pair of the standard larger sensors (~5mm), or a pair of smaller sensors (<2mm). The model was then attached to a computer-controlled arm and measurements of position were acquired and analyzed over a 40cm x 40 cm range. Results of this investigation, shown in Fig. 11, demonstrate only small errors over this range providing confidence that magnetic tracking is adequate but more detailed studies in the actual PET scanning environment are necessary. Preliminary indications are that use of the smaller sensors leads to unacceptable errors in positioning due to both their noise and limited field-of-operation in comparison with the standard sensors.

Aim 4: Phantom studies and performance evaluation

Initial phantoms have been developed and will be imaged on the integrated probe instrument in the upcoming year.

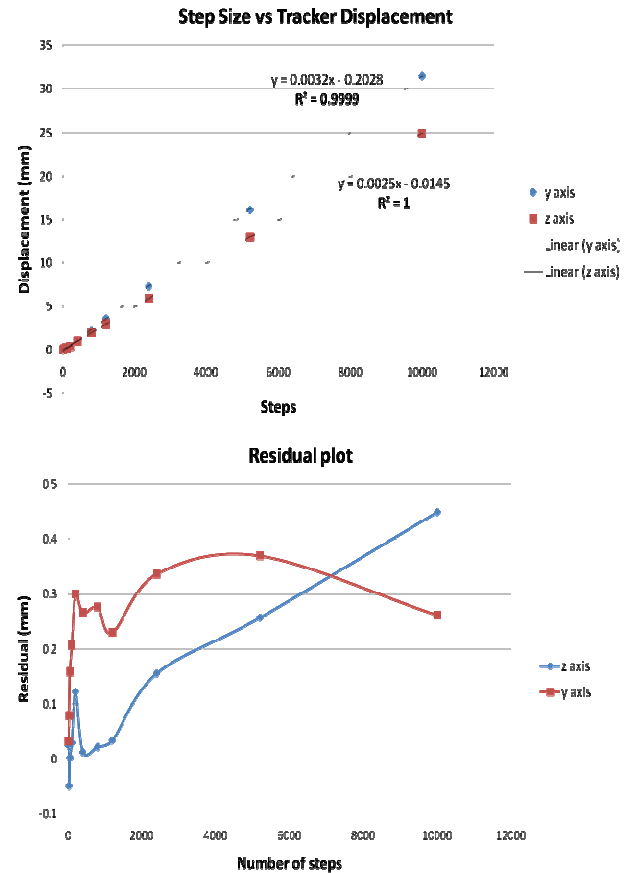


Figure 11. Results from tracking system measurements conducted throughout 40cm x 40cm field-of-view. Positioning errors appear acceptable for use with PET prostate probe.

Key Research Accomplishments

- The PET “magnifying glass” principle, which underlies much of the anticipated advantage of the probe was demonstrated on the partial-ring PET system at Michigan. Although, the principle had previously been shown using Monte Carlo modeling and reconstruction, it has now been verified in hardware that will be used for the probe demonstrations.
- 3D PET reconstruction has been developed and preliminary tests with probe configurations have been conducted.
- Initial design studies for human use have been conducted. This will accelerate application of this technology to human subjects after laboratory demonstrations have been completed.
- Several working probe PET prototypes were built and tested, with the highlight: achieving for the first time sub-mm (0.7mm) resolution in all three dimensions

REPORTABLE OUTCOMES

Publications, abstracts, and presentations

1. Studen A, Chesi E, Cindro V, Clinthorne NH, Cochran E, Grosicar B, Honscheid K, Kagan H, Lacasta C, Llosa G, Linhart V, Mikuz M, Stankova V, Weilhammer P, Zontar D: A silicon PET probe. *Nucl. Ins. Meth. Phys. Res. A*, doi:10.1016/j.nima.2010.11.073, To appear.
2. Garibaldi F, De Leo R, Ranieri A, Loddo F, Floresta M, Tamma C, Gabrielli A, Giorgi F, Cusanno f, Musico P, Perrino R, Finocchiaro P, Cosentino, L, Pappalardo A, Meddi F, Maraviglia B, Giove F, Gili T, Capuani S, Turisini M, Clinthorne N, Huh S, Majewski S, Lucentini M, Gricia M, Giuliani F, Monno E: TOPEM: a multimodality probe (PET TOF, MRI and MRS) for diagnosis and follow up of prostate cancer. *IEEE Nuclear Science Symposium Conference Record*, 2010.
3. Huh SS, Cochran E, Honscheid H, Kagan H, Smith S, Rogers WL, Clinthorne NH: The first generation prototype of a surgical PET imaging probe system. *IEEE Nuclear Science Symposium Conference Record*, 2010.
4. Studen A, Chesi E, Cindro V, Clinthorne NH, Cochran E, Grosicar B, Honscheid K, Huh SS, Kagan H, Lacasta C, Llosa G, Linhart V, Mikuz M, Stankova V, Weilhammer P, Zontar D: Report on the MADEIRA PET probe. *IEEE Nuclear Science Symposium Conference Record*, 2010.
5. Lacasta C, Clinthorne NH, Llosa G: The PET Magnifier Probe (Chapter 11), in *Radiation Physics for Nuclear Medicine*, Cantone MC, Hoeschen C (eds), Springer, 2011
6. Garibaldi F, et al, TOPEM: a PET TOF endorectal probe, compatible with MRI and MRS for diagnosis and follow up of prostate cancer, *Presented at the World Molecular Imaging Conference (WMIC), September 11–15, 2010 Kyoto, Japan*.
7. Cochran E, Chesi E, Clinthorne NH, Honscheid H, Huh S, Kagan H, Lacasta C, Mikuz M, Rackers J, Smith S, Studen A, Weilhammer P, Wolf E: High resolution PET using concentric silicon and scintillator rings. *Presented at the 2010 IEEE Nuclear Science Symposium, Oct. 25–31, 2010, Knoxville, TN USA*.
8. Clinthorne NH, Majewski S, Brzezinski K, Huh SS, Carr J, Chen Z, Salomonnnson E, Yande A: High resolution PET instruments for prostate imaging. *Presented at the 2011 IMPaCT Conference, March 9–12, 2011, Orlando, FL*.

9. Clinthorne NH, Cochran E, Kagan H, Huh SS, Lacasta C, Linhart V, Mikuz M, Smith D, Studen A, Weilhammer P: Recent results from a “dual-ring” high resolution PET demonstrator. *Presented at the 2011 Annual Meeting of the Society of Nuclear Medicine, June 3-8, 2011, San Antonio, TX.*
10. Clinthorne N, Cochran E, Chesi E, Grosicar B, Honscheid K, Huh S, Kagan H, Lacasta C, Brzezinski K, Linhart V, Mikuz M, Smith DS, Stankova V, Studen A, Weilhammer P, Zontar D: A high-resolution PET demonstrator using a silicon "magnifying glass." *Presented at Technology and Instrumentation in Particle Physics (TIPP 2011), June 9-14, 2011, Chicago, IL.*
11. Clinthorne N, Majewski S, Stolin A, Raylman RR, Carr J, Chen Z, Salomonsson E, Yande A, Huh SS, Kagan H, Smith S, Brzezinski K, Studen A: Progress in development of a high-resolution PET prostate imaging probe. *To be presented at the 2011 IEEE Nuclear Science Symposium, October 23-29, 2011, Valencia, Spain.*

Other reportable outcomes

1. A Michigan Biomedical Engineering graduate student who did much of the initial work on prostate probe evaluation, developing real-time reconstruction, and alternative high-resolution PET imaging probes obtained his Ph.D. in early-April 2011.
2. The former head of Urology at Michigan has expressed strong interest in having such a probe and in combining the information with MRI/MRS.

CONCLUSIONS

Several key demonstrations were accomplished this year including demonstration of the PET magnifier concept, multiresolution image reconstruction, and much extended beyond the initial narrow scope performance of the PET probes. Indeed we built several side prototype imagers with panel modules operating with probes. In addition, the results of the probe studies are now transplanted into the other projects, such as dedicated brain and breast imagers, as well as small animal PET-MRI imager. Although we are not as far along in the integration process as desired, the remaining work should progress much more rapidly in Year 3 with the ultimate goal being an instrument that will be straightforward to adapt to testing in prostate cancer patients in our follow-on investigations.

APPENDICES

1. Studen A, Chesi E, Cindro V, Clinthorne NH, Cochran E, Grosicar B, Honscheid K, Kagan H, Lacasta C, Llosa G, Linhart V, Mikuz M, Stankova V, Weilhammer P, Zontar D: A silicon PET probe. *Nucl. Ins. Meth. Phys. Res. A*, doi:10.1016/j.nima.2010.11.073, Preprint – in press.
2. Garibaldi F, De Leo R, Ranieri A, Loddo F, Floresta M, Tamma C, Gabrielli A, Giorgi F, Cusanno f, Musico P, Perrino R, Finocchiaro P, Cosentino, L, Pappalardo A, Meddi F, Maraviglia B, Giove F, Gili T, Capuani S, Turisini M, Clinthorne N, Huh S, Majewski S, Lucentini M, Gricia M, Giuliani F, Monno E: TOPEM: a multimodality probe (PET TOF, MRI and MRS) for diagnosis and follow up of prostate cancer. *IEEE Nuclear Science Symposium Conference Record*, 2010.
3. Huh SS, Cochran E, Honscheid H, Kagan H, Smith S, Rogers WL, Clinthorne NH: The first generation prototype of a surgical PET imaging probe system. *IEEE Nuclear Science Symposium Conference Record*, 2010.

4. Studen A, Chesi E, Cindro V, Clinthorne NH, Cochran E, Grosicar B, Honscheid K, Huh SS, Kagan H, Lacasta C, Llosa G, Linhart V, Mikuz M, Stankova V, Weilhammer P, Zontar D: Report on the MADEIRA PET probe. *IEEE Nuclear Science Symposium Conference Record*, 2010.
5. Clinthorne N, Majewski S, Stolin A, Raylman RR, Carr J, Chen Z, Salomonsson E, Yande A, Huh SS, Kagan H, Smith S, Brzezinski K, Studen A: Progress in development of a high-resolution PET prostate imaging probe. *To be presented at the 2011 IEEE Nuclear Science Symposium, October 23-29, 2011, Valencia, Spain*. Summary paper.
6. Clinthorne N, Cochran E, Chesi E, et al: A high-resolution PET demonstrator using a silicon “magnifying glass.” *Submitted to Physics Procedia, Proceedings of the 2011 conference on Technology and Instrumentation in Particle Physics (TIPP 2011)*, Chicago, IL June 9–14, 2011.



Contents lists available at ScienceDirect

Nuclear Instruments and Methods in Physics Research A

journal homepage: www.elsevier.com/locate/nima

A silicon PET probe

A. Studen^{a,*}, E. Chesi^b, V. Cindro^a, N.H. Clinthorne^c, E. Cochran^b, B. Grošičar^a, K. Honscheid^b, H. Kagan^b, C. Lacasta^d, G. Llosa^d, V. Linhart^d, M. Mikuž^{a,e}, V. Stankova^d, P. Weilhammer^b, D. Žontar^a

^a Jožef Stefan Institute, Ljubljana, Slovenia

^b The Ohio State University, Columbus, OH, USA

^c The University of Michigan, Ann Arbor, MI, USA

^d IFIC/CSIC-UVEG, Valencia, Spain

^e The University of Ljubljana, Ljubljana, Slovenia

ARTICLE INFO

Keywords:

PET

Silicon detectors

ABSTRACT

PET scanners with high spatial resolution offer a great potential in improving diagnosis, therapy monitoring and treatment validation for several severe diseases. One way to improve resolution of a PET scanner is to extend a conventional PET ring with a small probe with excellent spatial resolution. The probe is intended to be placed close to the area of interest. The coincidences of interactions within the probe and the external ring provide a subset of data which combined with data from external ring, greatly improve resolution in the area viewed by the probe.

Our collaboration is developing a prototype of a PET probe, composed of high-resolution silicon pad detectors. The detectors are 1 mm thick, measuring 40 by 26 mm², and several such sensors are envisaged to either compensate for low stopping power of silicon or increase the area covered by the probe. The sensors are segmented into 1 mm³ cubic voxels, giving 1040 readout pads per sensor. A module is composed of two sensors placed in a back-to-back configuration, allowing for stacking fraction of up to 70% within a module. The pads are coupled to a set of 16 ASICs (VaTaGP7.1 by IDEAS) per module and read out through a custom designed data acquisition board, allowing for trigger and data interfacing with the external ring.

This paper presents an overview of probe requirements and expected performance parameters. It will focus on the characteristics of the silicon modules and their impact on overall probe performance, including spatial resolution, energy resolution and timing resolution. We will show that 1 mm³ voxels will significantly extend the spatial resolution of conventional PET rings, and that broadening of timing resolution related to varying depth of photon interactions can be compensated to match the timing resolution of the external ring. The initial test results of the probe will also be presented.

© 2010 Elsevier B.V. All rights reserved.

1. Introduction

The spatial resolution is an important characteristics of a PET scanner. In early 2000's (all numbers according to NEMA NU 2-2001 Performance Measurement of Positron Emission Tomographs standard [1]) the bar was set at around 6 mm at the center of the field-of-view (FOV) by either BGO [2] or LSO [3] based scanners. The resolution is closely related to the size of the sensitive material segmentation, so smaller crystals are used to improve the resolution. In state-of-the-art whole-body scanners a resolution of 4 mm [4,5] is achieved at the expense of 2–3 fold increase of crystal count, reflected in increased complexity of the associated readout. Alternatively, dedicated high-resolution scanners achieve high-resolution by sacrificing the size of the FOV, as in a brain imager like

Siemens' HRRT at 2 mm resolution [6], or pre-clinical devices like micro PET at 1 mm [7] or Siemens Inveon at 1.8 mm [8].

The PET probe is an emerging concept [9–12], where the large FOV of the basic scanners is combined with a dynamically allocated small region of interest where spatial resolution compares to dedicated small FOV devices. The principle is illustrated in Fig. 1. The external ring, illustrated with big cubes, represents conventional PET ring detectors. The small cubes, placed inside the big ring, represent the high spatial resolution detectors, equipped with a motion tracker to register their positions with respect to the external ring. The line of response for the conventional ring is painted in dark shade of gray and labeled ring–ring, while the line of response for an event that interacted in probe on one side and in the ring on the other side, is painted light gray and labeled probe–ring. One can appreciate that the volume contained in the probe–ring response is much smaller than in the ring–ring response, hinting at the improved image quality for events obtained in the ring. Further discussion will assume a recent whole-body human

* Corresponding author. Tel.: +386 1 477 3162.

E-mail address: andrej.studen@ijs.si (A. Studen).

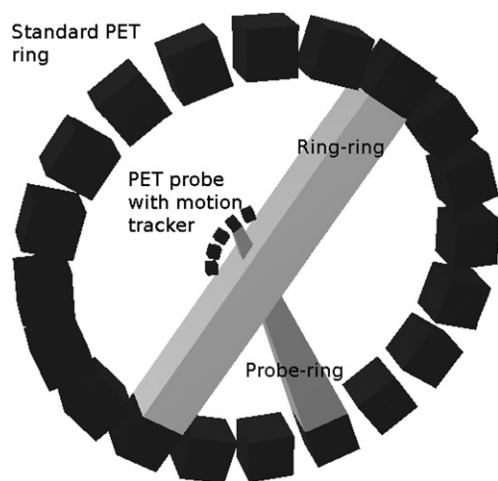


Fig. 1. Illustration of the Pet probe insert principle. Description in the text.

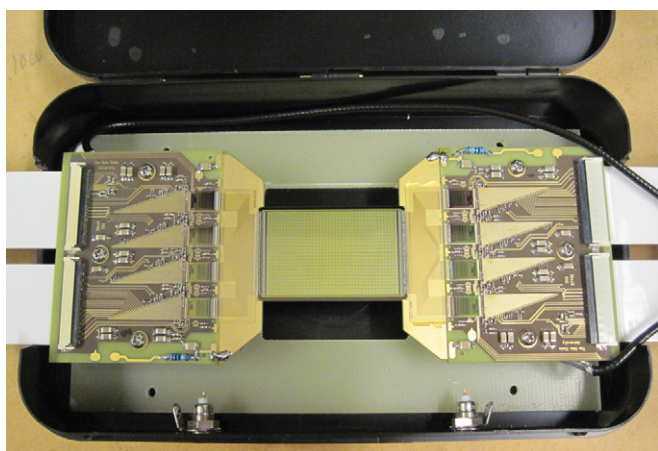


Fig. 2. Photograph of a single detector module of the probe prototype.

PET scanner [4,5] extended with a probe as described in the following text.

Within the MADEIRA collaboration a probe detector prototype was developed with a single module shown in Fig. 2. The sensitive part of each module is a pair of sensors, each measuring 40 by 26 mm², 1 mm thick, placed back-to-back with a separation around 0.8 mm. Each sensor is segmented into 1040 1 mm² square pads. The pads are read out through eight application specific integrated circuits (ASICs) per detector. ASICs are called VATAGP7.1 and designed and manufactured by Gamma-Medica-Ideas [13]. Each ASIC hosts 128 parallel readout channels, each channel composed of a common charge-sensitive amplifier, its output split into two shaper lines. The fast shaper with a shaping time of 150 ns is fed into a leading edge discriminator for a trigger signal, which is OR-ed among all channels on the ASIC. The slow shaper has a shaping time of 500 ns and is buffered through a sample and hold circuit via a shift register to the analog output. The ASICs are placed four per board on a custom made PCB. A total of 16 ASICs is required per module, and multiple modules are envisaged for higher probe efficiency. Downstream electronics is routed through VME crate and connected to a PC, which is used as control and storage device. Evaluation of the sensor and electronics can be found in Ref. [14].

This paper will compare the properties of the described prototype to the requirements posed by the PET probe principle. This introduction is followed by evaluation of the spatial uncertainty of the line of response of probe–ring events, a discussion on probe sensitivity compared to the external ring, description of a strategy

to remove scattered events, followed by characterization of impact of timing properties of the probe. In summary, the overall effectiveness of the probe is estimated.

2. Spatial resolution of the probe–ring events

We want to estimate the intrinsic resolution of the line of response between a probe (1) and a ring (2). The resolution of both is given as $\sigma_{D,1}$ and $\sigma_{D,2}$ along the depth, and $\sigma_{C,1}$ and $\sigma_{C,2}$ on the detector face (circumference resolution). We are assuming an annihilation at a distance d_1 from the first, and d_2 from the second sensor, both parameters described by the total distance $d = d_1 + d_2$ and $\alpha = d_1 / (d_1 + d_2)$. We also want to account for impact angles, θ_1 and θ_2 , defined versus line perpendicular to detector face. Using geometry one can show that the FWHM of the resolution uncertainty in the direction perpendicular to the line of response is

$$R_D = 2.35 \sqrt{((1-\alpha)^2(\sin^2\theta_1\sigma_{D,1}^2 + \cos^2\theta_1\sigma_{C,1}^2) + \alpha^2(\sin^2\theta_2\sigma_{D,2}^2 + \cos^2\theta_2\sigma_{C,2}^2))}. \quad (1)$$

The resulting resolution variation along the line connecting the detector pair is given in Fig. 3. The resolution of the ring detector was taken to be $\sigma_{C,2} = \sigma_{D,2} = 6$ mm and the total separation d of the detectors was 40 cm. Three curves are shown for probe resolutions $\sigma_{D,1} = \sigma_{C,1} = 1, 2$ or 3 mm FWHM. The uncertainty remains small even for substantial distances (5–10 cm) of probe from the annihilation position. Another benefit of the probe arrangement is that close to the probe the acollinearity uncertainty, approximated as $R_A \approx 0.0088 \cdot d_1 d_2 / (d_1 + d_2)$, is fairly small, 0.66 mm at 10 cm, and since it has to be added in quadrature to the total uncertainty, the plot in Fig. 3 can be viewed as the total uncertainty of the line of response.

By using pads with 1 mm side, the expected resolution of the probe–ring events is 1–1.5 mm, depending on the distance. The inherent spatial resolution, however, is not always reflected in actual reconstructed images. For the reconstruction the dominant ring–ring events have to be combined with the probe–ring events to alleviate the limited angle tomography artifacts. The important phenomena to be aware of is the variance–resolution trade-off, which will be influenced by many factors, the portion of the probe data relative to ring data and the properties of the imaged object itself among others which makes it hard to assess the reconstructed resolution in general. However, a study in small animal PET [12] showed a promising reduction in image variance with probe data

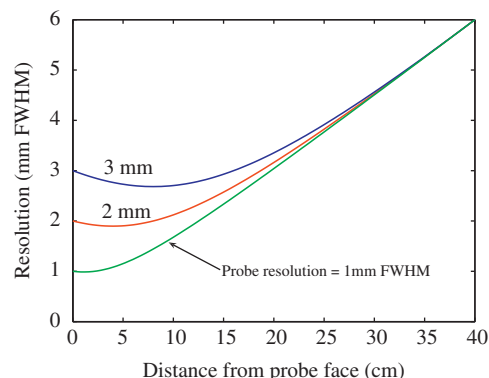


Fig. 3. The uncertainty of the line of response in the direction perpendicular to the line of response. Horizontal axis is the distance of the annihilation from the face of the probe, and the vertical axis is the FWHM of the uncertainty. Spatial resolution of 6 mm is assumed for the external ring. Curves for a probe with resolution of 1 mm (bottom) to 3 mm (top) FWHM are shown. To be compared with the resolution of dedicated high-resolution scanners at 1–2 mm as given in the introduction.

when targeted resolution (parameterized as bias in the cited study) is lowered in the reconstruction.

3. Efficiency of a silicon probe

To estimate the relative efficiency of the probe, we performed a Monte-Carlo simulation using Geant4 [15] to track the annihilation photons. Two detectors were used: a full 2 cm thick and 16 cm wide ring of LSO with a diameter of 80 cm and a single 1 mm thick layer of the 40 by 26 mm² probe. A note on orientation labeling: the direction along the ring axis is called down-to-up, and the ring plane is spanned by a back-to-front and a left-to-right axes. The probe was placed in the ring, displaced for 12 cm in back-to-front direction and centrally in all other directions. To estimate sensitivity, a barrel of water with elliptical cross-section was centered in the ring. The barrel was 60 cm long, the cross-section had a half-axis of 20 cm in left-to-right direction and 10 cm in back-to-front direction. Back-to-back photons were generated uniformly within the barrel. The following event properties were observed and recorded for each event:

- position of emission;
- scattering in the barrel prior to interaction;
- energy of interaction in sensitive detectors;
- energy of photons prior to interaction in the sensitive detectors.

Events were classified as clean if energy of photons prior to interaction in the sensitive detectors was above 450 keV, and scattered otherwise. Table 1 shows relative frequencies of different event types. The relative frequency (for a single probe layer) of probe–ring events was one in a thousand ring–ring events.

However, the distribution of probe–ring and ring–ring events within the barrel is significantly different, which is depicted in Fig. 4. The histograms in the figure are two slices (sagittal and

Table 1

The relative frequencies of event outcome for the generation of 2 million photon pairs. $\langle N \rangle$ stand for the number of events averaged over multiple runs. Recovered events N_{rec} and mis-recovered events $N_{mis-rec}$ are obtained for 100 keV threshold on energy in probe.

Event type	$\langle N \rangle$	N_{rec}	$N_{mis-rec}$
Probe only (singles)	218.6		
Ring only (singles)	632k		
Probe–ring (all)	40		
Probe (clean)–ring (any)	12.4	6.7	1.7
Probe (clean)–ring (clean)	3.1	1.6	0.6
Ring (any)–ring (any)	49k		
Ring (clean)–ring(clean)	4.6k		

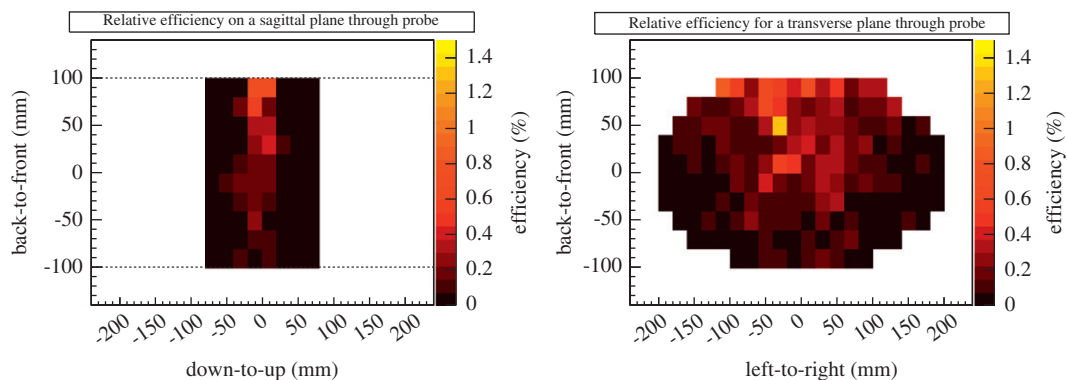


Fig. 4. Two slices (top: sagittal, bottom: transverse) of the three-dimensional voxel array giving ratio of clean probe–ring to ring–ring events for a single probe layer and conventional PET ring.

transverse) of the three-dimensional array of cubic voxels with a side of 2 cm. The content of each voxel is the ratio of clean probe–ring events to clean ring–ring events which originated within this voxel. Close to the probe (positive direction of back-to-front axis) the ratio is close to 1% for a single probe layer. For a 4–6 layer probe, the local efficiencies of 5% can be expected in regions close to the probe where the spatial resolution is excellent.

3.1. Classification of scattered events in a silicon probe

The most probable interaction of a 511 keV annihilation photon in a silicon detector is a Compton interaction, which prevents ordinary recognition of the scattered events as those with energy off the photo-peak. Nevertheless, we attempted to separate scattered and clean events based on interaction energy in the probe. Histogram in Fig. 5 shows distribution of simulated events with respect to the energy of the Compton electron. The dark-shaded histogram shows distribution for clean, non-scattered events, whereas the light-shaded histogram drawn on top is its equivalent for the scattered events. There is a clear tendency for non-scattered events to excite more energetic electrons, so a cut on the continuous spectrum is possible. The energy resolution in silicon probe is around 2 keV [14], sufficient for optimization on the energy cut. An arbitrary cut at 100 keV yields properly recovered (true-positives) and mis-recovered (false-positives) events given in Table 1.

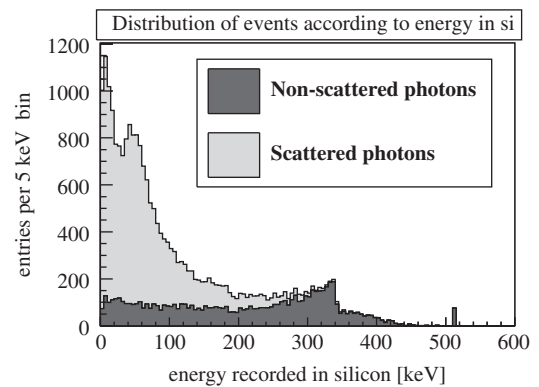


Fig. 5. Distribution of simulated events in probe according to energy in silicon detectors. The dark-shaded histogram shows clean, non-scattered events and light-shaded histogram, drawn on top, is the equivalent for scattered events.

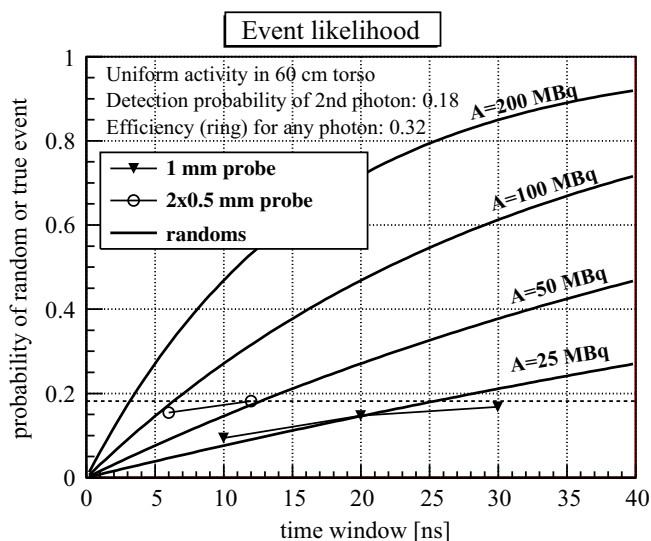


Fig. 6. Effect of imperfect timing resolution of the probe on collection of events. Probability of a random coincidence is shown with solid lines for the labeled total body activity. The inverted triangles show the comparable performance of a 1 mm thick probe, and open circles show the estimated performance of probe combined from a pair of detectors with half (0.5 mm) thickness. Dashed line shows the maximum possible probability of a probe-ring interaction, given by p_2 .

4. Timing properties

Timing of the probe is important in terms of coherence with an external ring. Results from previous section were used in determining the probability of (1) any photon from the barrel giving an interaction in the ring, $p_1 = 632k/2M = 0.32$ and (2) the second photon to interact in the ring if the first one interacted in the probe, $p_2 = 40/218.6 = 0.18$. We assume that a silicon interaction opens a time window with duration t_w . The probability of a random ring event is given as $p_R = 1 - \exp(-t_w p_1 A)$, where A is the total activity within the barrel (or the body) which is shown as solid curves in Fig. 6 for activities of 25–200 MBq. The maximum probability of a true event p_T within any t_w is given by p_2 . Any imperfection of the probe detector will further degrade p_T . In Ref. [16], the timing distributions for a silicon probe were estimated. Sliding a window with a duration of t_w over the distribution yields an optimum delay t_D such that the number of events N_D with trigger times between t_D and $t_D + t_w$ is maximal. Calculating the ratio of N_D to all coincidence events yields a degradation factor $p_D(t_w) = N_D/N_{all}$. In Ref. [16], the p_D were estimated for a 1 mm thick probes (labeled as efficiencies), and scaling them by p_2 yields an inverted triangle marked graph in Fig. 6. The p_D for a simulated pair of detectors with halved the thickness as simulated in Ref. [14] and scaled with p_2 is graphed with open circles, showing a significantly improved performance. Usefulness of current probe is limited to a setup, where the activity is below 25 MBq.

5. Summary

The PET probe concept aims at extending the spatial resolution of a general purpose PET scanner in a dynamically allocated region of interest. The expected resolution equals that of the probe detector to within 10 cm of the probe, and furthermore, the

resolution is not degraded by negligible acollinearity contribution at such short distances. A probe made of segmented silicon detector can provide spatial resolution of 1 mm FWHM, comparable to dedicated high-resolution PET scanners, and reasonable thicknesses of detectors provide sensible portions of probe-ring data in ring-ring data set. By using the energy resolution of the silicon probe, the events scattered prior to probe interaction can be distinguished from scattered events with reasonable efficiency. Timing of the probe is important, and silicon probe can only operate at moderate administered activities. Alternatives without sacrificing the other beneficial properties are possible and will be evaluated. Nevertheless, the current silicon probe is well adapted to the requirements of the probe concept, providing a moderate object radioactivity, and will provide experimental means to confirm the expected PET probe benefits.

Acknowledgments

The work was carried out within the Collaborative Project “MADEIRA” (www.madeira-project.eu), co-funded by the European Commission through EURATOM Seventh Framework Programme (Grant agreement FP7-212100).

References

- [1] National Electrical Manufacturers Association, Roslyn, VA, NEMA Standards Publication NU-2: Performance Measurements of Positron Emission Tomographs, 2001.
- [2] O. Mawlawi, D.A. Podoloff, S. Kohlmyer, J.J. Williams, C.W. Stearns, R.F. Culp, H. Macapinlac, *J. Nucl. Med.* 45 (10) (2004) 1734.
- [3] Y.E. Erdi, S.A. Nehmeh, T. Mulnix, J.L. Humm, C.C. Watson, *J. Nucl. Med.* 45 (5) (2004) 813.
- [4] S. Surti, A. Kuhn, M.E. Werner, A.E. Perkins, J. Kolthammer, J.S. Karp, *J. Nucl. Med.* 48 (3) (2007) 471.
- [5] B.W. Jakoby, Y. Bercier, M. Conti, M. Casey, T. Gremillion, C. Hayden, B. Bendriem, D.W. Townsend, Performance investigation of a time-of-flight PET/CT scanner, in: IEEE Nuclear Science Symposium Conference Record, 2008, pp. 3738–3743.
- [6] K. Wienhard, M. Schmand, M. Casey, K. Baker, J. Bao, L. Eriksson, W. Jones, C. Knoess, M. Lenox, M. Lercher, P. Luk, C. Michel, J. Reed, N. Richerzhagen, J. Treffert, S. Vollmar, J. Young, W. Heiss, R. Nutt, *IEEE Trans. Nucl. Sci.* NS-49 (1) (2002) 104.
- [7] J.S. Kim, J.S. Lee, K.C. Im, S.J. Kim, S.-Y. Kim, D.S. Lee, D.H. Moon, *J. Nucl. Med.* 48 (9) (2007) 1527.
- [8] Q. Bao, D. Newport, M. Chen, D.B. Stout, A.F. Chatzioannou, *J. Nucl. Med.* 50 (3) (2009) 401.
- [9] Y.C. Tai, H. Wu, D. Pal, J. O'Sullivan, Virtual-Pinhole PET, *J. Nucl. Med.* 49 (3) (2008) 471.
- [10] Y.-C. Tai, L.-J. Meng, H. Krawczynski, Y. Yin, S. Komarov, H. Wu, J.W. Tan, A. Li, Q. Garson III, J. Martin, Initial study of a sub-500-micron resolution PET insert device based on finely-pixelated CZT detector, Presented at the 2009 IEEE NSS/MIC, Orlando, Florida, 2009.
- [11] S.St. James, J. Zhou, J. Qi, S.R. Cherry, ZIP1: a single detector insert to locally improve the sensitivity and spatial resolution of small animal PET, Presented at the 2009 IEEE NSS/MIC, Orlando, Florida, 2009.
- [12] J. Zhou, J. Qi, Adaptive imaging for lesion detection using a zoom-in PET system, medical imaging, *IEEE Transactions on Medical Imaging*, pp. 99, 1, doi:10.1109/TMI.2010.2064173.
- [13] Gamma Medica-Ideas, Inc. (Norway), ><http://www.gm-ideas.com>>, Martin Linges vei 25, Snarøya, POB 1, N-1330 Fornebu, Norway, Tel: +47-6782-7171.
- [14] A. Studen, D. Burdette, E. Chesi, V. Cindro, N. Clinthorne, E. Cochran, B. Grošičar, K. Honscheid, H. Kagan, C. Lacasta, G. Llosá, V. Linhart, M. Mikuž, V. Stankova, Z. Weilhammer, D. Žontar, Performance of the MADEIRA PET probe prototype, in: IEEE Nuclear Science Symposium Conference Record, 2009, pp. 3111–3115.
- [15] S. Agostinelli, et al., *Nucl. Instr. and Meth. A* 506 (2003) 250.
- [16] A. Studen, D. Burdette, E. Chesi, V. Cindro, N.H. Clinthorne, E. Cochran, B. Grošičar, H. Kagan, C. Lacasta, V. Linhart, M. Mikuž, V. Stankova, P. Weilhammer, D. Žontar, *Radiat. Prot. Dosim.* 139 (2010) 199.

TOPEM: a Multimodality Probe (PET TOF, MRI, and MRS) for Diagnosis and Follow Up of Prostate Cancer

F. Garibaldi, R. De Leo, A. Ranieri, F. Loddo, M. Floresta, C. Tamma, A. Gabrielli, F. Giorgi, F. Cusanno, P. Musico, R. Perrino, P. Finocchiaro, L. Cosentino, A. Pappalardo, F. Meddi, B. Maraviglia, F. Giove, T. Gili, S. Capuani, M. Turisini, N. Clinthorne, S. Huh, S. Majewski, M. Lucentini, M. Gricia, F. Giuliani, and E. Monno

Abstract—Multimodality imaging plays a significant role on specific diagnosis of prostate cancer. An endorectal PET-TOF MRI probe, designed here, allows for improved SNR and NECR with respect to standard imagers, providing better functional diagnosis of prostate diseases.

I. INTRODUCTION

PROSTATE cancer (PC) is the most common disease and a leading cause of cancer death. Precise disease characterization is needed about cancer location, size, and extent and aggressiveness [1]. The current standard for diagnosing PC is transrectal biopsy; however, it is far from perfect. Multimodality imaging can play a significant role by merging anatomical and functional details from simultaneous PET and MRI (and MRS) scans to guide biopsy diagnosis and follow up. Due to sub-optimal prostate imaging geometries, generic scanners prevent separation of the signal from surrounding organs with sensitivity, spatial resolution and contrast inferior to what is achievable with dedicated prostate imagers. Our project is developing an endorectal PET-TOF MRI probe. Exploiting the TOF capability allows an increase in the SNR/NECR and also permits elimination of bladder background [4]. The internal probe is used in coincidence with an external dedicated detector and/or a standard PET ring. Performance is dominated by the endorectal detector with improvements in both spatial resolution and efficiency [2,3]. The electronics must measure coincidences with a precision of 300 ps or less, and be small enough to be connected to the internal detector. For compactness and MRI compatibility, Silicon Photomultipliers

(SiPM) are used. Their time jitter is negligible so the expected time resolution is a direct function of the sqrt of photoelectron number related to the PDE. Extensive ongoing simulation by Geant4 allows study of the scintillator geometry, coupling to the SiPMs and their pixel dimensions.

II. DETECTOR LAYOUT

One of the detectors, to be very close to the source has to be a small endorectal probe. The second detector is a standard PET scanner (detectors close to the body of the patient may be added). Fig. 1 shows the detector layout: a small probe in coincidence with a full ring standard PET possibly integrated by few detectors close to the body of the patient.

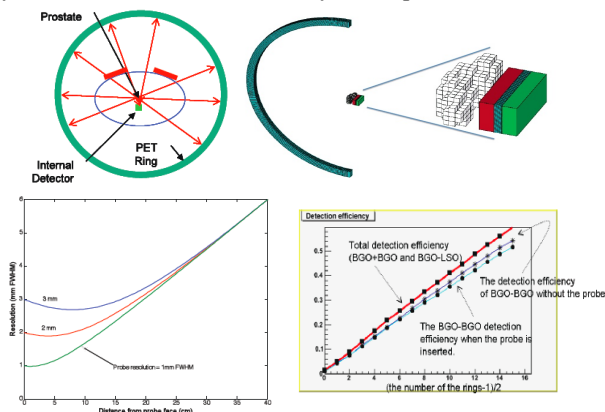


Fig. 1. Top left: Detector layout: a small probe in coincidence with a full ring standard PET possibly integrated by few detectors close to the body of the patient; top right: the layout in the Geant4 code. Bottom left: spatial resolution as function of the distance and of the resolution of the probe; Bottom right: efficiency as function of the dimension of the external PET.

III. SIMULATIONS

A GEANT4 code has been written in order to perform extensive simulations to optimize the detector layout. Preliminary data are available. Fig. 1 (top left) shows the layout of the system and (top right) what has been implemented in the Geant4 code (a Zubal phantom for the prostate, a probe of $25 \times 50 \times 10 \text{ mm}^3$ (LSO coupled to two sheets of SiPM photodetectors and an half ring of standard PET). Preliminary results of simulations, in Fig. 1 (bottom) are also shown the spatial resolution and efficiency obtained with the proposed system: a spatial resolution of 1.5 mm - 2 mm for source distances of 10–20 mm, with improved

Manuscript received December 14, 2010.

F. Garibaldi (franco.garibaldi@iss.infn.it) and F. Meddi are with INFN Sezione di Roma, Roma, Italy.

R. De Leo, A. Ranieri, F. Lodo, M. Floresta, and C. Tamma are with INFN Sezione di Bari, Bari, Italy.

A. Gabrielli and F. Giorgi are with INFN Sezione di Bologna, Bologna, Italy.

P. Musico is with INFN Sezione di Genova, Genoa, Italy.

F. Cusanno is with Technische Universitaet Muenchen, Garching, Germany.

R. Perrino is with INFN Sezione di Lecce, Lecce, Italy.

P. Finocchiaro, L. Cosentino, and A. Pappalardo are with INFN Sezione di Catania, Catania, Italy.

B. Maraviglia, F. Giove, T. Gili, S. Capuani, and M. Turisini are with University La Sapienza, Roma, Italy.

N. Clinthorne, S. Huh are with University of Michigan, Department of Radiology, Ann Arbor MI, USA.

S. Majewski is with West Virginia University, Morgantown WV, USA.

M. Lucentini, M. Gricia, and F. Giuliani are with Istituto Superiore di Sanita', Roma, Italy.

E. Monno is with ENEA, Centro Ricerche Faenza, Faenza, Italy.

efficiency over external PET. Depending on the reconstructed resolution desired, noise can be reduced by up to $\sim 7\times$ over external ring PET alone giving improvements of effective NEC of $\sim 50\times$. Simulation of the energy spectra for LSO and $\text{LaBr}_3(\text{Ce})$ continuous crystals shows the advantage of the $\text{LaBr}_3(\text{Ce})$ in terms of energy resolution (15% vs 17%) (see Fig. 7). The timing also would be better, but the stopping power and spatial resolution wouldn't favorize $\text{LaBr}_3(\text{Ce})$ for the NECR.

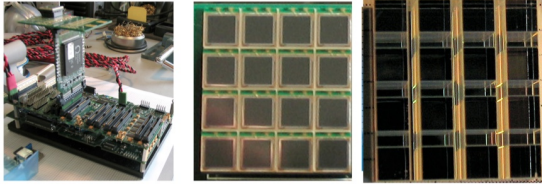


Fig. 2. The minidetector and the electronic setup for the first tests.

IV. A MINIDETECTOR PROTOTYPE

A minidetector prototype has been built (see pictures in Fig. 2) and will be tested in a 3-T MRI soon. Continuous as well as pixellated ($1 \times 1 \text{ mm}^2$ and $3 \times 3 \text{ mm}^2$) LYSO scintillator (with different surface treatments for optimizing both the timing and the Depth Of Interaction (DOI), coupled to SiPM arrays ($3 \times 3 \text{ mm}^2$ anode pixel) will be used. A continuous $\text{LaBr}_3(\text{Ce})$ scintillator sheet and a pixellated LSO doped with Ca, will be also be used for comparison.

A. Characterization of SiPM

Fig. 3 shows basic measurements on SiPM, three typical spectra acquired using the same reverse bias voltage (32.0V), but the detector thermostated at different temperatures: a) 13.5C, b) 24.3C, c) 41.5C. The gain reduction with temperature is due to the variation of breakdown voltage with temperature. The necessity of good timing resolution requires low and stable temperature to lower the noise and triggering on few photoelectrons. For this reason a cooling system (under design, see Fig. 3 b), with feedback on SiPM power supply will be needed.

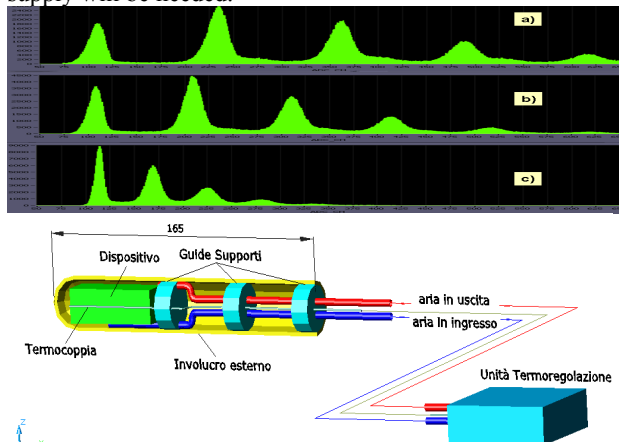


Fig. 3. Top: temperature dependence of gain for SiPM. Bottom: preliminary layout of the system with air cooling system.

B. Discrete Electronic System and Timing Resolution

A discrete electronics system with VME modules and dedicated preamplifiers has been used for preliminary timing

resolution measurements until the dedicated electronics system, namely the challenging ASIC is available. Timing resolution of $< 100 \text{ ps}$ (only the electronics) has been obtained with the discrete electronic system [8]. Moreover preliminary measurements with finger scintillators (LYSO $3 \times 3 \times 5 \text{ mm}^3$) showed that the design timing resolution is obtainable (see Fig. 4). The LYSO finger scintillator were coupled (1 to 1 to optimize the light collection) to Hamamatsu $3 \times 3 \text{ mm}^2$ pixel SiPM. Dedicated preamplifiers were used. A timing resolution as good as 350 ps was obtained. One should note that $25 \mu\text{m}$ microcells SiPM was used. Due to the higher PDE obtainable, this projects out a timing resolution of $\sim 250 \text{ ps}$ once the SiPM with $50 \mu\text{m}$ microcells will be used. A dedicated compact electronic system using off-the-shelf components is under design.

We focused on two main components:

- a very fast preamplifier-discriminator with low input impedance and Time Over Threshold (TOT) capability;
- a Time to Digital Converter (TDC) with dual edge measurement capability and resolution $\leq 100 \text{ ps}$.

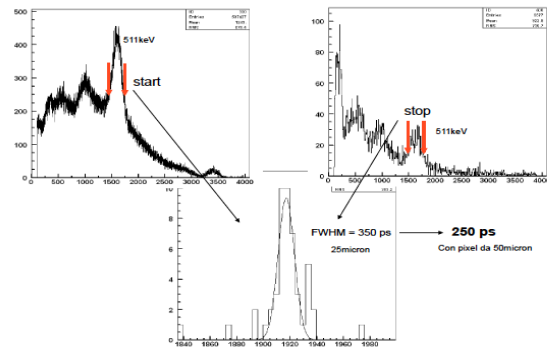


Fig. 4. Preliminary measurements of timing resolution.

We found components with good specifications yet designed and produced for CERN-LHC experiments.

For the preamplifier-discriminator the choice is NINO [6]: an 8 channels wide bandwidth fully differential preamplifier-discriminator with 40Ω input impedance.

For the TDC the HPTDC chip [7] is available. It measures the timing of both edges of the input pulses with resolution selectable down to 25 ps .

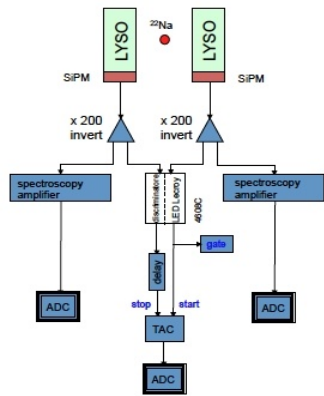


Fig. 5. The setup used for the timing measurements.

The system will be composed by a stack of three boards:

- the detector board hosts the SiPM array;
- the front-end board hosts the NINO chips (128 channels, 16 NINO);
- the TDC board hosts the dedicated chips (4 HPTDC, 32 channels each)
- the Control Board which implements the coincidence logic, readout control and the link with data acquisition computer.

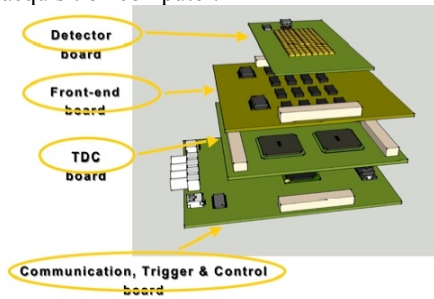
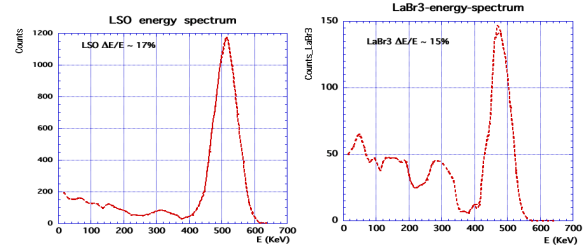
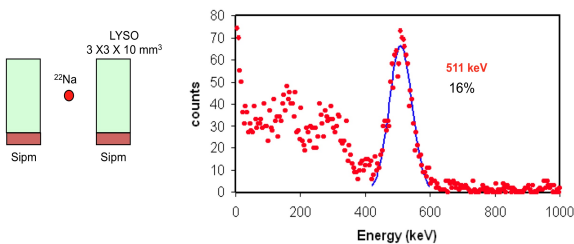


Fig. 6. A sketch of the electronic readout system.

C. Energy Resolution

Fig. 7 shows the energy resolution obtained with two finger LYSO ($3 \times 3 \times 10 \text{ mm}^3$) scintillators coupled to SiPM Hamamatsu ($3 \times 3 \text{ mm}^2$).

Fig. 7. Energy resolution of LYSO ($3 \times 3 \times 10 \text{ mm}^2$) coupled to SiPM Hamamatsu ($3 \times 3 \text{ mm}^2$); b. Simulated energy spectra of LYSO and LaBr3(Ce).

V. CONCLUSIONS

A project for building and testing an endorectal PET TOF probe compatible with MRI (and MRS) started. Preliminary results show that the design performances in terms of timing resolution are obtainable. This will allow significant reduction of noise allowing increasing of SNR/NECR. A powerful compact electronic system is under design. Tests on compatibility of PET with MRI will be performed soon. A full scale prototype of the probe will be designed and tested with phantoms and even with big animal models.

REFERENCES

- [1] G. Kellof et al, "Challenges in Clinical Prostate Cancer: Role of Imaging" *AJR*:192, June 2009, pg. 1455.
- [2] N. Clinthorne et al, Multi-resolution image reconstruction for high resolution small animal PET device. IEEE 2003, Nucl Symp. Conf. Rec. 3: 1997-2001.
- [3] W. W. Moses, Time of flight revisited, IEEE TNS Vol 50, N. 5 October 2003, 1325.
- [4] J. S. Karp et al, Benefit of Time-of-Flight in PET: Experimental and Clinical Results, JNM, February 20, 2008/ nume.107.044834.
- [5] W. W. Moses, Workshop on TOF PET, Baia delle Zagare, September 2009 and personal communication.
- [6] NINO: an ultra-fast and low-power front-end amplifier/discriminator ASIC designed for the multigap resistive plate chamber", NIM A 533 (2004) 183.
- [7] "Design aspects and prototype test of a very precise TDC system implemented for the Multigap RPC of the ALICE-TOF", NIM A 533 (2004) 178
- [8] A. Gabrielli et al, "Preliminary timing measurements on a data acquisition chain for a SiPM-based detector for prostate imaging". Proceedings of 12th Topical Seminar on Innovative Particle and Radiation Detectors (IPRD10) 7 - 10 June 2010 Siena, Italy", To be published in NPB.

The First Generation Prototype of a Surgical PET Imaging Probe System

Sam S. Huh, Eric Cochran, Klaus Honscheid, Harris Kagan, Shane Smith, W. L. Rogers, and Neal H. Clinthorne

Abstract—Our ultimate goal is to provide continuously updated 3-dimensional reconstructed PET images during surgery that are re-projected in real time onto a plane whose orientation is driven by a tracking device. The intra-operative PET imaging probe system can be viewed as a handheld, clinician-guided camera capable of seeing the distribution of the radiotracer. We present the first generation of the PET imaging probe system. The prototype of the first generation of the PET imaging probe system consists of a pixelated NaI(Tl) detector and a partial ring detector. A variant of a one-pass list-mode ordered subsets ML algorithm that was integrated with a row-action ML algorithm was used to reconstruct images. Parallel image reconstruction using a graphics card was used to speed up image reconstruction. The spatial resolution in the transverse direction was close to the NaI(Tl) crystal size. The elongation in the longitudinal direction due to limited angle tomography was not severe.

I. INTRODUCTION

POSITRON Emission Tomography (PET) is an effective diagnostic imaging method for identifying and locating tumors. PET imaging can also identify functional changes due to tumors. Based on the preoperative diagnostic scanning, oncologists make decisions whether or not the tumors are surgically removable. Conventionally if the tumors are surgically removable, surgeons locate and remove the tumors during surgery based on the preoperative images. One of the drawbacks of using only preoperative imaging is that tumor locations could be displaced due to patients' movement. As a result, surgeons have to pay extraordinary attention to locate lesions due to the patients' movement. Even after surgeons locate lesions, the complete removal of tumors is often a difficult task because the margin of tumor may be hard to delineate. One of the reasons to accurately identify the margin is the desire to preserve as much healthy tissue as possible without leaving any residual tumor.

Another important issue during surgery is to discover small tumors that are not detected in preoperative PET imaging. Occult tumors that survive surgery can lead to recurrence. It is well known that early detections of tumors can increase the life span and the quality of patients' life. Reliable detection of tumors that are less than 1 cm in diameter, however, remains a challenge in conventional whole-body PET imaging. Even

though the on-axis intrinsic resolution of current PET devices can be ~5 mm FWHM, this figure is rarely achievable in clinical use because of background activity in nearby tissue, statistical noise, and lack of depth resolution in the detectors. In addition, the relatively large ring diameter of the whole-body PET scanners tends to further reduce the spatial resolution due to annihilation photon acolinearity.

Non-imaging intra-operative probes have demonstrated effective tumor detections during surgical removal of removing lymph nodes. In order to locate small tumors and the residuals of tumor dissection more effectively, Intra-operative *imaging* probes are preferred. Imaging probes can display 2-dimensional images so that surgeons or clinicians spend less time locating lesions.

One scenario is to directly detect beta particles from radioisotopes emitting beta particles. Beta particles with short penetration ranges can be used to achieve high spatial resolution. Although this is attractive from the viewpoint of reducing effects of 511 keV background from elsewhere in the body due to the positron-electron annihilation, beta particles have short positron penetration ranges limiting the method's utility in detecting deep seated, small tumor foci below the surface of exposed tissue.

In order to detect deep-seated tumors, gamma-ray sensitive imaging probes are more suitable than beta particle sensitive imaging probes. However, use of single photon detection typically at 511 keV results in a broad point-spread function due to the long attenuation length in virtually all materials that are used for collimation.

In order to overcome the drawbacks of the two types of imaging probes, we have been investigating a small, high resolution PET imaging probe that operates in coincidence with a segment of a conventional PET scanner. The high spatial resolution intra-operative imaging probes can help surgeons determine locations and extent of primary tumors during surgery and identify multifocal disease. This PET imaging probe system is based on previous studies on high resolution imaging systems [1], [2].

In this study, we present a prototype of the PET imaging probe system as part of a preliminary study of an intra-operative positron emission tomography (PET) imaging probe system that provides reconstructed images in real time. The proposed PET imaging probe system consists of a low resolution partial ring detector and a high resolution imaging probe that is equipped with a position tracker. The high resolution imaging probe and the proximity of the imaging probe to target lesions contribute to the localization of small tumors. Our ultimate goal is to provide continuously updated 3-dimensional reconstructed images that are re-projected in

Manuscript received November 13, 2010.

Sam S. Huh is with the Biomedical Engineering Department, University of Michigan, Ann Arbor, MI 48109 USA (telephone: 734-764-7177, e-mail: huhss@umich.edu).

Eric Cochran, Shane Smith, Klaus Honscheid, and Harris Kagan are with the Department of Physics, Ohio State University, Columbus, OH 43210 USA. (telephone: 614-292-7331, e-mail: cochran.193@osu.edu).

Neal H. Clinthorne is with the Department of Radiology, University of Michigan, Ann Arbor, MI 48109 USA (e-mail: nclintho@umich.edu).

W. L. Rogers is with the Biomedical Engineering Department, University of Michigan, Ann Arbor, MI 48109 (w.l.rogers@umich.edu).

real time onto a plane whose orientation is driven by a tracking device.

The prototype of the PET imaging probe system consists of a pixelated NaI(Tl) detector and a partial ring detector. The partial ring detector comprises 4 BGO block detectors. A variant of a one-pass list-mode OS ML algorithm that was integrated with a row-action ML algorithm was used to reconstruct images [3], [4]. Parallel image reconstruction was used to speed up image reconstruction.

II. EXPERIMENTAL SET-UP

A pixelated NaI(Tl) detector was built to be used as the high resolution imaging probe. An array of pixelated NaI(Tl) crystals was coupled to a 2 in.-by-2 in. position sensitive PMT (Hamamatsu® H8500). The PSPMT has 64 anode outputs. The 64-anode outputs of the PSPMT were routed to a charge division circuit (CDC) that followed by a frontend readout circuit.

A partial ring detector comprises 4 BGO block detectors from a CTI® 931 PET scanner. 4 BGO block detectors were placed side by side to form a partial ring detector.

The coincidence pulses were controlled using a VME FPGA (C.A.E.N.® v1495) via a VME interface system. A custom data acquisition system that is based on Gtkmm [5] and SigCX [6] was used for on-line data acquisition/analysis.

A. Pixelated NaI(Tl) Detector

Fig. 1 shows a position sensitive PMT that has an 8-by-8 array of anodes. Fig. 2 shows a charge division circuit that was coupled to the PSPMT in order to convert 64 anode signals to 4 position output signals. The schematic of the charge division circuit is shown in Fig. 3.



Figure 1. A position sensitive PMT. This picture is from a manual of Hamamatsu® H8500.

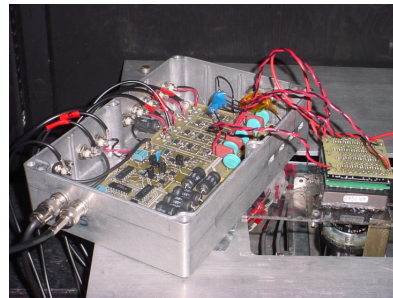


Figure 2. The charge division circuit coupled to the PSPMT.

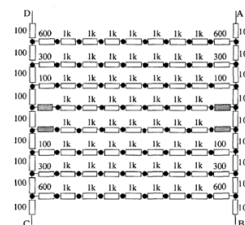


Figure 3. A typical charge division circuit (CDC) [7].

The module of the PSPMT-CDC was coupled to an array of pixelated NaI(Tl) crystals as shown in Fig. 4. Each NaI(Tl) measures $2 \times 2 \times 10 \text{ mm}^3$. The light-tight container is shown in Fig. 5. The trigger pulse and a shaped channel signal are shown in Fig. 6.

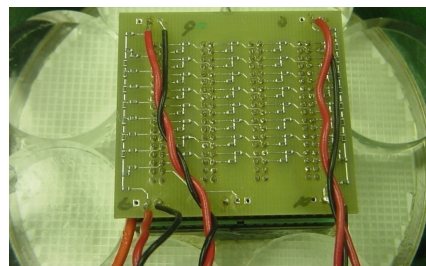


Figure 4. An array of NaI(Tl) crystals and the module of the PSPMT-CDC. Each NaI(Tl) measures $2 \times 2 \times 10 \text{ mm}^3$.

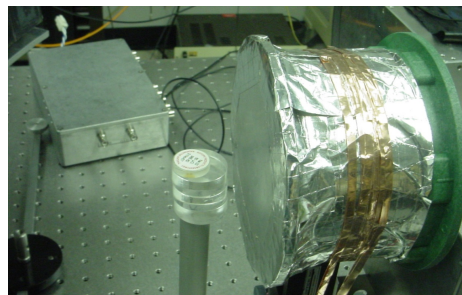


Figure 5. The light-tight container of the NaI(Tl) crystal array.

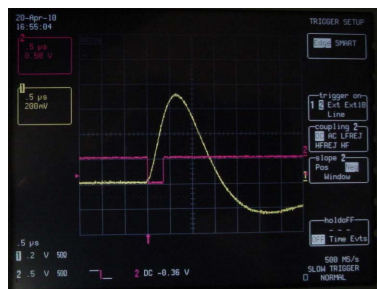


Figure 6. A trigger pulse and a shaped channel signal.

B. BGO Block Detectors

Each BGO block detector has 4 PMTs that are coupled to BGO as shown in Fig. 7. Each BGO crystal measures $5.25 \times 12.5 \times 30 \text{ mm}^3$. The gain of each PMT was adjusted using a coincidence set-up. The set-up is shown in Fig. 8. A PMT coupled to a single LSO crystal was mounted on an optical rail and the BGO block detector was placed on an x-y translation stage. A Na-22 source was positioned in a disk holder in between the LSO detector and the BGO block detector.

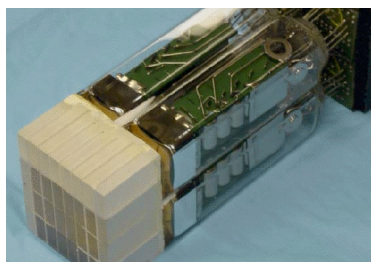


Figure 7. BGO block detector.

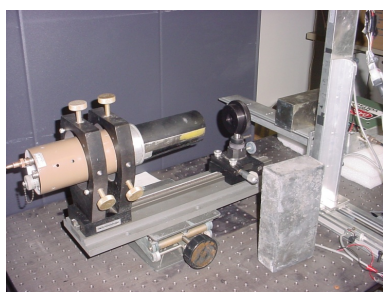


Figure 8. A coincidence gain-adjustment set-up.

Measured coincidence events between the LSO detector and the BGO block detector were processed using a custom data acquisition/analysis program. Fig. 9 shows estimated interaction positions in BGO and the coincidence pulse height spectra at translated positions. The BGO block detector was translated in order to illuminate one BGO crystal near each corner.

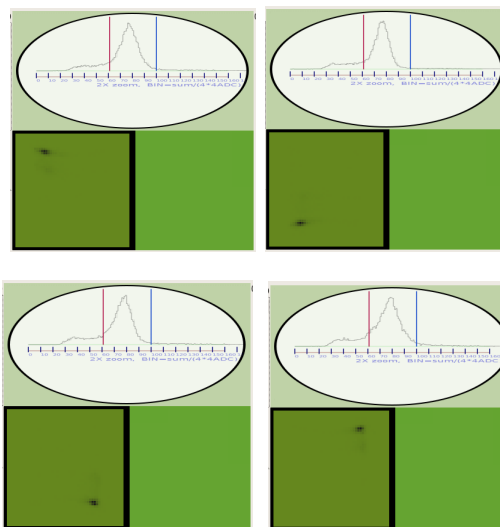


Figure 9. Estimated crystal positions in coincidence measurements.

C. Flood Images

Flood images in BGO detectors and the NaI(Tl) detector were obtained in order to identify the crystals in each detector. A Na-22 ($30 \mu\text{Ci}$ or $60 \mu\text{Ci}$) point source disk was used instead of a flood source.

1) Flood Images in BGO

Fig. 10 shows a pulse height spectrum in BGO from a Na-22 source. The pulse height spectrum shows the 511 keV peak and the 1.275 MeV peak. The lower square with $50\text{-by-}50$ pixels shows the flood image in BGO. We can see 4 rows of spots. Each row shows 8 crystals. In order to clearly separate the crystals, we drew the flood images using $128\text{-by-}128$ pixels. The higher resolution image is shown in Fig. 11.

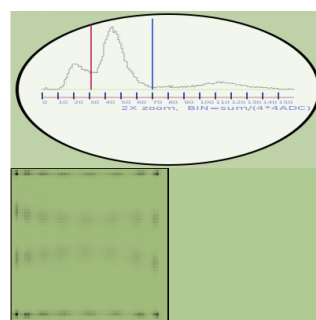


Figure 10. Pulse height spectrum in BGO and a flood image from a Na-22 source.

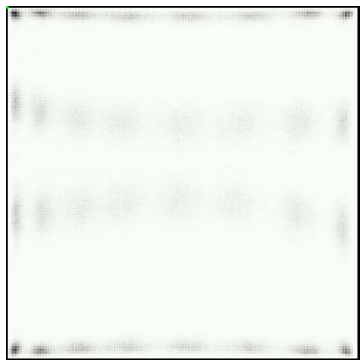


Figure 11. A 128-by-128 flood image in BGO.

2) Flood Images in NaI(Tl)

Fig. 12 shows a Na-22 flood image in NaI(Tl) and the pulse height spectrum. A higher resolution flood image is shown in Fig. 13. The 2mm-pitch NaI(Tl) crystals were clearly identified in Fig. 13. The pulse height spectrum in Fig. 12 does not show the 511 photo peak. This is due mainly to non-uniform conversion efficiency of each crystal, and the size mismatch between the PSPMT and the NaI(Tl) array.

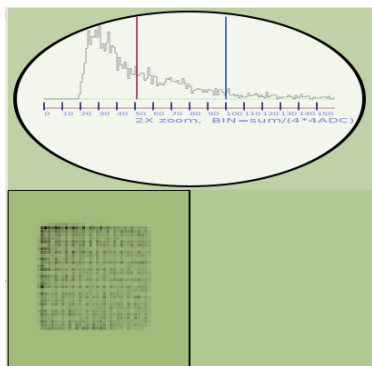


Figure 12. A Na-22 Flood image in NaI(Tl) from Na-22.



Figure 13. A 512-by-512 pixel flood image.

D. Coincidence Images

The coincidence events between one or two BGO crystals and the NaI(Tl) detector were obtained. Fig. 14 shows the Na-

22 coincidence image in NaI(Tl). The pulse height spectrum clearly shows the 511keV photo-peak. The coincidence image shows a few NaI(Tl) crystals.

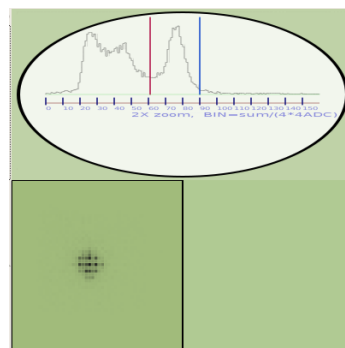


Figure 14. The Na-22 coincidence NaI(Tl) image in coincidence with one or two BGO crystals.

In order to illuminate a single NaI(Tl) crystal, the Na-22 source disk was propped against the front surface of the NaI(Tl) detector as shown in Fig. 15. The coincidence image in Fig. 16 shows a single illuminated NaI(Tl) crystal.

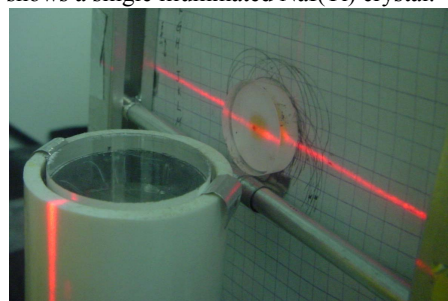


Figure 15. The Na-22 source disk was propped against the front surface of the NaI(Tl) detector.

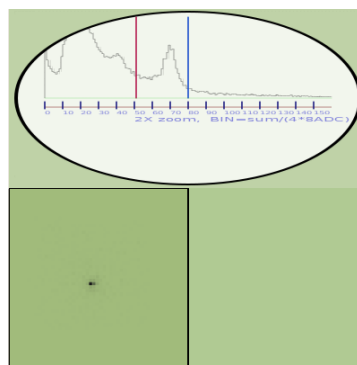


Figure 16. The Na-22 coincidence NaI(Tl) image that shows a single NaI(Tl) crystal.

III. PIXEL IDENTIFICATION

Mapping of estimated crystal positions to true crystal positions is required because the estimate crystal positions are distorted as shown in Fig. 17. Quadrilaterals that surround estimated crystal centers were drawn to show the boundaries

between crystals. The 4 vertexes of each quadrilateral were used to test whether a measured coincidence event fell into the given quadrilateral.

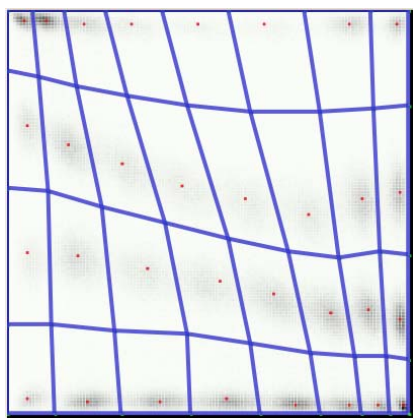


Figure 17. Identifying BGO crystals.

The same crystal identification method was used for the NaI(Tl) detector. Fig. 18 shows a Na-22 flood image in NaI(Tl). The middle points of sets of 4 neighbor crystal centers were picked out to draw the quadrilaterals as shown in Fig. 19.

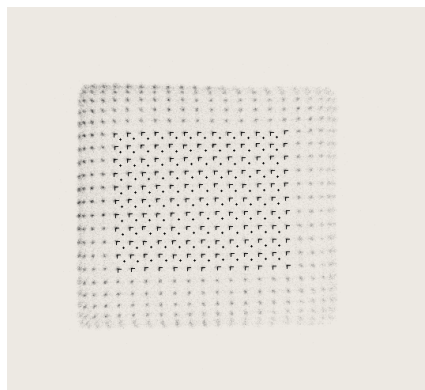


Figure 18. A Na-22 flood image in NaI(Tl) with estimated crystal centers.

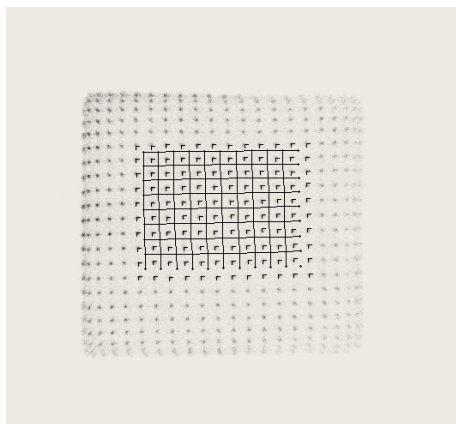


Figure 19. Quadrilaterals that surround the estimated crystal centers.

IV. IMAGE RECONSTRUCTION

Coincidence events between the pixelated NaI(Tl) detector and a partial ring detector were collected in order to reconstruct 3-dimensional images. In order to speed up image reconstruction, we used a graphics processing unit (nVidia® Geforce 9800GTX+) and CUDA. Parallel image reconstruction can be implemented using graphics processing units (GPUs).

A. Coincidence Data Set-up

Fig. 20 shows the prototype of the PET imaging probe system. To the left is the BGO block detectors and to the right is the NaI(Tl) detector. The rotational pivot next to the NaI(Tl) detector is also a cylindrical source stage.



Figure 20. The prototype of the PET imaging probe system.

Fig. 21 illustrates the top view of the experimental set-up. Each BGO detector has 8 crystals. Each crystal measures 5.25mm in width. The NaI(Tl) crystals has effective 11 crystals. Each NaI(Tl) crystal measures 2mm in width.

Fig. 22 illustrates the side view of the experimental set-up. Each BGO detector shows 4 rows. The height of each crystal is 12.5mm. The right hand side shows the effective 9 NaI(Tl) rows. The height of each NaI(Tl) crystal is 2mm.

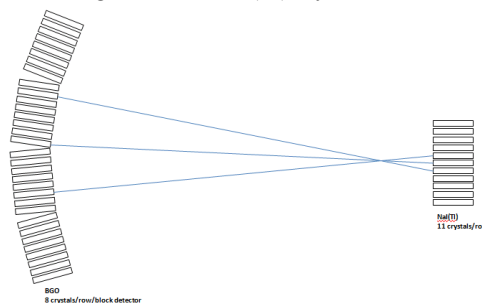


Figure 21. Illustration of the top view of the experimental set-up.

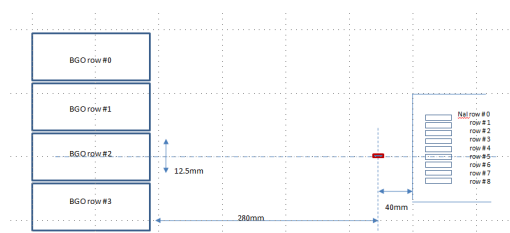


Figure 22. Illustration of the side view of the experimental set-up.

The NaI(Tl) detector was rotated around the cylindrical pivot. Fig. 23 illustrates the rotational movement of the NaI(Tl) detector. It covers about 26° in total. Fig. 24 shows the rotation in the counter-clockwise direction. The clockwise rotation is shown in Fig. 25.

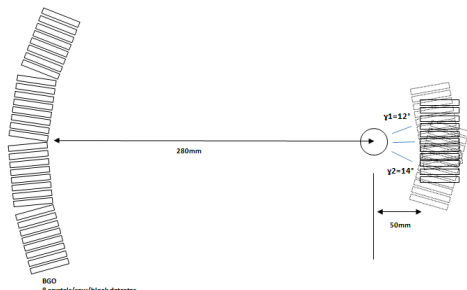


Figure 23. Illustration of the rotational movement of the NaI(Tl) around the rotational pivot.



Figure 24. The rotation of the NaI(Tl) detector in the counter-clockwise direction.



Figure 25. The rotation of the NaI(Tl) detector in the clockwise direction.

A Na-22 double source ($30\mu\text{Ci/point}$) disk was used for data acquisition for image reconstruction as shown in Fig. 26. The center-to-center distance of the two point sources is 1.5mm. The two point sources were aligned parallel to the front surface of the NaI(Tl) detector.

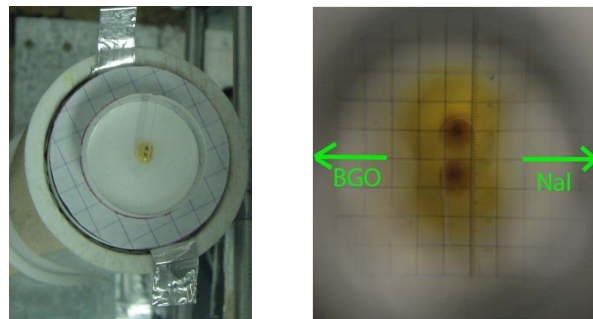


Figure 26. The Na-22 double source disk.

B. Coincidence with one row of BGO crystals

The BGO detector has 4 rows of BGO crystals as shown in Fig. 22. Only one row was enabled for a test run as shown in Fig. 27. The user interface was used to either enable or disable the crystals for data collection. Fig. 28 shows the coincidence image in NaI(Tl). One or two rows of NaI(Tl) crystals were illuminated.

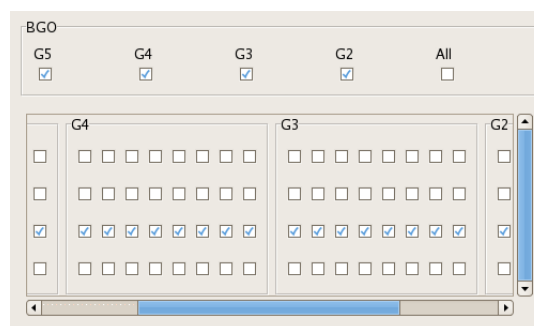


Figure 27. The user interface for BGO crystal selections.

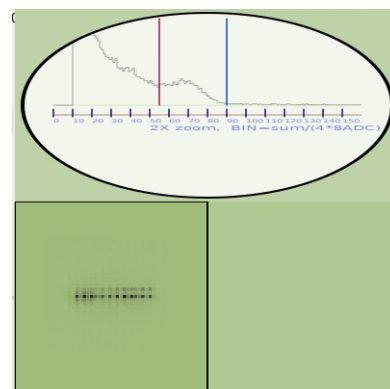


Figure 28. Na-22 coincidence image in NaI(Tl) in coincidence with one row of BGO crystals.

C. Coincidence with 3 Rows of BGO Crystals

Three rows of BGO crystals were enabled for data acquisition as shown in Fig. 29. The coincidence image in NaI

is also shown in the picture. About 5 or 6 rows of NaI(Tl) crystals were illuminated. Only 5 rows of NaI(Tl) crystals were enabled for coincidence data collection.

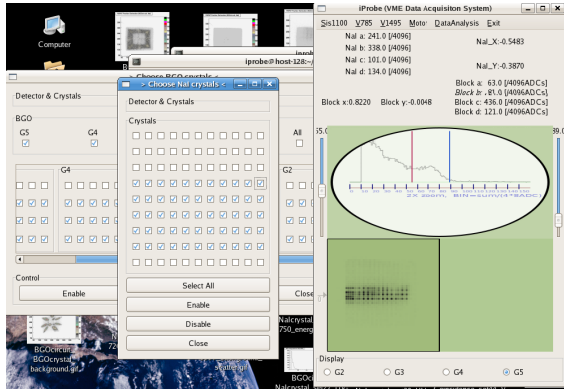


Figure 29. Three rows of BGO crystals.

D. Image Reconstruction Algorithm

We used a variant of a one-pass list-mode OS ML algorithm that was integrated with a row-action ML algorithm. A Gaussian back-projection kernel was also used in the proposed image reconstruction algorithm [8]. The update equation is shown below.

$$x_j^{(s)} = x_j^{(s-1)}(1 - \lambda_s Q_j^{(s)}) + \lambda_s x_j^{(s-1)} \cdot \left(\sum_{i \in s} \frac{G_n(d_j, \sigma)}{\sum_{i=1}^M G_n(d_{ij}, \sigma)} x_i^{(s-1)} \right) \quad (1)$$

Where s is the subset identification number and λ_s is a relaxation factor. Q_j is the sensitivity factor and $G_n(d_j, \sigma)$ is a Gaussian back-projection kernel. σ was taken as the crystal width/2.35.

Each subset contains 16 lines-of-response (LORs). 50 subsets per angle were collected. In simulation studies, we used similar number of LORs and subsets [8], [9].

E. Parallel Image Reconstruction

An nVidia® Geforce 9800GTX+ graphics processing unit and CUDA were used for parallel image reconstruction. It has 128 streaming processors (SPs). Fig. 30 shows the graphics card in a DELL® Optiplex GX280 computer with Fedora 11 and the version 4.3 of gcc.



Figure 30. nVidia 9800GTX+ that is installed in a computer.

The image space was set to a $128 \times 64 \times 64$ array of voxels. Each voxel measures $0.25 \times 0.25 \times 0.25 \text{ mm}^3$.

F. Reconstructed Images

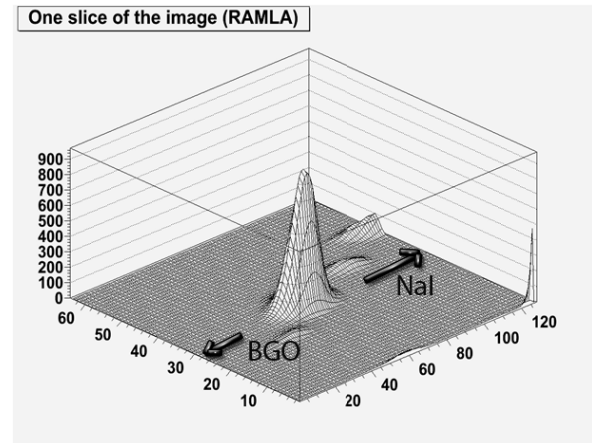


Figure 31. The center slice of a reconstructed image. Each pixel measures $0.25 \text{ mm} \times 0.25 \text{ mm}$.

The coincidence data of the Na-22 double source disk (Fig. 26) from three different angles were collected and the GPU was used to reconstruct images from the coincidence data.

Fig. 31 shows the center slice of the reconstructed image. The FWHM in the transverse direction was about 2mm. As we can expect, the image in the longitudinal direction was elongated. The FWHM in the longitudinal direction was about 4mm.

V. CONCLUSIONS

In this study, a prototype of the surgical PET imaging probe system was built to test the feasibility of the idea of taking coincidences between a high resolution imaging probe and a partial ring detector. A 2mm-sided pixelated NaI(Tl) detector was used for the high resolution imaging probe. BGO block detectors scavenged from a CTI 931 PET scanner were used for the partial ring detector.

A Na-22 double source disk was imaged using the prototype surgical PET imaging probe system. The customized image reconstruction algorithm that included RAMLA, one-pass list-mode OS ML, and a Gaussian kernel was used to obtain reconstructed images. The theoretical spatial resolution of the prototype system was not able to separate the two Na-22 point sources. In parallel with our expectations, the reconstructed images showed a single hump.

The reconstructed images showed that the degree of the effects of limited angle tomography was not severe. The relative lack of artifacts is due mainly to the NaI(Tl) detector's proximity to the target source and the customized image reconstruction algorithm.

REFERENCES

- [1] Lisha Zhang, "Compton gamma-ray imaging probes for prostate and breast," Dissertation at University of Michigan, Ann Arbor, 2004.
- [2] Sang-June Park, et al. , "A prototype of very high-resolution small animal PET scanner using silicon pad detectors," *Nuclear Instruments and Method in Physics Research A* 570, Page(s) 543-555, (2007).
- [3] Reader et al., "One-Pass List-Mode EM algorithm for High-Resolution 3-D PET Image Reconstruction Into Large Arrays," *IEEE Transactions on Nuclear Science*, Vol. 49, No. 3, June 2002.
- [4] Browne et al. "A Row-Action Alternative to the EM Algorithm for Maximizing Likelihood Emission Tomography," *IEEE Transactions on Medical Imaging*, Vol. 15, No. 5, October 1996.
- [5] Available at <http://www.gtkmm.org/en/>.
- [6] Available at <http://libsigcx.sourceforge.net/docs/index.html>.
- [7] Stefan Siegel, Robert W. Silverman, Yiping Shao, Simon R. Cherry, "Simple Charge Division Readouts for Imaging Scintillator Arrays using a Multi-Channel PMT," *IEEE Transactions on Nuclear Science*, Vol. 43, No. 3, June 1996.
- [8] S. S. Huh, W. L. Rogers, N. H. Clinthorne, "On-Line Sliding-Window List-Mode PET Image Reconstruction for a Surgical PET Imaging Probe," M13-4 *IEEE NSS/MIC/RSTD*, October 19-25, 2008, Dresden, Germany.
- [9] Sam S. Huh, Li Han, W. L. Rogers, and N. H. Clinthorne, "Real Time Image Reconstruction Using GPUs for a Surgical PET Imaging Probe System," HPP-13, The workshop on high performance medical imaging (HPMI), *NSS/MIC Conference Record*. October 25-31, 2009, Orlando, Florida, USA.

Report on the MADEIRA PET Probe

Andrej Studen, Enrico Chesi, Vladimir Cindro, Neal H. Clinthorne, Eric Cochran, Borut Grošičar, Klaus Honscheid, S. S. Huh, Harris Kagan, Carlos Lacasta, Gabriela Llosá, Vladimir Linhart, Marko Mikuž, Vera Stankova, Peter Weilhammer and Dejan Žontar

Abstract—PET probes are showing a lot of promise in extending performance of the conventional PET ring. The underlying idea is to supplement basic PET data with information collected in the finely segmented probe placed close to the region of interest. The benefit is two fold: a) data collected near the object are less prone to errors related to scattering and acolinearity and b) the object itself is magnified in the proximity focus. The principle would be beneficial to clinical applications where spatial resolution below the current limit is required in a narrow field of view.

The probe should therefore have excellent spatial resolution, should be compact and robust and should be able to handle large count rates of the clinical environments. Based on those we decided to explore devices with high-resistivity silicon as the sensitive material. They provide high spatial resolution, are compact and robust, and can handle the foreseen rates. We constructed a prototype, based on 1 mm thick silicon wafers, cut into 40 by 26 mm² detectors further segmented into 1 x 1 mm² square pads, effectively providing 1 mm³ sensitive voxels. For a module, two such detectors were placed in a back-to-back arrangement, providing filling factor in excess of 70 %. Stacking multiple modules is foreseen to compensate for low stopping power of silicon. The sensors are read out by 128 channel VATAGP7, GM-Ideas sourced application sensitive integrated circuit. Each module requires 16 chips, placed on 4 custom made PCB boards (hybrids) which are read independently.

The modules were characterized and will be placed in a test PET ring. A simple point sources and phantoms will be imaged to confirm the predicted benefits.

Index Terms—silicon pad detectors, PET insert, medical imaging.

I. INTRODUCTION

THERE is a trend in PET imaging towards improved resolution of the PET scanners. From early 2000s and resolution of 6 mm [1], [2] at the center of the field of view (FOV), the performance of current whole-body devices has improved to 4 mm [3], [4] at the expense of increased crystal count and associated complexity of the associated readout electronics. On the other hand, dedicated devices for brain [5] or preclinical imaging [6], [7] already exhibit resolutions between 1 and 2 mm FWHM, at the expense of significantly reduced FOV.

The PET probe concept [8]–[11] can dynamically merge the approaches outlined above. Figure 1 illustrates the approach:

V. Cindro, B. Grošičar, M. Mikuž, A. Studen and D. Žontar are with the Jožef Stefan Institute, Ljubljana, Slovenia. M. Mikuž is also with University of Ljubljana, Ljubljana, Slovenia.

E. Chesi, E. Cochran, K. Honscheid, H. Kagan and P. Weilhammer are with the Ohio State University, Columbus, OH, USA

N. H. Clinthorne and S. S. Huh are with the University of Michigan, Ann Arbor, MI, USA.

C. Lacasta, G. Llosa, V. Linhart and V. Stankova are with IFIC/CSIC-UVEG, Valencia, Spain.

starting with an external ring, an additional sensitive detector, a probe, is placed within the ring. Most of the annihilation photon pairs will be detected in the external ring (ring-ring events), however some will have one photon hitting the probe and the other photon hitting the ring (probe-ring event). Should the events occur close to the probe, the uncertainty in the line of response will be dominated by the probe resolution and the uncertainty due to the acolinearity will be practically negligible. Figure 2 shows uncertainty in the direction perpendicular to the line of response for three different resolutions of the probe as a function of the distance of annihilation from the probe. A detector with 6 mm FWHM resolution is assumed as the ring detector.

The MADEIRA collaboration aims at improving relation between the image quality and the absorbed dose in imaging with radiopharmaceuticals. Within the collaboration, our group is developing a PET probe prototype based on silicon detectors. Silicon was chosen because of its excellent potential in spatial resolution. The following sections will describe our prototype, the prototype characterization in terms of efficiency, energy, timing and spatial resolution. At the end results from initial tests, demonstrating the excellent resolution of probe-ring events, will be shown.

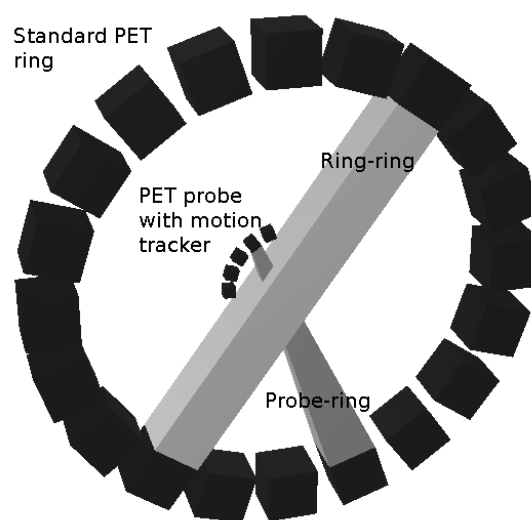


Fig. 1. Schematic drawing of the PET probe principle.

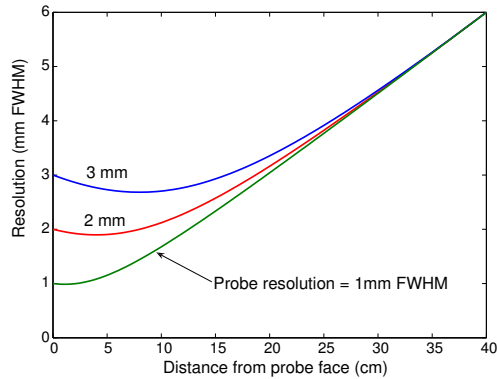


Fig. 2. Functional dependence of uncertainty in direction perpendicular to the line of response to the distance of photon annihilation from the probe face. Curves correspond to three different spatial resolutions of the probe. Resolution of the ring detector (placed at 40 cm distance from the probe) is assumed to be 6 mm FWHM.

II. THE PROTOTYPE

Figure 3 shows a set of two modules of silicon detectors, comprising building blocks of the MADEIRA PET probe prototype. Each module consists of two layers of silicon detectors, each 1 mm thick and segmented into 1040 pads with a size of 1 by 1 mm². The total size of the sensors is 40 by 26 mm². The detectors are placed approximately 0.8 mm apart, giving a stacking fraction of 70%; 2 mm active material over 2.8 mm total thickness. The readout is spaced to 4 independent hybrids/plastic circuit boards with separate readout to minimize electronics cross-talk. Each board hosts four application specific integrated circuits (ASIC) by name of VATAGP7, designed and produced by Gamma Medica Ideas [12]. Each ASIC hosts 128 channels and each channel is comprised of a common charge-integrating amplifier, with its output split into a pair of independent shaping circuits, one with a slow and other with a fast shaping time. The fast circuit is coupled to a leading edge comparator for a combined trigger of 128 channels, and the slow circuit is connected to a shift register through a sample and hold circuit. For each event, the address of the hit channel along with the analog value of the hit pixel and a preset number of adjacent channels (typically three) is read. The gantry of the prototype, shown in Figure 4 allows for flexible task-oriented arrangements of the modules, either maximizing coverage or increasing detection efficiency.

III. PROTOTYPE CHARACTERIZATION

- **Efficiency.** The efficiency of the probe in collecting events was estimated using Monte-Carlo simulations and GEANT4 [13] software package. We modelled a human whole-body ring supplemented by a single 1 mm thick slice of silicon detector as the probe. To simulate scattering and activity outside of the FOV, a barrel of water measuring 60 cm in length, with an elliptical cross-section with primary axes of 10 and 20 cm was placed axially in the ring. The probe was placed 2 cm away from

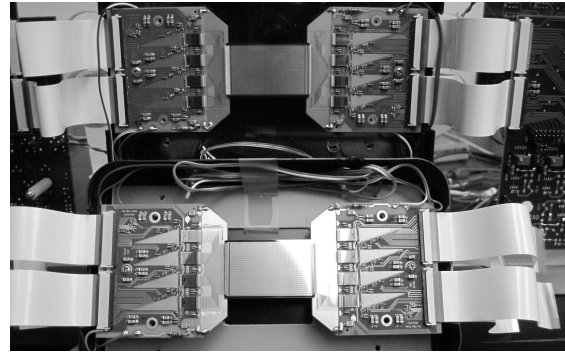


Fig. 3. Photograph of a set of two modules for MADEIRA PET probe prototype.

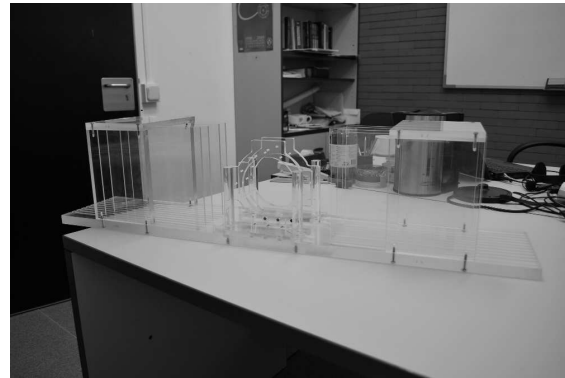


Fig. 4. Photograph of the gantry for module placement.

the barrel. Annihilations were simulated homogeneously throughout the barrel. Counting interactions in the ring and the probe, there were 1000 ring-ring interactions for each probe-ring interaction. However, the distribution of probe-ring events within the object that were detected is biased towards regions close to the probe. Within that area, relative efficiencies of 100 ring-ring events for 1 probe-ring event were estimated. Adding multiple layers of silicon detectors, relative efficiencies close to 10 % are reasonably achievable, with negligible contributions of double interactions [14].

- **Energy resolution** The energy resolution of detectors in PET is normally used for classification of events. The aim is to separate direct photons from those scattered in the body prior to detection. Most of the detectors in PET have a high probability of photoelectric effect and a tight window is drawn around the photoabsorption energy peak to eliminate scattered events. In silicon detectors, the dominant interaction is Compton scattering with continuous energy spectra of electrons excited by photon interaction and windowing on the photo-peak has no practical value. However, Figure 5 shows simulated energy spectrum of events detected in silicon detector classified by whether they scattered prior to interaction.

By applying an optimized cut on the interaction energy, a powerful reduction of scattered events can be performed. The energy resolution of the probe modules at 2 keV is sufficient to allow strenuous optimization of such a cut.

- Timing resolution** The timing resolution is required to separate true coincidences from randomly coupled interactions of consecutive positron emissions. Once one of the photon pairs interacts in a silicon, a timing window is opened to match it to an interaction in the ring. For a true event, the second photon should be detected in the ring, the probability of which was estimated from simulation to be one in five. On top of that, applying timing windows shorter than timing uncertainties of the sensor pair will result in another efficiency cut. From out previous work [8] the efficiencies were 51, 74 and 86 % for 1 mm sensor and timing windows of 10, 20 and 30 ns, respectively. The probability of a random match can be expressed as $P(\text{random}) = 1 - \exp(-R \cdot t_w)$, where R is the rate of the single interactions in the ring and t_w is the timing window. From simulations R is estimated as 3 interactions per 10 positron emissions so it scales with total activity in the object. Figure 6 shows comparison of probabilities for both type of events as a function of time window, showing that our probe (inverted triangles) can only be used in moderate radioactive environment. If higher activities are to be considered, timing can be hypothetically improved by reducing the sensor thickness, as indicated by simulated performance of a 0.5 mm probe indicated by open circles in the Figure.

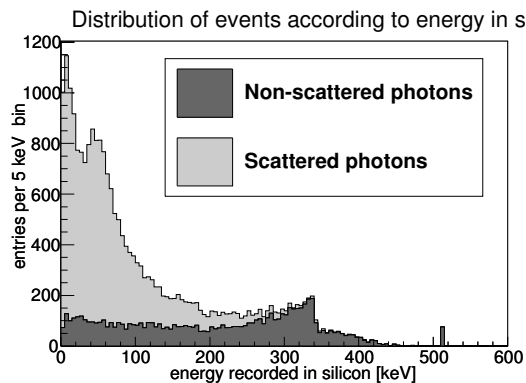


Fig. 5. The energy spectrum of simulated events in silicon. The histogram for the scattered events (dark grey) is superimposed on the histogram for the non-scattered events (light grey).

IV. INITIAL RESULTS

The spatial resolution of the sensors and resolution of the probe-ring events were the first parameters to be evaluated in our bench-top setup set at the University of Michigan. The photograph in Figure 7 shows the arrangement. There are two banks of block BGO detectors, each covering an angle of 67.5 degrees. Each block has a set of 32 crystals measuring 6 by 13 by 30 mm³, arranged in a 8 by 4 matrix, with axial coarse

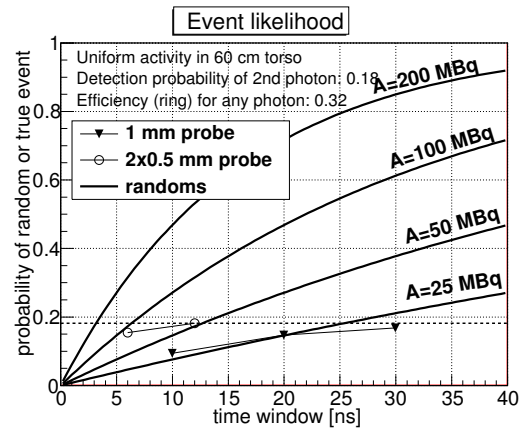


Fig. 6. Probability of true or random coincidence as a function of the duration of the coincidence window t_w . Probability of a random coincidence is indicated with thick solid lines for indicated activities in the simulated water barrel for whole-body PET scanner. The inverted triangle graph shows expected performance of a 1 mm thick silicon detector used as a probe, and open circles show hypothetical performance of a 0.5 mm thick silicon sensor.

segmentation, viewed by 4 photo-multiplier tubes (PMT). The gains of PMTs were aligned and the blocks were calibrated using flood illumination. Further in there is a pair of silicon detectors placed on each side of the object. For the initial test, a previous generation of probe modules was used, with equal electronics, ASIC and detector thickness, but detectors with double the pad area (1.4 by 1.4 mm²). The sources are placed on a rotating table, and collimated to a thin slice that contains both silicon detectors in the edge-on arrangement.

A setup with two probe detectors allows one to collect an additional type of event, a probe-probe event. The spatial resolution of such an event is completely determined by the resolution of the probe sensors. Figure 8 shows a filtered-back-projection (FBP) of probe-probe events for a simple phantom consisting of a single ²²Na point source shifted by 2 mm for three consecutive runs. The reconstruction allows to easily separate the events, indicating a resolution close to the pad size of 1.4 mm. Figure 9 shows FBP for probe-ring events. Still, the point sources are clearly separated, confirming the predictions indicated in Figure 2.

V. SUMMARY

The PET probe concept allows one to dynamically combine high spatial resolution of events in a narrow FOV close to the probe with large FOV of the external ring. The spatial resolution of the probe-ring events is predominantly determined by the spatial resolution of the probe sensor. Our group has built a demonstrator based on silicon detectors with 1 mm segmentation. Relative efficiency of probe-ring versus ring-ring events is 1 % per 1 mm thick layer of silicon detectors as a probe. The energy resolution is sufficient to allow energy cuts to separate scattered events from direct hits. The timing resolution allows the probe to be operated in a reasonable radioactive environment. We built a test setup with a partial ring of BGO block detectors combined with a pair of

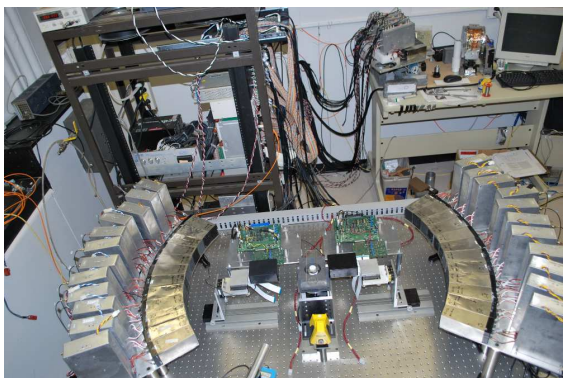


Fig. 7. Photograph of the setup at University of Michigan.

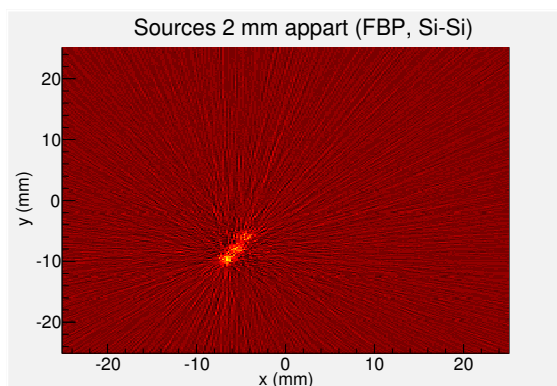


Fig. 8. Filtered back-projection (FBP) of probe-probe events.

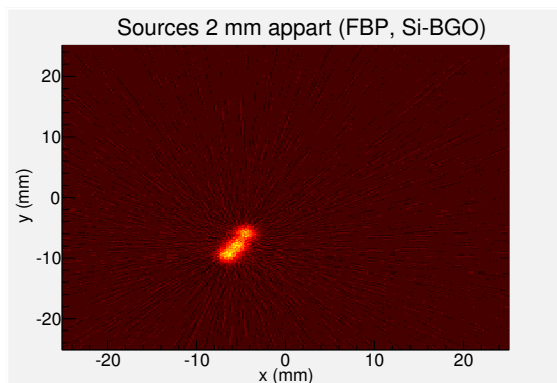


Fig. 9. Filtered back-projection of probe-ring events.

previous generation of silicon detectors functioning as a PET probe. The data reconstructed from probe-probe interactions confirmed excellent spatial resolution of the probe detectors. The resolution of the probe-ring events was demonstrated by reconstructing events where one photon interacted in a silicon detector and the other in the BGO block, giving resolution below 2 mm FWHM, as expected by the calculation. These

results indicate the validity of the approach, so our next effort will be directed towards demonstrating performance for more complex phantoms and sophisticated reconstruction algorithms.

ACKNOWLEDGMENT

The work was carried out within the Collaborative Project "MADEIRA" (www.madeira-project.eu), cofunded by the European Commission through EURATOM Seventh Framework Programme (Grant Agreement FP7-212100). Authors would also like to acknowledge support from the NIH grant NIH R01 EB430.

REFERENCES

- [1] O. Mawlawi, D. A. Podoloff, S. Kohlmyer, J. J. Williams, C. W. Stearns, R. F. Culp, and H. Macapinlac, "Performance Characteristics of a Newly Developed PET/CT Scanner Using NEMA Standards in 2D and 3D Modes," *J Nucl Med*, vol. 45, no. 10, pp. 1734–1742, 2004.
- [2] Y. E. Erdi, S. A. Nehmeh, T. Mulnix, J. L. Humm, and C. C. Watson, "PET Performance Measurements for an LSO-Based Combined PET/CT Scanner Using the National Electrical Manufacturers Association NU 2-2001 Standard," *J Nucl Med*, vol. 45, no. 5, pp. 813–821, 2004.
- [3] S. Surti, A. Kuhn, M. E. Werner, A. E. Perkins, J. Kolthammer, and J. S. Karp, "Performance of Philips Gemini TF PET/CT Scanner with Special Consideration for Its Time-of-Flight Imaging Capabilities," *J Nucl Med*, vol. 48, no. 3, pp. 471–480, 2007.
- [4] B. W. Jakoby, Y. Bercier, M. Conti, M. Casey, T. Gremillion, C. Hayden, B. Bendriem, and D. W. Townsend, "Performance Investigation of a Time-of-Flight PET/CT Scanner," in *IEEE Nucl Sci Conf R*, October 2008, pp. 3738–3743.
- [5] K. Wienhard, M. Schmand, M. Casey, K. Baker, J. Bao, L. Eriksson, W. Jones, C. Knoess, M. Lenox, M. Lercher, P. Luk, C. Michel, J. Reed, N. Richerzhagen, J. Treffert, S. Vollmar, J. Young, W. Heiss, and R. Nutt, "The ECAT HRRT: Performance and First Clinical Application of the New High Resolution Research Tomograph," *IEEE T Nucl Sci*, vol. 49, no. 1, pp. 104–110, Feb 2002.
- [6] Q. Bao, D. Newport, M. Chen, D. B. Stout, and A. F. Chatzioannou, "Performance Evaluation of the Inveon Dedicated PET Preclinical Tomograph Based on the NEMA NU-4 Standards," *J Nucl Med*, vol. 50, no. 3, pp. 401–408, 2009.
- [7] J. S. Kim, J. S. Lee, K. C. Im, S. J. Kim, S.-Y. Kim, D. S. Lee, and D. H. Moon, "Performance Measurement of the microPET Focus 120 Scanner," *J Nucl Med*, vol. 48, no. 9, pp. 1527–1535, 2007.
- [8] A. Studen, D. Burdette, E. Chesi, V. Cindro, N. H. Clinthorne, E. Cochran, B. Grošičar, H. Kagan, C. Lacasta, V. Linhart, M. Mikuž, V. Stankova, P. Weilhammer, and D. Žontar, "Timing Performance of the Silicon PET Insert Probe," *Radiat Prot Dosim*, vol. 139, pp. 199–203, 2010.
- [9] J. Zhou and J. Qi, "Adaptive Imaging for Lesion Detection Using a Zoom-in PET System," *IEEE T Med Imaging*, in press.
- [10] S. St. James, J. Zhou, J. Qi, and S. R. Cherry, "ZIPI: a Single Detector Insert to Locally Improve the Sensitivity and Spatial Resolution of Small Animal PET," presented at the 2009 IEEE NSS/MIC, Orlando, Florida.
- [11] Y.-C. Tai, L.-J. Meng, H. Krawczynski, Y. Yin, S. Komarov, H. Wu, J. W. Tan, A. Li, Q. Garson III, and J. Martin, "Initial Study of a Sub-500-Micron Resolution PET Insert Device Based on Finely-Pixelated CZT Detector," presented at the 2009 IEEE NSS/MIC, Orlando, Florida.
- [12] Gamma Medica-Ideas, Inc. (Norway), <http://www.gm-ideas.com>, Martin Linges vei 25, Snarøya, POB 1, N-1330 Fornebu, Norway, Tel: +47-6782-7171.
- [13] S. Agostinelli *et al.*, "GEANT4: A Simulation Toolkit," *Nucl Instrum Meth A*, vol. 506, pp. 250–303, 2003.
- [14] S.-J. Park, W. L. Rogers, S. Huh, H. Kagan, K. Honscheid, D. Burdette, E. Chesi, C. Lacasta, G. Llosá, M. Mikuž, A. Studen, P. Weilhammer, and N. H. Clinthorne, "Performance evaluation of a very high resolution small animal pet imager using silicon scatter detectors," *Physics in Medicine and Biology*, vol. 52, no. 10, p. 2807, 2007. [Online]. Available: <http://stacks.iop.org/0031-9155/52/i=10/a=012>

Progress in Development of a High-Resolution PET Prostate Imaging Probe

Neal Clinthorne, Stan Majewski, Alexander Stolin, Raymond R Raylman, Sam S. Huh, Jesse Carr, Zhewei Chen, Emma Salomonsson, Aashay Yande, Harris Kagan, Shane Smith, Karol Brzezinski, Andrej Studen

I. INTRODUCTION

As an imaging modality for prostate cancer, PET allows the possibility of “engineering” radiotracers to follow specific metabolic pathways or to indicate the presence of biomarkers associated with disease. Nevertheless, our considerable investment in tracer development cannot be used to full advantage if PET instrumentation is not capable of imaging small prostatic lesions well. Strong attenuation of annihilation radiation emitted from the prostate, intrinsic resolution limits of present scanners, and patient motion during scanning all contribute to modest imaging performance when lesion diameters are 8mm or less.

One way to attack the resolution problem is to use an image reconstruction method that models—and then unfolds—blurring intrinsic to the measurements. While this can work to an extent, it inevitably increases the noise level in reconstructed images with each imaging system having its peculiar tradeoff between resolution and noise. Shown in Figure 1 are resolution-noise tradeoff curves for three PET scanner models having different intrinsic resolutions (4mm, 6mm, and 8mm FWHM). Notice how quickly the noise level increases as one attempts to work beyond the “brick wall” imposed by the intrinsic resolution.

An alternative to resolution recovery methods is to use organ-specific high-resolution probes as add-ons to conventional PET scanners in much the same fashion as application-specific imaging coils are used in MRI. Described by several investigators [1-4], resolution performance of these instruments in regions close to the probe is dominated by the resolution of the probe as illustrated in Figure 2 and as given by the following approximation:

$$R_D \approx 2.35 \sqrt{((1-\alpha)^2 (\sin^2 \theta_1 \sigma_{D1}^2 + \cos^2 \theta_1 \sigma_{C1}^2) + \alpha^2 (\sin^2 \theta_2 \sigma_{D2}^2 + \cos^2 \theta_2 \sigma_{C2}^2))}$$

where α is the fractional distance from the probe detector at which resolution is desired along a line-of-response connecting the probe and conventional PET, σ represents the rms uncertainty of each detector in either circumferential or depth direction, and θ the angle of incidence of the LOR on each detector. From Figure 3 one immediately notes that spatial resolution—even at moderate distances from the probe—is dominated by probe detector performance.

Even though, the fraction of data collected by the probe is relatively small in comparison the total, such high resolution data can have a strong impact on the overall noise-resolution tradeoff when compared to conventional PET. Shown in Figure 4 is the relative noise advantage as a function of desired reconstructed resolution when a fraction (12%) of data having intrinsic

resolutions of 1mm, 2mm, and 3mm FWHM is added to PET data having 4mm FWHM uncertainty. In order to achieve the same noise level, a mean number of events equal to the *square* of the noise advantage must be acquired using conventional PET alone.

II. PROGRESS TOWARD DEVELOPING A PROBE FOR PATIENTS

Work to develop a high resolution prostate imaging probe to augment data from a conventional PET ring is proceeding rapidly along three fronts. First, high-resolution PET detectors having good 3D position resolution have been developed at WVU’s Center for Advanced Imaging using arrays of LYSO crystals coupled to silicon photomultiplier (SiPM) arrays. To date, devices using several readout technologies have been evaluated. Figure 6 shows an early non-DOI incarnation using an array of 1.5mm x 1.5mm x 10mm LYSO scintillators. Second, good progress has been made in developing packaging and tracking details necessary for human use. Figure 5 shows a mechanical model used for stress testing. Finally, high-resolution PET from high/low-resolution hybrid events has been demonstrated on a partial-ring BGO PET system using a high-resolution silicon detector insert. Figure 7 shows the system while Figure 8 shows images reconstructed from the lowest resolution events (BGO-BGO), the highest resolution (Si-Si), and—highly relevant to the prostate probe—the intermediate resolution Si-BGO events. In the next few months, the high-resolution endorectal detectors will be interfaced to this unit to assess advantages of adding the high resolution data to conventional PET.

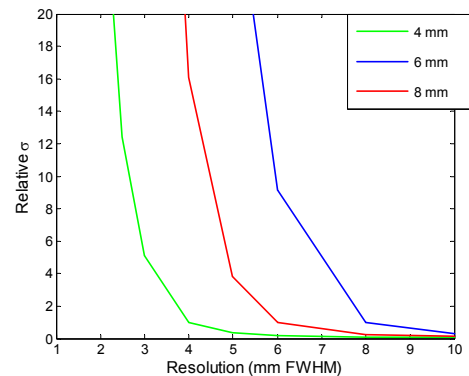


Figure 1. Effects of resolution recovery on noise. Reconstruction noise is plotted against desired reconstructed resolution for scanners having intrinsic resolutions of 4mm, 6mm, and 8mm FWHM..

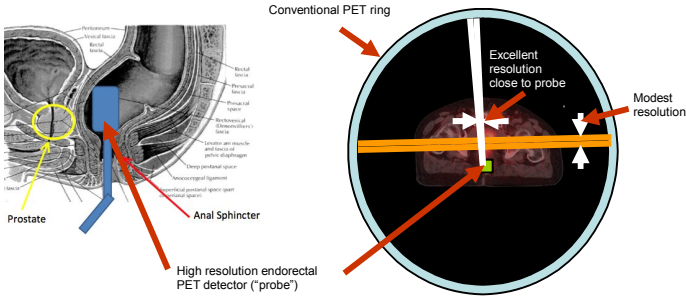


Figure 2. Diagram of endorectal PET prostate probe and its effect on resolution..

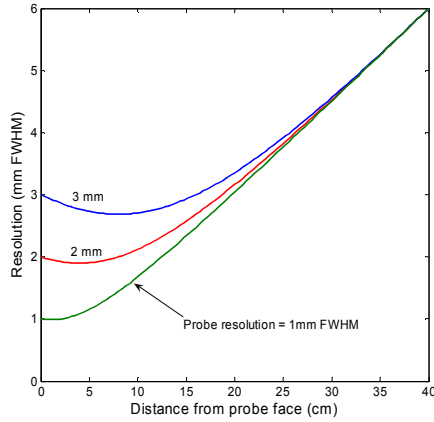


Figure 3. Intrinsic spatial resolution vs. distance from probe for external PET detector having 6mm FWHM resolution.

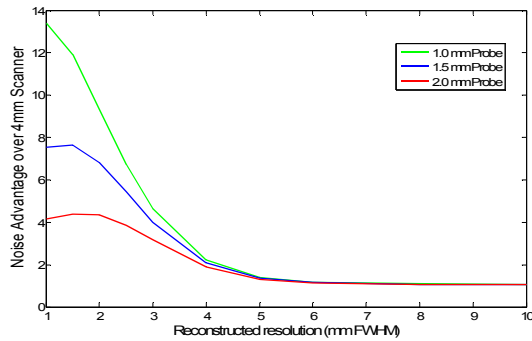


Figure 4. Noise advantage resulting from augmenting conventional PET (4mm FWHM intrinsic resolution) data with 12% additional high resolution data having intrinsic resolutions of 1mm, 1.5mm, and 2mm FWHM..

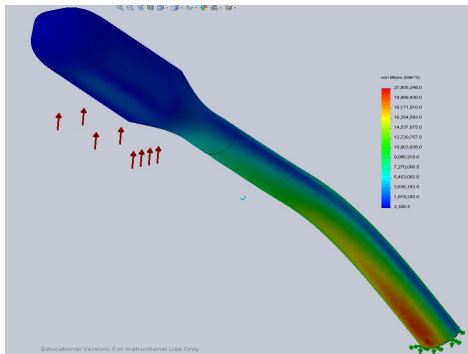


Figure 5. Mechanical model of endorectal probe used for stress analysis. Prototype housings suitable for human use have been constructed using light-tight black delrin.

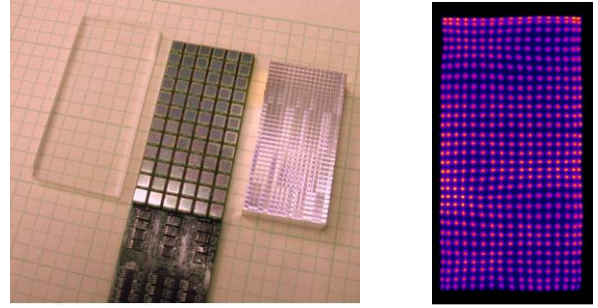


Figure 6. Left: an early non-DOI prototype developed at the Center for Advanced Imaging. Right: crystal identification in a 1.5mm x 1.5mm x 10mm LYSO array. More recent versions support DOI resolution using two-sided readout via SiPM arrays.

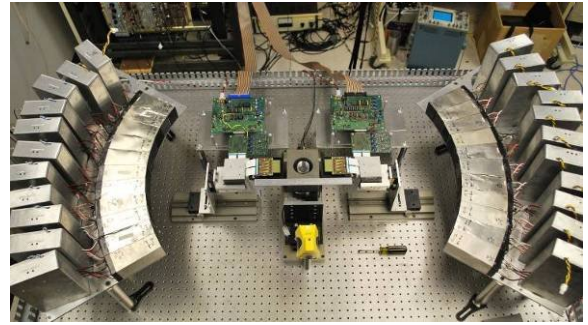


Figure 7. Partial-ring BGO PET system to which prototype prostate probe will be interfaced for initial tests. Configuration shown is a dual-ring BGO/high-resolution silicon (Si) setup for small field-of-view imaging. Silicon detectors will be removed when LYSO/SiPM detector is installed.

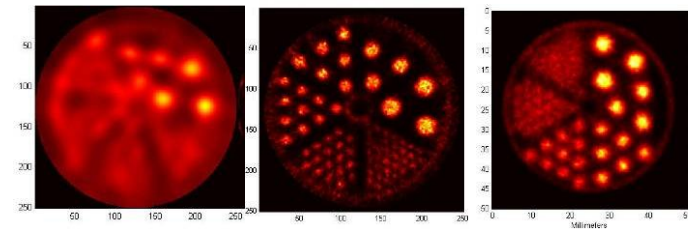


Figure 8. Left: reconstruction of MicroJaszczak resolution phantom data from system above using lowest resolution BGO-BGO events. Center: reconstruction of same phantom using highest resolution (Si-Si) events. Right: reconstruction using hybrid Si-BGO events illustrating probe resolution advantages shown in Figure 3.

III. REFERENCES

- [1] NH Clinthorne, et al. "Very high resolution animal PET," *J Nucl Med Suppl.* 41:20, 2000.
- [2] YC Tai, H Wu, D Pal, JA O'Sullivan, "Virtual pinhole PET," *J Nucl. Med.* 49:471-479, 2008.
- [3] SS Huh, NH Clinthorne, WL Rogers, "Investigation of an internal PET probe for prostate imaging," *Nucl. Ins. Met. Phys. Res A*, 579:339-343, 2007.
- [4] J Zhou, J Qi, "Theoretical analysis and simulation study of a high-resolution zoom-in PET system," *Phys. Med. Biol.* 54:5193, 2009.

Conference Title

A high-resolution PET demonstrator using a silicon “magnifying glass”

Neal Clinthorne^{a*}, Eric Cochran^b, Enrico Chesi^c, Milan Grkovski^d, Borut Grošičar^d, Klaus Honscheid^b, Sam S. Huh^a, Harris Kagan^b, Carlos Lacasta^e, Karol Brzezinski^e, Vladimir Linhart^e, Marko Mikuž^d, D. Shane Smith^b, Vera Stankova^e, Andrej Studen^d, Peter Weilhammer^c, Dejan Žontar^d

^a*Nuclear Medicine and Molecular Imaging, University of Michigan, Ann Arbor, MI 48109-5610 USA*

^b*Department of Physics, Ohio State University, Columbus, OH USA,*

^c*CERN, Geneva, Switzerland*

^d*Jozef Stefan Institute, Ljubljana, Slovenia*

^e*IFIC / CSIC University of Valencia, Valencia, Spain*

Abstract

To assist ongoing investigations of the limits of the tradeoff between spatial resolution and noise in PET imaging, several PET instruments based on silicon-pad detectors have been developed. The latest is a segment of a dual-ring device to demonstrate that excellent reconstructed image resolution can be achieved with a scanner that uses high-resolution detectors placed close to the object of interest or surrounding a small field-of-view in combination with detectors having modest resolution at larger radius. The outer ring of our demonstrator comprises conventional BGO block detectors scavenged from a clinical PET scanner and located at a 500mm radius around a 50mm diameter field-of-view. The inner detector—in contrast to the high-Z scintillator typically used in PET—is based on silicon-pad detectors located at 70mm nominal radius. Each silicon detector has 512 1.4mm x 1.4mm x 1mm detector elements in a 16 x 32 array and is read out using VATA GP7 ASICs (Gamma Medica-Ideas, Northridge, CA). Even though virtually all interactions of 511 keV annihilation photons in silicon are Compton-scatter, both high spatial resolution and reasonable sensitivity appears possible. The system has demonstrated resolution of ~0.7mm FWHM with Na-22 for coincidences having the highest intrinsic resolution (silicon-silicon) and 5–6mm FWHM for the lowest resolution BGO-BGO coincidences. Spatial resolution for images reconstructed from the mixed silicon-BGO coincidences is ~1.5mm FWHM demonstrating the “magnifying-glass” concept.

© 2011 Published by Elsevier Ltd. Selection and/or peer-review under responsibility of [name organizer]

Keywords: PET; silicon detectors; high-resolution imaging; magnifying PET

* Corresponding author. Tel.: +1 734 764-4289; fax: +1 734 764-0288.

E-mail address: nclintho@umich.edu.

1. Introduction

Positron emission tomography or PET is a widely employed imaging method in medicine and biomedical research [1]. Briefly, the subject is injected with a radiolabeled tracer that localizes according to specific metabolic pathways. Upon decay, the radionuclide emits a positron that annihilates with a nearby electron releasing two 511 keV photons traveling in nearly opposite directions. Detection of these photons in time-coincidence localizes the annihilation to a line-of-response (LOR) and from a collection of $10^7 - 10^8$ such events, the 3D distribution of radiotracer can be reconstructed.

Magnifying PET geometries—where a detector having high spatial resolution located close to a region of interest works in coincidence with a conventional PET detector having more modest resolution—have been investigated in a number of studies spanning the past decade. Clinthorne and Park proposed instruments for small animal and patient imaging based on high-resolution detectors used in conjunction with standard PET detectors [2–5]. Tai and co-workers have referred to the concept as “virtual pinhole PET” and have developed several demonstration instruments [6–8]. Huh, et al, have evaluated the concept of an endorectal insert for high resolution prostate imaging and are presently developing a LYSO/silicon photomultiplier based instrument [9]. The goal of the MADEIRA project is to develop a high-resolution add-on probe for clinical PET [10]. More recently, Zhou and co-workers have termed the concept “zoom-in” PET and have investigated the advantage of augmenting conventionally acquired PET data with information from a higher resolution detector [11,12].

To explore potential performance advantages of magnifying geometries for PET applications ranging from small animal imaging to organ-specific high resolution imaging probes for human subjects, we have constructed a demonstration instrument consisting of a partial outer ring of conventional PET detectors supplemented by a partial inner ring of high-resolution silicon detectors. This paper describes the basic principles, construction, and initial images obtained from the device.

2. Principles and Design

2.1. Magnifying PET geometry

The principles of a magnifying geometry are discussed by Park, et al. [5]. We restrict the following discussion to geometries in which a full ring of high resolution detectors (or emulation thereof) surrounds a small field-of-view. This high resolution detector ring is itself inserted into the larger diameter bore of a conventional PET instrument. Since the inner detector may not have high detection efficiency for 511 keV photons, there are three significant classes of PET coincidence events that can be reconstructed: (1) those in which both annihilation photons interact in the high resolution detector ring (referred to as Si-Si here); (2) those in which both photons are detected in the outer, low-resolution ring (BGO-BGO); (3) and

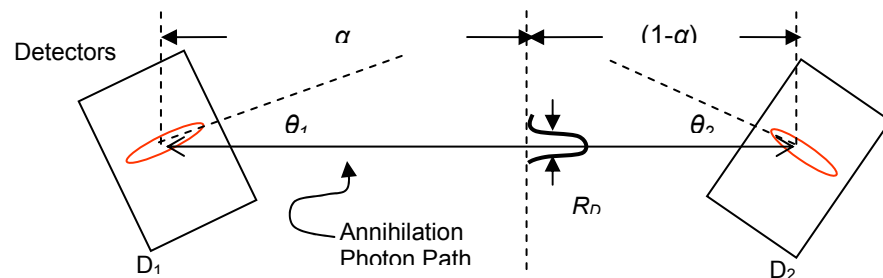


Fig. 1. Diagram illustrating detector geometry and parameters used for approximating intrinsic resolution in Equation (1).

hybrid events (Si-BGO) where one event interacts in the high resolution ring and the other in the low resolution ring. That the Si-Si and BGO-BGO events result in the highest and lowest resolution data, respectively, is clear. The spatial uncertainty of the Si-BGO events, however, varies significantly along the coincidence LOR between the high- and low-resolution detectors as described next.

2.2. Intrinsic spatial resolution in a magnifying geometry

Intrinsic resolution is dominated by the detector (either high- or low-resolution) to which the positron source is physically closest. Thus, resolution in a small FOV surrounded by high-resolution detectors will be dominated by the performance of that detector as shown through the following expression:

$$R_D \approx 2.35 \sqrt{\left((1-\alpha)^2 (\sin^2 \theta_1 \sigma_{D1}^2 + \cos^2 \theta_1 \sigma_{C1}^2) + \alpha^2 (\sin^2 \theta_2 \sigma_{D2}^2 + \cos^2 \theta_2 \sigma_{C2}^2)\right)} \quad (1)$$

where σ_C and σ_D are the standard deviations in estimating position in each detector in the circumferential or transverse and depth directions, respectively, α is the fractional distance of the source along a coincidence LOR intersecting the two detectors at the angles of incidence shown in Fig. 1. Note that the expression conveniently accounts for depth-of-interaction uncertainty that often degrades resolution at large angles of incidence.

As an example, assuming normal incidence on both detectors, the intrinsic resolution for a source 3cm from a detector having 1mm FWHM resolution and 40cm from a detector having 6mm FWHM resolution would be 1.1mm FWHM including the effects of acolinearity of the annihilation radiation in soft-tissue. At 10cm from the higher resolution detector, this decreases to 1.7mm FWHM.

2.3. Tradeoff between reconstructed resolution and noise

Although intrinsic measurement uncertainty plays a significant role in overall system performance, spatial resolution in the reconstructed image can actually be better than that suggested by the intrinsic resolution if the system aperture function is appropriately modeled in the reconstruction process [1]. Such *resolution recovery*, however, increases the noise level or variance in reconstructed images. This increase is highly non-linear as a function of reconstructed resolution as shown in Fig. 2(a) where the

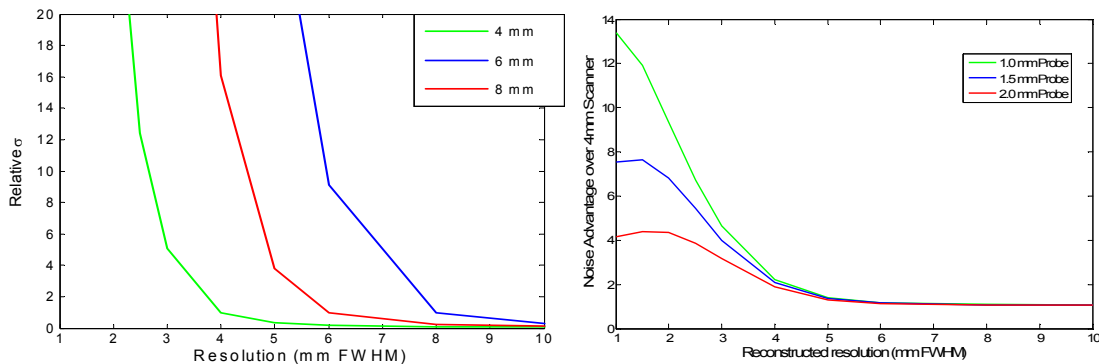


Fig. 2. (a) Standard deviation vs. reconstructed image resolution for detectors supporting intrinsic resolution of 4mm, 6mm, and 8mm FWHM. Standard deviation has been normalized to unity for reconstructed resolution equal to the intrinsic resolution. (b) Noise advantage as a function of reconstructed image resolution for an additional 12% of data having intrinsic resolutions of 1.0mm, 1.5mm, and 2.0mm FWHM added to 4mm FWHM data.

approximate standard deviation at the center of a uniformly emitting disk source occupying the full FOV is plotted against desired spatial resolution in reconstructed images for simulated PET systems having Gaussian resolutions of 4mm, 6mm, and 8mm FWHM (curves were calculated using the modified uniform CR bound [13]). Each curve has been normalized to unity at the intrinsic resolution of the simulated scanner. Note how quickly noise increases as one attempts to operate at points better than the intrinsic resolution. As an example, operating the 4mm system at 3mm FWHM reconstructed resolution increases the standard deviation by a factor of 10. To achieve the same noise level as a reconstruction with 4mm FWHM resolution, 100x the number of events would need to be collected.

Fig. 2(b) demonstrates the effect of adding a small amount (12%) of additional data having resolutions of 1mm, 1.5mm, and 2mm FWHM to PET data from a system having 4mm intrinsic resolution. Curves shown are the standard deviation of reconstructions from the combined datasets divided by that of the 4mm dataset alone and are plotted against desired reconstructed resolution. At operating points above 4mm FWHM, there is little advantage to including information from a high resolution detector while there is a considerable performance improvement at operating points *better* than 4mm FWHM. And as expected, the advantage increases for detectors having higher resolution.

2.4. Silicon as an unconventional PET detector

The previous section demonstrates that adding a modest amount of data having high intrinsic resolution to lower resolution data can have a significant impact on performance. In a conventional PET scanner, detectors typically comprise high-density scintillators such as BGO or LYSO read out by photodetectors. It remains challenging to achieve submillimeter spatial resolution with this approach as well as appropriate depth of interaction resolution (i.e., 3D position resolution). Solid-state detectors based on silicon, however, can readily achieve submillimeter performance in 3D. Even though attenuation length of silicon for 511 keV photons is 5cm as opposed to 1cm for BGO and 1.1cm for LYSO, information in the previous section demonstrates that silicon may well outperform the more conventional scintillation detectors when the goal is resolution in the neighborhood of 1mm FWHM.

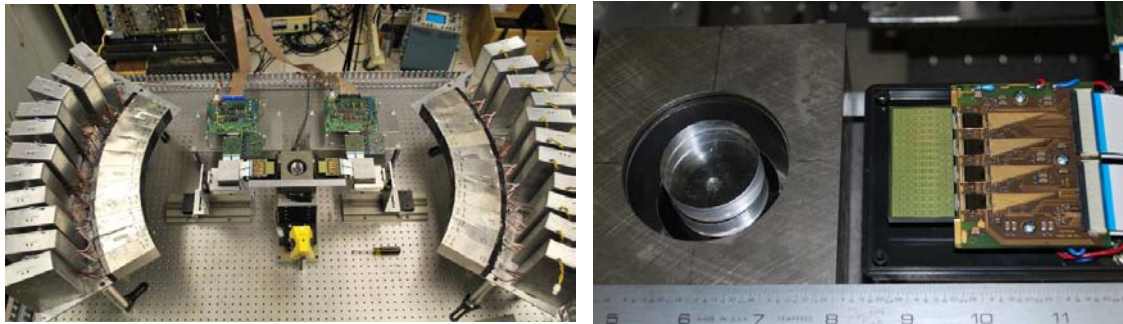


Fig. 3. (a) Dual partial-ring PET demonstrator showing BGO block detectors at 500mm radius and silicon pad detectors at ~70 mm radius surrounding 45mm diameter field-of-view. Full PET dataset is acquired by rotating object. (b) Close-up showing edgewise positioning of 1mm thick silicon pad detector, object turntable and tungsten slice collimator.

3. Demonstrator Design

To evaluate the use of silicon as a PET detector for the primary purpose of rodent imaging within a 50mm FOV, we have assembled the demonstration instrument shown in Fig. 3(a). The instrument consists of a partial ring of 24 BGO detectors at 500mm radius within which a partial “ring” of silicon pad detectors at nominal radius 70mm has been inserted. To reduce the overall event rate on the detectors, the source has been collimated to a 1mm thick slice using tungsten plates and the silicon detectors have been located on edge as shown in Fig. 3(b) to achieve high detection efficiency for the slice. A full set of PET data is acquired by rotating the object in 6° steps and recording Si-Si, Si-BGO, and BGO-BGO coincidences. Raw coincidence information is recorded in a structured list containing position and energy as well as a time-stamp for each trigger, which allows acquired data to be post-processed to change energy thresholds or timing window widths, for example.

3.1. BGO block detectors

The 24 BGO block detectors were scavenged from a CTI 931 (ca. 1985) PET scanner and each comprises a 4x8 BGO crystal array of 6mm x 12mm crystals read out by a 2 x 2 array of 25mm square PMTs. The detectors are oriented such that the 6mm width is along the circumference of the ring. PMT outputs are routed to a simple CR-RC shaping amplifier and then to a peak-sensing ADC. Timing resolution for BGO-BGO coincidences is ~ 12 ns FWHM while typical energy resolution for the 511 keV peak is 20% FWHM. Although the performance of these detectors is inferior to modern LYSO (or LSO) based devices, they provide an excellent demonstration of the magnifying PET concept using Si-BGO coincidences.

3.2. Silicon pad detectors

The silicon detectors currently used in this instrument are 1mm thick and each have 512 1.4mm x 1.4mm pads arranged in a 16 x 32 array [14]. Each detector is read out by four VATAGP-7 ASICs developed for this application by Gamma Medica-Ideas [15] and a VME bus based interface. Since virtually all interactions of 511 keV photons will be Compton scattering, the triggering threshold for PET measurements was set to nominally 30 keV but varied by channel depending on inherent offset. While the ASIC has trim-DACs for each channel to allow triggering at the same energy, these were not calibrated for the measurements presented below. Energy resolution with this setup is approximately 2 keV FWHM (although this does not directly impact PET performance of the instrument). Timing resolution is relatively poor due to both time-walk of the leading-edge trigger in the ASIC, which can be corrected off-line, and variations due to 3D interaction location in the detector and uncertainty in the Compton recoil electron path. Coincidence resolution between two silicon detectors operated at 136 V bias is ~ 50 ns FWHM. Increasing the bias and correcting the pulse-height dependent time-walk improves timing performance but was not done since the random coincidence rate was sufficiently low in the single-slice geometry.

4. Imaging Performance

4.1. Reconstructions from simulated data

To understand what to expect from reconstructions of a resolution phantom and to explore the advantages of simultaneously reconstructing a single image from all three types of coincidence events, a

single-slice Monte Carlo simulation was conducted using measurement sensitivities and intrinsic resolutions consistent with those of the demonstrator. Specifically, 50 million total detected events were used (3% Si-Si, 14% Si-BGO, and 83% BGO-BGO) with Si-Si resolution of 0.7mm FWHM, Si-BGO resolution of 1.2mm FWHM and BGO-BGO resolution of 3.2 mm FWHM (all Gaussian shaped). These figures correspond to an idealized version of the demonstrator and performance of the actual system is expected to be significantly worse due primarily to significant mis-positioning in the BGO detectors and to a lesser extent inaccuracies in modeling the response of the real device.

Reconstructions from the simulated data using a regularized maximum likelihood (ML) reconstruction [16] are shown in Fig. 4 for a resolution phantom consisting of 4.8mm, 4.0mm, 3.2mm, 2.4mm, 1.6mm and 1.2mm diameter rods separated by two rod diameters center-to-center. The top row shows images reconstructed from the individual coincidence events (Si-Si, Si-BGO, and BGO-BGO). Performance is as expected with the Si-Si events demonstrating the best resolution (and spot shape fidelity) but also the highest noise. BGO-BGO resolution is the worst and reconstruction also shows aliasing for the wedges containing the three smallest diameter spots due to undersampling. Reconstructions from the Si-BGO events greatly improve upon this with resolution closer to that of the Si-Si reconstruction. Note, however, that the smaller spots in the Si-BGO and BGO-BGO reconstructions tend to be overly sharp with diameters smaller than actual and that the larger spots in the Si-BGO reconstructions suffer from edge overshoot.

The image at the bottom left in Fig. 4 combines both Si-Si and Si-BGO events. Resolution is improved over the reconstruction from Si-BGO events alone and noise is reduced over using only Si-Si events. Moreover, the spot shape has better fidelity. As predicted in [16], adding the lowest resolution

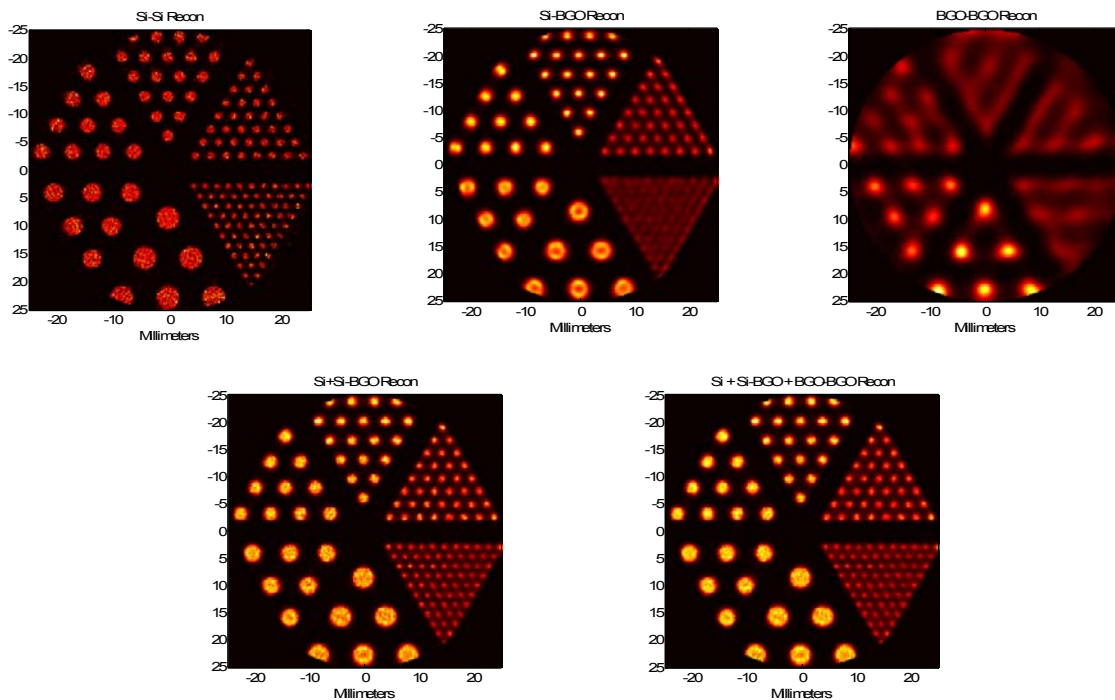


Fig. 4. Top row left-to-right: Si-Si reconstruction from simulated data, Si-BGO reconstruction, BGO-BGO reconstruction. Note noise in Si-Si reconstruction as well as distortion of spot shapes in Si-BGO and BGO-BGO reconstructions. Bottom row: composite reconstructions using Si-Si and Si-BGO data (left) and all events (right).

BGO-BGO events adds little, if anything, to overall performance and slows convergence of the iterative ML reconstruction.

4.2. Reconstructions from demonstrator measurements

Fig. 5 shows images reconstructed from micro-Jaszczak resolution phantom measurements acquired using the demonstrator instrument using ~ 185 MBq of ^{18}F -fluorodeoxyglucose (FDG) over an interval of 5 hours. The order is the same as for the reconstructions shown in Fig. 4. In this case, Si-Si events comprise 3.4%, Si-BGO 20.5%, and BGO-BGO 76.1% of the 1.2×10^7 collected coincidences. For reconstruction, the same system model for reconstructing the simulated data in Fig. 5 was used (responses of 0.7mm, 1.2mm, and 3.2mm FWHM for Si-Si, Si-BGO, and BGO-BGO events, respectively). The hot ring around the resolution phantom is real and not visualized in the Si-Si reconstruction due to the slightly smaller FOV size (45 mm vs. 50mm diameter). Trends in these reconstructions correspond to those in Fig. 4 with the exception that the Si-Si reconstruction is significantly noisier due to fewer coincidence events. Composite reconstructions are shown in the bottom row. While reconstruction from Si-Si and Si-BGO events is perhaps slightly better than either reconstruction alone (the outer ring is correctly reconstructed and the blurring slightly less for the smallest diameter spots), reconstruction from all events reduces performance somewhat. This is due to both a significantly slower convergence rate for the combined data and to inaccuracies in modeling the actual response of the BGO-BGO events. If modeling is consistent, there is no reason that including the lowest resolution events should decrease performance.

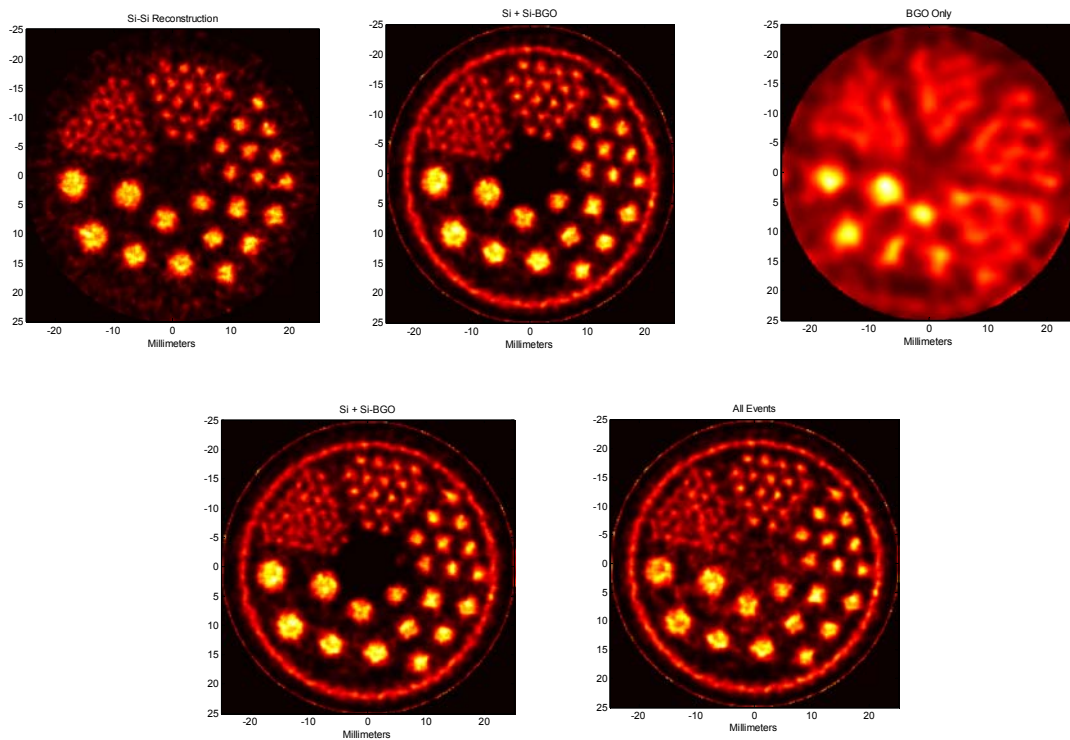


Fig. 5. Reconstructions from data measured with the demonstrator shown in Fig. 3. Top row left-to-right: reconstructions of a micro-Jaszczak resolution phantom from Si-Si, Si-BGO, and BGO-BGO events alone. Bottom row left: reconstruction from Si-Si and Si-BGO events. Bottom right: reconstruction using all events.

Nevertheless, when the desired operating point is at a resolution much higher than the intrinsic resolution of the BGO-BGO events one will lose little performance by disregarding them as shown in Fig. 4.

5. Conclusions

To assist in our ongoing investigation of high resolution PET in magnifying geometries we have constructed a demonstration instrument consisting of low resolution BGO detectors and high resolution silicon pad detectors. Preliminary reconstructions of resolution phantom data acquired using the device were presented and performance qualitatively agreed with Monte Carlo simulations from an idealized system. In the coming months, this instrument will be used to evaluate a number of high-resolution PET imaging configurations including those applicable to small animals as well as probes for prostate and head-and-neck imaging in human subjects.

Acknowledgement

We acknowledge support from the US Department of Health and Human Services under NIH grant R01 EB430-37, the US Army Congressionally Directed Medical Research Program under grant W81XWH-09-1-0413, and the European Commission under Framework Programme 7 EURATOM-FISSION grant 212100 (Acronym: MADEIRA).

References

- [1] Wernick M, Aarsvold J (eds). *Emission tomography: the fundamentals of PET and SPECT*. New York: Elsevier Academic Press; 2004.
- [2] Clinthorne NH, Meier D, Hua C, et al. Very high resolution animal PET (abs). *J Nucl Med Supp* 2000; **41**:20P.
- [3] Park SJ, Rogers WL, Wilderman SJ, et al. Design of a very high resolution animal PET (abs). *J Nucl Med Supp* 2001; **42**:55P.
- [4] Clinthorne NH, Park SJ, Wilderman SJ, et al. High resolution PET detector (abs). *J Nucl Med Supp* 2001; **42**:102P.
- [5] Park SJ, Rogers WL, Clinthorne NH: Design of a very high resolution small animal PET scanner using a silicon scatter detector insert. *Phys Med Biol* 2007; **52**:4653–77.
- [6] Tai YC, Wu H, Pal D, et al. Virtual pinhole PET. *J Nucl Med* 2008; **49**:471–9.
- [7] Wu H, Pal D, Song TY, et al. Micro Insert: A Prototype Full-Ring PET Device for Improving the Image Resolution of a Small-Animal PET Scanner. *J Nucl Med* 2008; **49**:1668–76.
- [8] Wu, H, Pal D, O’Sullivan, et al. A Feasibility Study of a Prototype PET Insert Device to Convert a General-Purpose Animal PET Scanner to Higher Resolution. *J Nucl Med* 2008; **49**:79–87.
- [9] Huh SS, Clinthorne NH, Rogers WL: Investigation of an internal PET probe for prostate imaging. *Nucl Ins Met Phys Res A* 2006; **579**:339–343.
- [10] Studen A, Chesi E, Cindro V, et al. Report on the MADEIRA PET probe. *Nuclear Science Symposium Conference Record, 2010 IEEE*. 2010; p. 1755–8.
- [11] Zhou J, Qi J. Theoretical analysis and simulation study of a high-resolution zoom-in PET system. *Phys Med Biol* 2009; **54**:5193–208.
- [12] Zhou J, Qi J. Adaptive imaging for lesion detection using a zoom-in PET system. *IEEE Trans Med Imag* 2011; **30**:119–130.
- [13] Meng LJ, Clinthorne NH. A modified uniform Cramer-Rao bound for multiple pinhole aperture design. *IEEE Trans Med Imag* 2004; **23**:896–902.
- [14] Meier D, Czermak A, Jalocha P, et al. Silicon detector for a Compton camera in nuclear medical imaging. *IEEE Trans Nucl Sci* 2002; **49**:812–16.
- [15] Linhart V, Burdette D, Chesi E, et al. Spectroscopy study of imaging devices based on silicon pixel array detector coupled to VATAGP7 readout chips. *J Inst* 2011, doi:10.1088/1748-0221/6/01/C01092.
- [16] Clinthorne NH, Park SJ, Rogers WL, et al. Multi-resolution image reconstruction for a high-resolution small animal PET device. *Nuclear Science Symposium Conference Record, 2003 IEEE*. 2003; p. 1997–2001.